MAGNETIC RECONANCE IMAGING CHARACTERIZATION OF POROUS SUBSTRATES AND MODELS OF SOIL AND BIOFILMS

by

GABRIELE MICHELE CIMMARUSTI

A thesis submitted to the
University of Birmingham
For the degree of
DOCTOR OF PHILOSOPHY

School of Chemistry
College of Engineering and Physical Science
University of Birmingham

March 2021

UNIVERSITY OF
BIRMINGHAM

University of Birmingham Research Archive

e-theses repository

This unpublished thesis/dissertation is copyright of the author and/or third parties. The intellectual property rights of the author or third parties in respect of this work are as defined by The Copyright Designs and Patents Act 1988 or as modified by any successor legislation.

Any use made of information contained in this thesis/dissertation must be in accordance with that legislation and must be properly acknowledged. Further distribution or reproduction in any format is prohibited without the permission of the copyright holder.

ABSTRACT

Bacteria and biofilms are frequently found growing in sponges and are a common cause of malodour in the sponge and cross-contamination of humans and surfaces with the risk of causing bacterial infections. Bacterial infection generates high annual healthcare costs and are related to high mortality rates. Removal of bacteria and biofilms from sponges is thus of critical importance to avoid infections, food poisoning, and surface contamination. To tackle biofilm development in sponges, and thus reduce cross contamination, fast-moving consumer goods (FMCGs) companies have focused on developing detergents which can remove food from sponges. However, due to their intrinsic method's limitation, current existing techniques, such as X-Ray micro-CT, confocal laser scanning microscopy, scanning and transmission electron microscopy, do not allow a complete understanding and visualization on how detergents act in removing food and biofilms from sponges. To fulfil this gap, new methodologies need to be developed to increase knowledge on biofilm development, particularly within sponges, and its relationship with food residues, as well as on fluid dynamics within sponges. Thanks to their nature, nuclear magnetic resonance (NMR) and magnetic resonance imaging (MRI) could allow to image food residues and biofilm development in porous media in-situ and in-vivo. Moreover, NRM and MRI enable the characterization of the 3D internal structure of porous media and the visualization of fluid flow within them. Thus, NMR and MRI could potentially allow to study how the physical parameters of sponges affect fluid flow, and how this is related to food residues removal and biofilm development in sponges, in-situ and without the need of pre-treatments.

In this work, novel nuclear magnetic resonance (NMR) and magnetic resonance imaging (MRI) have been developed to characterize polyurethane open-cell porous media, and directly visualize food and biofilms within, without the need of sample pre-treatment or the addition of contrast agents. A combination of NMR relaxometry, MRI T_2 relaxation maps and X-ray micro computed tomography (μCT), has highlighted the dependence of T_2 relaxation times of water, within the foam, on the pore sizes. This has enabled the creation of new protocols to characterize polymeric open-cell porous media directly by MRI, which can be combined with MRI visualization of composition and flow. MRI Chemical Shift Selective (CHESS) imaging has been employed to visualize food residues within polyurethane (PU) sponges, enabling the selective mapping of hydrophobic and hydrophilic residues within the sponge without additional contrast agent. Finally, MRI chemical exchange saturation transfer (CEST) experiments have been successfully developed to image polysaccharide-based (alginate) materials within sponges, demonstrating their potential to visualise the exopolysaccharide matrix of biofilms without the need for additional contrast agents.

With love to my wife, Thais Rocha

Acknowledgments

At first, I would like to thanks my supervisor, Dr. Melanie M. Britton, for her support and teachings throughout my Ph.D. She has always pushed me to give the best of myself and gave me useful hints to improve both scientifically and personally.

I am also thankful to Eric Robles, Anju Brooker, Karl Brookman and all the people at P&G for all the insights and support they have provided over the last four year, and for reading and approving this thesis.

I would also like to thanks all the other Ph.D. students involved in the BioClean project. In these years, we have formed a family, and we have supported each other, sharing bad and good moments that will be bound in my memory forever.

Special thanks go to all the people involved in the BioClean project, which have also been supportive and have given me, during the years, invaluable suggestions and help. In Particular, I would like to thanks Matthieu Boone, Veerla Cnudde and Abhishek Shastry for their help with μCT measurements and data interpretation.

All the members of the Britton group also deserve my acknowledgements. In particular, Emma, for teaching me the fundamental of Prospa and for always been there when I needed clarification on NMR theory and experimental procedures. Claire, Yasmeen and Helen for all the discussion on NMR we had, for all your help with measurements, but in particular for sharing with me all the frustrations and for making my time in the office much funnier and amusing.

I thank my family and all my friends for their unconditional support. Particularly, my Mom and Dad for all the sacrifices they have done to allow me to study and reach my dream. Without them, this goal would have been impossible to achieve.

Finally, my biggest thanks go to my wife Thais. You made my life a thousand times better, and I will never be able to thank you enough for all the joy and love you brought to my life. You have supported me through all the bad moments of my Ph.D. and pushed me to keep going and never give up. Part of this Ph.D. is also yours.

Gabriele

Table of Content

1 INTRODUCTION 1

1.1 Prologue 1

1.2 Biofilms 3

1.2.1 Extracellular polymeric substances 5

1.2.2 Role of the EPS matrix 6

1.2.3 Effect of substrates on biofilm growth 8

1.2.4 Biofilm morphology in porous media 10

1.2.5 Use of biofilms in biotechnological applications 12

1.2.6 Human infections caused by biofilms 14

1.2.7 Problems related to biofilms in industry 15

1.2.8 Problems related to biofilms in domestic environments 16

1.2.7 Biofilm removal in kitchen sponges 18

1.3 Imaging biofilm in porous media 19

1.3.1 Scanning electron microscopy 19

1.3.2 Confocal laser scanning microscopy 20

1.3.3 X-ray computed tomography 22

1.3.4 MRI visualization of Biofilms 23

1.4 Thesis outline 26

1.5 References 29

2 METHODS AND THEORY 40

2.1 NMR principles 40

2.1.1 Chemical shift 42
2.1.2 NMR relaxation 43
2.2 Magnetic resonance imaging 48
2.2.1 MRI Contrast 50
2.2.2 Chemical exchange saturation transfer imaging 52
2.3 Complementary techniques 57
2.3.1 X-ray micro-computed tomography 57
2.3.2 Confocal laser scanning microscopy 59
2.4 Porous media characterization 60
2.4.1 Pore structure parameters 61
2.4.2 NMR relaxation time for measuring the pore size distribution 64
2.4.3 MRI for porous media characterization 66
2.4.4 Micro-CT for porous media characterization 68
2.5 Flexible polyurethane foams 70
2.6 References 74
3 POLYURETHANE OPEN-CELL SPONGES CHARACTERIZATION 79
3.1. Introduction 79
3.2. Materials and Methods 83
3.2.1. Sample preparation 83
3.2.2. X-ray micro-computed tomography 84
3.2.3. Magnetic resonance 85
3.2.4. MR T_2 relaxation time maps correction 86
3.2.5. Statistical analysis 87

3.3. Results 88

3.4. Discussion 97

3.5. Conclusion 99

3.6. References 101

4 VISUALIZATION OF BIOFILMS AND BIOFILM NUTRIENTS IN POLYURETHANE SPONGES 104

4.1 Introduction 104

4.2 Materials and methods 107

4.2.1 Biofilm growth in sponge 107

4.2.1.1 Sample preparation 107

4.2.1.2 Bacteria and Biofilm growth 108

4.2.1.3 Biofilm staining and confocal microscopy 109

4.2.2 Chemical shift selective imaging 110

4.2.2.1 Sample preparation 110

4.2.2.2 NMR spectroscopy and CHESS experiments 111

4.3 Results 113

4.3.1 Confocal microscopy of biofilm in sponge 113

4.3.2 Confocal microscopy on sponge 115

4.3.3 NMR spectroscopy and MR CHESS imaging on water and oil 118

4.3.4 NMR spectroscopy and MR CHESS imaging on sponge plugs filled with water and oil. 119

4.4 Discussion 122

4.4.1 CLSM on sponge and biofilm in sponge 122

4.4.2 CHESS imaging of biofilm nutrients 123

4.5 Conclusion 124

4.6 References 126

5 BIOFILM MIMIC MATERIAL 127

5.1 Introduction 127

5.2 Materials and methods 130

5.2.1 Sample preparation 130

5.2.1.1 Solutions preparation 130

5.2.1.2 Sodium alginate beads 130

5.2.1.3 $CaCl_2$ and Sodium alginate gel in sponge 130

5.2.2 MRI CEST and T_2 map experiments 131

5.2.3 CEST Data analysis 132

5.3 Results 134

5.3.1 Alginate solution 134

5.3.2 Alginate gel beads 138

5.3.2 $CaCl_2$ solution in sponge 141

5.3.3 Alginate Gel in sponge 141

5.4 Discussion 144

5.5 Conclusions 146

5.6 References 148

6 CONCLUSION AND FUTURE WORK 150

6.1 References 157

APPENDICES *158*

Appendix 1: MATLAB code for MR CEST data analysis **158**

Appendix 2: "Characterization of open-cell sponges via magnetic resonance and X-ray tomography". **161**

List of Figures

Figure 1.1 . Diagram of biofilms life cycle: 1. Single bacteria cells land on the surface. 2 Bacteria clonal propagate and attach to the surface. 3. Polysaccharides secretion. 4. 3D biofilm growth. 5. Biofilm maturation and bacteria cell detachment..... 4

Figure 2.1Schematic diagram showing precession of the nuclear magnetic moment, μ, in a static magnetic field $\boldsymbol{B}_0$..... 40

Figure 2.2 Schematic diagram showing the energy levels and the orientation of the spins of an I = $1/2$ nucleus when placed in an external magnetic field $\boldsymbol{B}_0$..... 41

Figure 2.3 Schematic graph showing the T_1 and T_2 relaxation time with the correlation time τ_c..... 44

Figure 2.4 Schematic diagram of an inversion recovery pulse sequence..... 45

Figure 2.5 Schematic diagram of a spin-echo pulse sequence..... 47

Figure 2.6 Schematic diagram of the CPMG sequence..... 48

Figure 2.7 Schematic diagram of a CHESS imaging sequence..... 52

Figure 2.8 Diagram describing the CEST effect. A solute is saturated by an RF pulse, which reduces its signal. The saturated hydrogen is then exchanged with an unsaturated proton of the water, causing a reduction of the water signal. This process continues during the experiment time leading to an amplified decrease in water signal..... 53

Figure 2.9 example plot of a z-spectrum and MTR_{asym} 55

Figure 2.10 Confocal diagram configuration. 60

Figure 2.11 Schematic diagram showing two different pores and the spheres (dark grey) used to evaluate the maximum opening (blue arrow). 69

Figure 2.12. A schematic representation of a) a closed-cell foam, and b) an open-cell foam 71

Figure 2.13 Gel reaction..... 71

Figure 2.14 Blow reaction: a) first stage; b) decomposition step; c) urea formation . 72

Figure 3.1 a) Photograph of polyurethane sponge. b) Schematic diagram for the set-up used to hold and compress sponge plugs..... 84

Figure 3.2 Plot of the ratio between the CPMG T_2 relaxation time and T_2 evaluated from T_2 maps R vs T_2 obtained from RARE sequence. The black line represents a linear fit of the data. CPMG data were recorded collecting 64 spectra, varying the number of echoes from 0 to 2048, logarithmically spaced, with an echo time of 2 ms and repetition time of 15 s and a spectral width of 100,000 Hz. T_2 relaxation time maps were acquired with a RARE factor of 128, echo time of 8 ms and repetition time of 15 s. a 64 × 128-pixels matrix, with a field of view of 25 × 50 mm. 87

Figure 3.3 3D μCT renderings of an a) uncompressed and b) 60 % compressed plug. 3D renderings of a vertical clipping plane, with the maximum opening distribution for c) uncompressed and d) 60 % compressed plug. All images are for the same plug (plug B_2). 89

Figure 3.4 . Extracted sections from 2D ^{1}H MR T_2 relaxation maps of 7° dH water in an uncompressed (a) and 60% compressed (b) sponge plug. Both images are for the same plug (plug B_2). 91

Figure 3.5 Plots of the distribution of maximum opening determined from μCT for compressed (- -) and uncompressed (—) plugs extracted from sponge A (a-c), sponge B (d-f), and sponge C (g-i). 92

Figure 3.6 Plots of the distribution of T_2 relaxation time determined from T_2 relaxation MR maps for compressed (- -) and uncompressed (—) plugs extracted from sponge A (a-c), sponge B (d-f), and sponge C (g-i). 93

Figure 3.7 Plots of the distribution of T_2 relaxation time determined from bulk T_2 relaxation time measurements for compressed (- -) and uncompressed (—) plugs extracted from sponge A (a-c), sponge B (d-f), and sponge C (g-i). 94

Figure 3.8 Plot of the average maximum opening vs bulk T_2 MR relaxation time (a) and average T_2 relaxation time determined from T_2 relaxation MR maps (b) for 7° dH water in uncompressed and compressed sponge plugs. The dotted lines are a linear fit of the data. Two outlying samples are circled in each plot. 96

Figure 3.9 3D μCT reconstructed image of one of the two 60 % compressed plug related to the outliers points in figure 7. An indentation, caused by a bending of the plug when compressed, is highlighted by a white circle. 97

Figure 4.1 Schematic diagram of a) a six well-plate, observed from the top, showing the growth liquid (yellow) and the sponge cube (blue) within each well and b) a side view of a single well. 108

Figure 4.2 Schematic diagram of the sample holder and the positioning of the NMR tubes for the CHESS experiments on water (light blue) and sunflower oil (yellow). 111

Figure 4.3 Diagram representing a sponge plug used for CHESS images of oil and water in sponge, with the position of the four 1 mm 2D axial slices (red rectangles) recorded. 112

Figure 4.4 CLSM images of sponges after 72h of bacteria growth stained with acridine orange using a bath staining method with different dye concentration a) 0.002 % w/v, b)0.001 % w/v, c) 0.0005 % w/v, and using a syringe staining method with two different dye concentrations d) 0.002 % w/v, and e) 0.001 % w/v. Acridine orange was excited by a 405 nm laser and emission was detected in the range of 488 - 550 nm. Calcofluor white was excited by a 405 nm laser and emission was detected in the range 430 – 550 nm..... 113

Figure 4.5 CLSM images of sponges after 72h of bacteria growth stained with Calcofluor white using a bath staining method with different dye concentration a) 0.1 % w/v, b)0.05 % w/v, c) 0.025 % w/v, and using a syringe staining method with three different dye concentrations d) 0.1 % w/v, and e) 0.05 % w/v and 0.025 %w/v. Calcofluor white was excited by a 405 nm laser and emission was detected in the range 430 – 550 nm. 115

Figure 4.6 CLSM images of a clean sponge in absence of biofilms. The sponge was excited with four different wavelengths using four different lasers. For image acquisition, fluorescence emissions were acquired at various wavelength ranges. 117

Figure 4.7 NMR spectra of sunflower oil (red) and of a mixture of water and sunflower oil (blue)in five mm NMR tubes. 118

Figure 4.8 a) 2D axial T_2 weighted image of the phantom containing three 5 mm NRM tubes filled with water, oil, and a mixture of water-oil, and CHESS images acquired by selectively exciting b) the aliphatic protons of oil, and c) water protons. 119

Figure 4.9 ^1H NMR spectra of water (red) and of a mixture of water and sunflower oil (blue) within sponge plugs..... 120

Figure 4.10 T_2 weighted image of the phantom containing three different sponge specimens soaked with water, oil, and a mixture of water and oil..... 121

Figure 4.11 MR oil CHESS images (a-d), MR water CHESS images (e-h), and distribution maps of oil and water (i-n) within four slices of the phantom containing three different sponge specimens soaked with water, oil, and a mixture of water and oil. For the distribution map, the oil domains are represented in blue, the water domains in green, and the domains where both substances are present are represented in red. 121

Figure 5.1 Flow chart showing the steps performed to correct the $\boldsymbol{B}_0$ inhomogeneities within CEST images and to evaluate the Z-spectrum and MTR_{asym}..... 133

Figure 5.2 2D axial ^1H MR T_2 relaxation map of water for 2 % w/w sodium alginate solution in a 5 mm NMR tube. 134

Figure 5.3 A selection of 2D axial MRI CEST images, displayed at an interval of 15 Hz, acquired for 2 % w/w sodium alginate solution in a 5 mm NMR tube. The images displayed cover the range of frequency offset between 1680 Hz and 1335 Hz. 135

Figure 5.4 a) Z-spectrum and b) corrected spline-fitted z-spectrum, evaluated from each pixel of the 41 CEST images of the 2 % w/w alginate solution in a 5 mm NMR tube. 136

Figure 5.5 Plot of the Average z-spectrum and MTR_{asym} for 2 % w/w sodium alginate solution as a function of frequency offset. 137

Figure 5.6 2D axial ^1H MR T_2 relaxation map of 2 % w/w alginate gel beads in 0.2 M $CaCl_2$ solution within a 5 mm NMR tube. 138

Figure 5.7 Averaged z-spectrum for a) alginate gel bead, and b) 0.2 M $CaCl_2$ solution surrounding the bead, within a 5 mm NMR tube. 139

Figure 5.8 a) Axial MR spin density image and b) CEST map of the alginate gel bead in 0.2 M CaCl2 within a 5 mm NMR tube. 140

Figure 5.9 Averaged z-spectrum for water in a 0.2 M $CaCl_2$ solution within a sponge plug..... 141

Figure 5.10 2D axial ^1H MR T_2 relaxation map of sponge filled with 0.2 M $CaCl_2$ solution, following injection of sodium alginate. Alginate gel is formed with a T_2 = 110 ms ± 12 ms and appears blue. The surrounding liquid has a T_2 = 256 ms ± 24 ms and appears green. This solution is predominately 0.2 M $CaCl_2$ but also contains residual sodium alginate. The black pixels in the sponge are regions with low signal intensity. 142

Figure 5.11 Averaged z-spectrum evaluated from CEST images of alginate gel in a sponge saturated with CaCl2 solution for a) alginate gel calculated from pixels range [46:50,28:29], and b) 0.2 M CaCl2 solution within a 4 mm diameter sponge plug, calculated from pixels range [31:37,29:38]..... 143

List of Tables

Table 3.1: Total number of pores for uncompressed and compressed plugs from X-ray μCT..... 90

Table 3.2 Average maximum opening from μCT, average MR T_2 relaxation time from T_2 relaxation MR map and bulk T_2 relaxation time determined from a mono- or bi--exponential fit to the CPMG data. The variability in average maximum opening and T_2 relaxation time from MR maps, comes from the standard deviation of values across the sample. 95

Table 4.1 List of the excitation and emission wavelengths used for the CLSM image acquisition of pure polyurethane sponge cubes without biofilm. 110

List of abbreviations

τ_c	Rotational Correlation Time
2D, 3D	2 Dimensional, 3 Dimensional
BAC	Biological Active Carbon
C&D	Cleaning and Disinfection
CEST	Chemical Exchange Saturation Transfer
CF	Cystic Fibrosis
CHESS	Chemical Shift Selective Imaging
CLSM	Confocal Laser Scanning Microscopy
CPMG	Carr-Purcell-Miiboom-Gill
CRS	Chronic Rhinosinusitis
DS	Direct Saturation
ESEM	Environmental Scanning Electron Microscopy
FID	Free Induction Decay
FISH	Fluorescent In-Situ Hybridization
FMCG	Fast-Moving Consumer Goods
FPU	Flexible Polyurethane Foam
K-space	Reciprocal Space Vector
MIP	Mercury Intrusion Porosimetry
MMRB	Moving Bad Biofilm Reactor
MR	Magnetic Resonance
MRI	Magnetic Resonance Imaging
MT	Magnetization Transfer
MTR_{asym}	Magnetic Transfer Asymmetric Ratio
NMR	Nuclear Magnetic Resonance
NNLS 1D	1D Non-Negative Least Square Algorithm
OM	Otitis Media
P. aeruginosa	Pseudomonas Aeruginosa
P. fluorescence	Pseudomonas Fluorescence
P. syringae	Pseudomonas Syringae
PBS	Phosphate Buffer Saline
PU	Polyurethane
RARE	Rapid Acquisition with Relaxation Enhancement
RF	Radio-Frequency
SEM	Scanning Electron Microscopy
T_1	Spin-Lattice Relaxation Time
T_2	Spin-Spin Relaxation Time
TEM	Transmission Electron Microscopy
t_p	Radio-Frequency Pulse Duration
TSB	Trypticase Soy Broth
µCT	X-ray Micro-Computed Tomography
γ	Gyromagnetic Ratio

1 INTRODUCTION

1.1 Prologue

Biofilms are composed of complex communities of bacteria[1] generally composed of multiple species.[2] Biofilms are ubiquitous and adaptable, forming anywhere, and can cause problems in different areas, such as, water treatment, fabrics and laundry, food and human health. Bacteria cause, every year, significant economic and health issues due to food spoilage or bacterial infections caused by cross-contamination from contaminated clothes, kitchen utensil and medical tools. For instance, the treatment for infections caused by catheter contaminations itself generates an annual cost between $296 million to 2.3 billion, with 12-25% of mortality rate.[3] Removal and prevention of biofilms formation is thus extremally important. For biofilm removal, two main processes are performed: cleaning and disinfection. Cleaning has two main objectives: (i) remove and prevents the formation of residues accumulation that can enhance bacteria and biofilm proliferation; (ii) to dissolve or break biofilms extracellular matrix, making microorganisms more accessible to disinfectants.[4] This operation is generally carried out using detergents, whose composition vary depending on type of dirt. For instance, in food industry, alkali compounds are mostly used, which break down proteins using the action of the hydroxyl group. Moreover, when combined with chelates, such as EDTA, alkali compounds have proven to be more effecting in removing biofilm that other chemicals, such as acid detergents.[5] However, conventional cleaning methods by detergent not always are successful in removing dirt and bacteria. In this case, more aggressive treatments are required, which comprise brushing, scraping, or/and the use of enzymes and heat.[6,7] Disinfection is performed

to totally eliminate microorganisms, or to reduce they quantity to a safe level.[8] To reach this goal, various disinfectants have been used, such as iodine compounds, peroxides ,bisphenols, chlorin components and quaternary ammonium compound.[9,10,11] The efficiency of these disinfectants varies depending on the bacteria species. For instance, iodine and quaternary ammonium compounds were found to be less effective than sodium hypochlorite in removing *Listeria* spp. and *Salmonella* spp.[12]

The main problem with using antimicrobials is the increase of bacteria antimicrobial resistance (AMR). AMR is a process that occurs naturally due to bacteria mutation. The constant use of antimicrobials increases the frequency to which this mutation occurs,[13] leading to the creation of so called “super-bacteria”, which present higher resistance to antimicrobials. To overcome this problem, new products for fighting bacteria and biofilms need to be developed without using antimicrobial agents, which are also environmentally friendly and cheap to produce. For the development of these new products, new methodologies need to be developed to study biofilm formation in different environments and their responses to different treatments. To understand biofilm behaviour, in different environments, and how they are affected by various treatments, it becomes extremely important to image biofilms formation and evolution in real time, and in the original biofilm cultivation. In particular, it is interesting to visualize how the presence of food residues in porous media, such as fabrics and sponges, affects biofilm developments. A better understanding of this interaction can help the creation of more efficient products, that tackle biofilm contamination problems indirectly, by decreasing their food viability and avoiding biofilm formation. Different techniques have been used previously to image and study biofilm development,

including confocal laser scanning microscopy (CLSM)[14], X-ray micro-computed tomography (μCT), scanning electron microscopy (SEM), transmission electron microscopy (TEM), ultrasound. These techniques provide good images of biofilms with high image resolution. However, they all require pre-treatments of the sample that can affect the bacteria structure. Magnetic resonance imaging (MRI) instead, offers the opportunity to image biofilm without the need of pre-treatment and in their native growing environment, giving the possibility to fully understand biofilm development and interaction with food in porous media.

1.2 Biofilms

Bacteria can be considered the most successful life form on Earth, in terms of the variety of colonized habitats and total biomass. They represent ≈ 15% of the Earth's biomass and can be found in a cornucopia of environments.[15,16] Almost 90 % of bacteria live in micro-communities and form what is known as a biofilm,[17] defined as complex systems that can be composed of multiple species and contain high density of cells (from 10^8 to 10^{11} cells g^{-1}).[18] Bacteria form biofilm through a complex process composed of five steps (figure 1.1).[19] In the first step, bacteria cells land and adhere onto a surface. This is followed by a clonal propagation and attachment, which leads bacteria to colonize a larger surface. Meanwhile, three-dimensional (3D) growth of the community also occurs, due to secretion of polysaccharides, which generate a matrix surrounding bacteria. At the end, after biofilm establishment, some cells escape from the biofilm and colonize new surfaces.

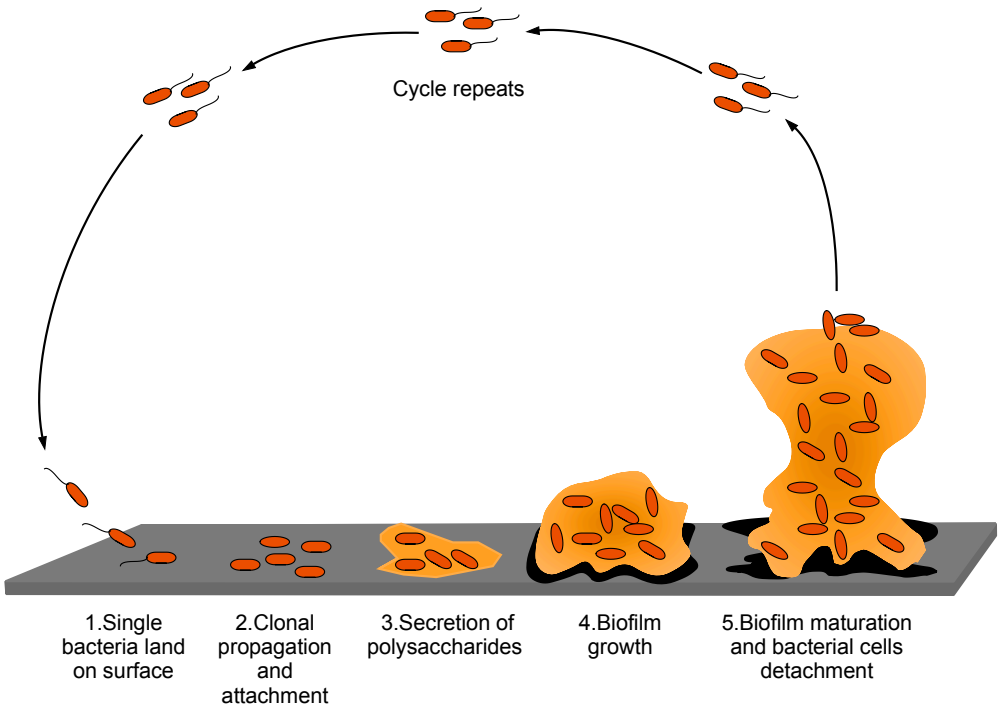


Figure 1.1 . Diagram of biofilms life cycle: 1. Single bacteria cells land on the surface. 2 Bacteria clonal propagate and attach to the surface. 3. Polysaccharides secretion. 4. 3D biofilm growth. 5. Biofilm maturation and bacteria cell detachment.

Compared to free-living bacterial cells, biofilms present a series of new properties that are not available to single cells,[20] which allow bacteria to be more resistant to environmental assault.[2] These include increased resistance to antibiotics, dryness, UV radiation, and variation in pH.[21-24] Most of the advantages of biofilm, over planktonic bacteria, derive from the matrix that surrounds the bacteria and acts as a barrier against external agents.[25] This extracellular matrix is composed of water (up to 97 %) and other components that are generally referred to as extracellular polymeric substances (EPS), like polymers, eDNA, proteins, pili, flagellae and frimbiane.[1,25,26] Each of these components plays an important role in the life of a biofilm and is fundamental for the survival and development of the microbial community.

1.2.1 Extracellular polymeric substances

The EPS can be described as the construction material of the biofilm matrix. Originally, the term referred to *extra-polysaccharides* only, as they were assumed to be the major component of the matrix, excluding water.[27] However, depending on the bacteria species and the environment in which biofilm develops, different macromolecules can be present in the EPS at a higher percentage than polysaccharides.[27] Currently, reference to the EPS refers to all biofilm components present in the matrix apart from bacteria, including polysaccharides, proteins, peptides, lipids and nucleic acid.[28,29] The chemical composition of polysaccharides within a biofilm, and the rate of formation, is strongly dependent on both bacteria genetic and physiochemical environment growth conditions.[1,30-32] Thus, a great diversity of polysaccharides in the EPS composition can be observed for different species of bacteria and also for different strains of the same species of bacteria.[33 34] A good example of the variety of polysaccharides chemical composition, depending on genetic and environment, are the Pseudomonas species. *P. aeruginosa* mainly produce three polysaccharides: (i) *Psl*, composed of D-glucose, D-mannose and L-rhamnose; (ii) *Pel*, a cellulose-like polymer rich in glucose, and (iii) alginate.[32,35] *P. syringae* instead produce, in addition to alginate, *Pel* and *Psl*, a polysaccharide called levan.[32] Variation in the composition of polysaccharides can also be seen within biofilms produced by different strains of the same bacterium. Indeed, *P. aeruginosa* forms alginate as the primary polysaccharide in mucoid strains,[32 36] while little, or no, alginate is found in non-mucoid strains.[37]

1.2.2 Role of the EPS matrix

While biofilm is generally described as a “city of microbes”, the matrix can be defined as the “house of the biofilm cells”.[38] Indeed, it acts as an interface between the external environment and the cells. Moreover, it regulates bacteria physiological activity within the biofilm and provides structural organization.[18] One of the most important property imparted to a biofilm, by the EPS matrix, is an increase in resistance and tolerance towards antimicrobial agents, compared to planktonic bacteria.[23,39] This resistance is produced by a diffusion-reaction inhibition process,[40] which includes diffusion through the EPS, antimicrobials enzymatic degradation, chelation and sacrificial reactions.[40,41] Even if the EPS works as a diffusion barrier for external antimicrobial agents, some of these agents, like tetracycline and daptomycin, are able to penetrate the EPS within a few minutes.[40] When this happens, biofilms can still defend themselves by complexing the antimicrobial or by degrading it using enzymes.[18] The diffusion-reaction inhibition process works particularly well with toxic metals, such as copper.[41] Examples can be seen in biofilms formed by *Erwinia amylovora*, which use the EPS to complex copper in order to decrease its antibacterial action.[41] The combined action of degradation, chelation and EPS, brings the antimicrobial concentration to a sublethal value allowing the survival of bacteria cells.

The binding property of the EPS matrix and the diffusion of chemicals through the EPS also offers the possibility to absorb a wide variety of substances, ranging from metal ions to nutrients.[18,42,43] Metal ions can be used for biofilm stabilization, which confers to the biofilm a higher resistance towards shear forces,[44] which can cause problems when removing biofilms with normal cleaning procedures, such as brushing, flow, or

air pressure. For instance, *Bacillus subtilis* biofilm show an increase of erosion stability toward shear forces when in presence of high metal ions concentration such as Cu^{2+} and Fe^{2+}. [44] In particular, when fed with Cu^{2+} or Fe^{2+}, the biofilm displays a variation of its viscoelastic properties, which confers the biofilm a higher resistance toward shear forces caused by flowing fluids.[44] Similar results have been found for *Pseudomonas fluoresces* biofilm[45] and oral biofilms,[46] where the yield strength has been found to increase with calcium concentration increase.[45,46] For *P. fluoresces* biofilm, this could be related to the uronic acid present in the alginate composing the biofilm, which contains potential crosslinking sites for calcium.

Nutrient sorption is a fundamental step for the bacteria community survival. The different mechanisms for sorption and the wide range of substances that can be trapped within the biofilm, allow the survivor of the biofilm also in difficult environments, such as oligotrophic environments.[47] Besides nutrient sorption, biofilms can also use their own cells and debris from lysed cells to provide nutrients for the community.[48,49] For example, in starving conditions, *Bacillus subtilis* biofilms produce *skf* and *spd* toxins to lyse cells within the community,[50] which are then used as food for biofilm development. Similar behaviour has been observed in *P. auruginosa* and *shewenella* biofilms, which produce DNase enzymes. These enzymes are then used to dissolve the DNA of lysed cells and exploit it as an energy resource.[51,52] Within the matrix it is also possible to find channels and pores that facilitates the transport of liquids and nutrients, and this can be seen as the biofilm circulation system.[53,54]

Another important property imparted by the EPS matrix to the biofilm is the protection against desiccation. Such protection against desiccation arises from the combined action of hydrated polymers produced by the biofilm,[55] like alginate in *P. aeruginosa* mucoid strains, and skin formation in the outer biofilm layer.[56] The former forms a hydrogel retaining water within the biofilm, while the latter prevents water evaporation. Studies on *Escherichia coli*, *Erwinia stewartia* and *Acinetobacter calcoaceticus* have showed how mucoid strains of these bacteria, which are able to produce hydrogels and skin layers, were more resistant to desiccation compared to non-mucoid mutant strains.[55]

1.2.3 Effect of substrates on biofilm growth

The possibility of biofilms to growth in different environment and on different surfaces is strongly related to ability of bacteria to adhere to a surface.[57] Thus, biofilm formation is dependent on the chemical and physical properties of the substrate, such as wettability, roughness, surface charge density and surface topography.[58]

Surface charge density is one of the most important properties affecting bacterial adhesion. Various studies have shown how positively charged surfaces increases the possibility of biofilm adhesion compared to negatively charged surfaces.[59-61] This is related to the fact that bacteria usually possess carboxyl, phosphate and amino groups, which give bacteria a net negative charge, favouring attachment on positively charged surfaces. For instance, Gottenbons *et al*., have shown an increase of 2 times in the attachment and growth of *Pseudomonas aeruginosa* on positively charged surfaces compared to negatively charged ones.[62] However, few studies have also

demonstrated the ability of negatively charged bacteria to strongly adhere to negative charged surfaces thanks to their fimbriae.[63] Therefore, the effect of surface charge density on biofilm development is still not totally understood, and further studies are needed to improve the knowledge.

Surface wettability is the main properties controlling the interaction between liquid and solid phases in biological system, and it is governed by roughness and surface energy.[64] To explain bacterial adhesion and its dependency with surface energy, different models have been used, such as DLVO[65] and thermodynamics-based approaches.[66] The use of DLVO theory have shown that lower ionic strength prevent bacterial adhesion,[67] while higher ionic strengths favour it.[68] Thermodynamic approaches describe the process in a more observational way, such as hydrophobic materials favour attachment of bacteria with hydrophobic surface, while hydrophilic materials favour hydrophilic cells surfaces.[69]

Regarding roughness, an increase of the roughness is usually correlated to a higher biofilm development, due to the increase of surface area available for bacteria attachment. Moreover, rough surfaces better protect bacteria against shear forces, favouring biofilms growth.[70] However, in some cases, an increase in surface roughness has resulted in a decrease of bacteria attachment and subsequent biofilm development. For instance, *S. aureus* and *P. aerouginousa* adhesion was found to be higher in polished stainless steel samples compared to unpolished one.[71] These contrasting results shows how various variable needs to be kept in consideration when studying the dependence of biofilm developments to surface energy and roughness,

such as the type of surface and its topography, the bacteria specie and the medium used for the study.

Surface topography also affects bacteria attachment and biofilm development. In general, surfaces with features whose dimensions are higher on in the same order of bacteria, enhance their attachments. Vice – versa, surfaces with smaller features compared to bacteria tend to reduce the attachment. This last tactic is strongly used in nature, where various animals, like geckos or cicadas, show micro/nanostructure skin, which shows superhydrophobic properties that reduces bacteria adhesion.

1.2.4 Biofilm morphology in porous media

Morphological characteristic of biofilms within porous media can be different from the classical films observed on surfaces or other systems.[72] as describe on section 1.2, biofilm formation is a multi-step process that involves surface adsorption, microbe proliferation, EPS secretion and bacteria detachment.[19] This dynamic process depends on materials' surface properties,[58] food availability, and shear forces.[73] In porous media, the growth process is further complicated by pore network complexity, and pore sizes and shapes, especially when the porous medias is in aqueous environments.[73] For instance, the thickness and of biofilms in porous media was found to be dependent on the pore size,[74] while the intricate pore network, and the change in flow condition during biofilms growth, can favour the development of one specie over another.[74]

Various studies, involving different techniques, have been performed to visualize biofilm morphology in porous media, and its developing. These studies have shown

manly two different biofilm morphologies: (i) biofilm patches; (ii) biofilm streamer or web-like structures.

Biofilm patches mostly form in low shear stress conditions. Studies of biofilm patches development in Nafion grains, have shown that patches possess a high aspect ratio and a tendency to be aligned with the direction of the flow. Moreover, larges patches have been found in smaller pores, suggesting a dependence between patches and pore sizes.[74]

Conversely, biofilm streamers have been observed in porous media when high shear conditions were applied. Indeed, in these conditions, biofilm tend to assume filamentous structures, whose thickness is around 50 μm, were one or both ends of the filament are attached to the surface, while the rest of the filament is floating in the fluid.[19] Streamers, also present lower porosity, higher homogeneity, and stronger adhesion to the surfaces.[75] Web-like structure composed of different streamers have also been observed.[19,72]

While the separation between structures in porous depending on flow can look easy, the situation is much more complex. Indeed, within porous media, different flow condition can occur depending on how pores are distributed and on how permeable the system is. Moreover, biofilms development itself, can affect convective flow through pores, causing a variation of the conditions and thus the subsequential formation of patches or streamers.[72] Thus, complex biofilms, composed of both patches and streamers, can be found in porous media. Paulsen *at all*., [72] observed a three distinct

phases for biofilm formation in porous media, which they considered valid in both high and low flow rate:

1. Between day 1-5, homogenous biofilm formation with no difference between low and high flow rate pores. A high flagellar motion at the bulk-biofilm interface was also observed.
2. Day 5-10, rougher biofilms appearance, composed of large and small cell clusters. Once again, no difference was observed between high and low flow rate pores
3. > 10 days, biofilm streamers formation, with web-like appearance. These streamers seem to develop in denser and faster high flow zones.

While multiple studies have been performed, a clear understanding on the relation between biofilm morphology and pore structure is still lacking. Thus, further studies need to performed, and new methodologies need to be developed, to fully characterized and understand the different morphologies and the reason for their formation.

1.2.5 Use of biofilms in biotechnological applications

Biofilms can be considered either dangerous or useful. This is dependent on many different parameters. Biofilms are used in many biotechnological applications, such as water filtration,[76] solid waste and wastewater biodegradation[77] and biocatalysts.[78] In water filtration, biofilms are used in combination with porous media, overcoming some of the issues of conventional water treatment methods.[76] Indeed, water filtration conventional methods, such as sedimentation or disinfection, are based on

flocculation, disinfection through the use of chlorine and sand filtration.[79,80] However, these conventional methods have difficulties in removing organic matter and can produce disinfection by-products such as haloacetic acids or trihalomethanes.[81 82] Systems with biofilm and porous media instead uses the latter to remove microorganisms and the biofilm within to biodegrade remaining contaminants.[76,82] An example of these systems are biological active carbon (BAC) media filtration that, thanks to the combined action of porous media and the biofilm, enables fewer demand of chemicals, such as chlorine, less bacterial-regrowth in water after the filtration, and reduced risk of producing chlorination by-products.[76] Porous media are also used in combination with biofilms for wastewater treatments. In these systems, biofilm needs to grow on supports to be able to filtrate. The efficiency of such filters is strongly related to the characteristics of the materials of the biofilm carrier, such as porosity and surface area.[83] In particular, supports with higher porosity and specific surface area have been found to be more efficient.[83] Over time, several polymeric materials have been tested out, such as polyamide, polyethylene, polypropylene,[84] polyvinyl chloride [83] and polyurethane.[77,85] Among these, polyurethane was found to be the most suitable for the job,[77,86,87] and is, nowadays, one most used polymer for wastewater treatment biofilm carriers. For instance, PU is used as a biofilm foam matrix in moving bed biofilm reactors (MMRB), where biofilms are used to remove nitrogen, nitrite, and ammonium.[77] The use of PU in these systems has also shown higher efficiency in ammonium and TOC removal when compared to other carriers, such as polycaprolactone,[77] and a rate of denitrification up to 1.6 times higher than the one obtained in traditional activated sludge reactor.[88]

Biofilms have also been successfully used as biocatalysts for the production of a range of chemicals.[89-93] Biofilms offer to the production process the advantage of long term activity, continuous processing, and higher tolerance to toxic reactants.[76,94] One of the most successful biocatalyst process using a biofilm is the production of acetic acid from alcohol. For this process, bacteria from *Acetobacter* and *Gluconobaster* genera are used, which allow achieving a conversation rate of ~90 % of the added alcohol.[94] Other chemicals, such as ethanol or 2,3-butanediol are also produced using respectively *Zymomonas mobilis* or *Klebsiella pneumoniae* biofilms respectively.[78,89]

1.2.6 Human infections caused by biofilms

Biofilms can cause a wide range of problems in human health and in different industry sectors, such as fast-moving consumer goods (FMCG). In humans, approximately 65% of chronic infections, such as chronic prostatitis or chronic periodontitis, are believed to be caused by biofilms.[95] This is related to the resistance of biofilm to antibiotics and to the host immune system response, which causes treatment failure and, as a consequence, persistent infections.[95] For instance, *Pseudomonas aeruginosa*, *staphylococcus aureus,* and *Haemophilus influenza* biofilms have been predominantly found in chronic rhinosinusitis (CRS) patients.[96,97] These biofilms act by damaging the mucosa and decreasing muco-ciliary clearance, which promotes bacterial persistence and causes persistent infections.[97,98] *P. aeoruginosa* has also been found in other chronic diseases, e.g., otitis media (OM) and cystic fibrosis (CF).[99,100] Furthermore, biofilms have also been found on medical device surfaces such as surgical implants and catheters, causing implantable device and prosthesis related infections.[101-103] Bacterial colonization is also a major problem in wound

dressing and healing treatments.[104] Wound dressings usually have a porous structure and are composed of different biomaterials, such as cellulose, alginate or collagen.[104,105] The porous structure helps (i) to create and maintain a moisturized environment, which is fundamental for generating optimal conditions for wound healing, (ii) to enhance epidermal migration, (iii) to allows air exchange between the eternal environment and the wound and (iv) to provides protection against dust.[106,107] However, the presence of moisture can also enhance bacteria and biofilm growth, causing wound infections. In particular, *Staphylococcus aureus* and *Pseudomonas aeruginosa* have often been found in wounds and wound dressing, causing infections and a decrease of the wound healing process efficiency.[104]

1.2.7 Problems related to biofilms in industry

Biofilm surface contamination have also major implications in different industrial processes ranging from paper production to oil drilling and food processing.[108] In particular, in food industry, biofilms are the cause of significant economic and health issues,[109] due to food spoilage and the pathogenic nature of the contaminant bacteria species (*Vibrio* spp, *Pseudomonas* spp., and *Listeria monocytogenes*).[109-111] Many of these problems are related to the difficulties of removing biofilm from food processing equipment, due to high resistance of biofilms to cleaning and disinfection (C&D).[112] Indeed, biofilms have been found to be resistant to most of the common C&D agents, such as hydrogen peroxide, iodine, paracetic acid, ozone, surfactants, and quaternary ammonium compounds.[112,113] Moreover, these chemicals can cause metallic erosion of the working equipment,[113] which can pose a huge problem for the production

process. Recent strategies for biofilms removal have employed enzymes as a primary cleaning agents.[114] Enzymes are able to both degrade the EPS matrix macromolecules, causing a weakening of the biofilm matrix structure, and to promote cell lysis, causing the death of bacteria.[113,115] Once the matrix is weakened, the biofilm results easier to remove by mechanical cleaning procedures (brushing, flow, or pressure).[115] Moreover, a weakened matrix results less protective for bacteria, making them more susceptible to normal C&D agents.[115] However, enzymes are strongly substrate-specific[113] and, as described in section 1.2.1, the composition of the EPS matrix varies from species to species.[32-35] Thus, in order to successfully degrade the EPS components, a specific enzyme should be introduced according to the EPS composition,[113] which limit the range of use of these products.

1.2.8 Problems related to biofilms in domestic environments

The proliferation of bacteria and biofilms proliferation cause problems not only in the industry sector but also in domestic environments. Common domestic environments, where bacteria in high concentration, are washing machines, toilets, cleaning utensils and clothes. Washing machines in particular can contain more pathogenic biofilms (*P. aeruginosa* and *K. pneumoniae*) than toilets.[116] This problem has partially increased in the last twenty-thirty years due to substantial variations in the chemical composition of detergents and laundry processes for economic and environmental reasons, which required lower washing temperature and fewer water demands.[117] These goals have been achieved by the introduction of enzymes within washing detergents, and the use of liquid detergents, most of whom do not contain disinfecting bleaching agents.[116] As a result of these variations, most common washing cycles are performed at

temperatures between 30 to 40 °C.[118,119] While there are advantages for the environment and economy, the use of such low temperatures does not remove bacteria from clothes or washing machines. For instance, *S. aureus, S. epidermidis*, *P. aeruginosa,* and *E. coli* have been found to survive laundry programs up to 50 °C.[120] To eliminate biofilms and bacteria, temperatures of 60 °C or higher are needed.[117] Lower temperatures may be sufficient for bacteria disinfection, but only if bleaches are present within the detergents.[121] However, while bleach agents are commonly present in hospital laundry detergents, they are not commonly found in household detergents.[122] The presence of bacteria in washing machines causes problems non only for the washing machines themselves, but can also cross-contaminate clothes. This cross-contamination can induce malodour in washed clothes,[120] which gives the idea to the consumer that the detergent is not performing as expected.

Apart for washing machines, kitchens and bathrooms are also known to be incubators for bacteria and biofilm due to constant body contact with surfaces and food handling.[123] The kitchen, in particular, has proved to be the room with most bacteria and biofilms in the house.[124,125] Part of this is due to the presence of kitchen sponges that were found to be the second-highest bacteria container of the house.[124] Kitchen sponges are primarily made from open-cell polyurethane foams, also known as flexible polyurethane foams (FPU). FPU foams usually have high porosity (> 90 %) and a large surface area. These properties, together with the intrinsic liquid high retention, make FPU foams an ideal media for biofilm growth. Within kitchen FPU sponges, many different species of bacteria have been isolated, such as *Salmonella* spp,[126] *Escherichia coli* spp,[127,128] *Staphylococcus* spp,[127,129] and *Klebsiella* spp.[127-129]

Moreover, due to their use, sponges spread bacteria on surfaces leading to food and body cross-contamination, which can then result in foodborne diseases.[127]

1.2.7 Biofilm removal in kitchen sponges

To reduce, and remove, bacteria and biofilms from kitchen sponges, different products have been produced and tested, such as bleach solutions[130] and dishwashing liquids.[128,131] The use of bleach solutions has resulted in a reduction of > 99.9 % of bacteria population in sponges when these have been left soaking in the solution for 5 minutes or more.[130] However, these percentages tend to decrease when food and other substances are present within the sponge.[132] Similar results have been found for the use of dishwashing liquids in contaminated sponges.[128,133] Indeed, the concentration of *Salmonella* spp., *Pseudomonas* spp. and *E. coli* was found to slightly reduce in laboratory tests, were sponges were contaminated with milk, lettuce, or raw kitchen breast fillet suspensions.[128,133] However, no variation in bacteria concentration was observed in used sponges collected from households that contained different food residues.[128,133] These studies suggested that bacteria removal in sponges depends on various factors and that food residues within the sponge strongly affect the efficiency of detergents. Because of this, and limitations in the use of antibacterial in washing products, FMCGs companies have focused on developing detergents which can remove food from sponges to tackle the bacteria contamination problem. However, to fully understand how detergents act on food trapped within open-cell porous media, a full understanding of the fluid dynamic of liquids within the sponges is required. Unfortunately, nowadays this is still poorly understood, and new methodologies need to be developed to increase knowledge on fluid dynamics within sponges, as well as

on the bacteria and biofilm development within sponges and their relations with food residues.

1.3 Imaging biofilm in porous media.

Whether it is for understanding how biofilms grow in porous media, or how they interact with food residues and detergent within kitchen sponges, their visualization within the foam is extremely important. Unfortunately, the visualization of biofilm in porous media is not easy, since porous media are generally opaque and have irregular shapes. For instance, optical techniques are strongly affected by the irregularity and opacity of the porous media because the former causes image blurriness and background signal, while the latter limits the depth of field of observation.[134] The techniques used to visualize biofilm in porous media can be divided into two categories: invasive and non-invasive.[134] The techniques in the first category, which comprises scanning electron microscopy (SEM), transmission electron microscopy (TEM), and confocal laser scanning microscopy (CLSM), require pre-treatments that can alter the structure of the biofilm and porous media.[134-136] The second, containing magnetic resonance imaging (MRI) or ultrasound, have negligible effects on biofilm, but generally suffer from low resolutions or low selectivity.

1.3.1 Scanning electron microscopy

SEM is able to visualize biofilms on sponges surface with high resolution.[137,138] For instance, using SEM, Ribeiro *et al* [138] were able to observe and characterize three biofilm colonization phases on PU foam, where the first two, cell adhesion and EPS secretion, were related to biofilms formation, while the third, with microgranules

formation, corresponded to the biofilm establishment. While offering the possibility of such high resolution (≈ 10 nm), SEM requires pre-treatment of the specimen, including fixation, drying, and coating with a conductive material,[139] which can alter the sample structure, and does not allow *in-situ* visualization. Of particular importance is that drying can modify the biofilm morphology, because of the collapse of the EPS matrix.[135,136] Moreover, SEM is well-placed to visualize biofilms on the surfaces of the sample, but cannot provide images of biofilms within the sponge,[140] which can be useful for some applications. Some of the SEM problems can be overcome by using environmental SEM (ESEM) which enables matrix preservation, thanks to the use of only moderate vacuum, does not require a conductive coating, and offers the possibility to perform analysis in moist atmospheric conditions.[139,141] However, the absence of a conductive coating generates difficulties in EPS visualization for biofilm growth in absence of metals,[142] causing great variation of the images across the sample.[139]

1.3.2 Confocal laser scanning microscopy

CLSM has become extremely important for understanding the structure of biofilms, through visualization of their three-dimensional structure in vivo.[14,143] CLSM has the advantage of analysing biofilms in their fully hydrated state, even on non-transparent surfaces.[144,145] Moreover, thanks to various dyes that can selectively target bacteria, nucleic acids, EPS polymers, or proteins, the different components of biofilms can be selectively visualized.[146] CLSM can provide information on the spatial structure of biofilm,[137,146] and has shown differences in the biofilm architectures and biofilms biomass location depending on the bacteria species forming the biofilm.[14] For example, an inverted pyramid structure has been visualized for *Vibrio*

parahaemolyticus biofilm, with the biofilm biomass mostly located at the biofilm-liquid interface.[147] Conversely, P *aerouginosa* biofilm have been found to have cell mass mostly located close to the biofilm base.[147] CLSM has also enabled the visualization of biofilms under flow conditions, which have revealed a complex structure composed of water channels, within the EPS matrix, separating cell clusters.[14,148]Further CLSM studies produced by recording images of latex bead fluorescently labels at different times within biofilms have discovered that these channels are used by biofilms to transport liquids to the different parts of the structure.[149] CLSM has also been used to study the effect of antimicrobial, containing silver sulfadiazine, and non-antimicrobial surfactant-based wound dressing in the development of biofilms.[150] Confocal images have shown how both microbial and non-antimicrobial surfactants cause the dispersion of the biofilm and the lysis of the bacteria.[150] While offering good image resolution and high flexibility thanks to the different fluorescent labels that can be used, CLSM suffers some of the same problems as SEM. Indeed, CLSM needs to pre-treat the sample, which in this case requires staining bacteria with fluorescents dyes,[140] that could have a negative impact on the bacteria cellular metabolism.[151] The staining process also causes a problem when the biofilm is within a sponge, because of the staining of the sponge itself. The difficulty of removing the stain from the sponge, makes difficult the separation, within the image, between the biofilm and the sponge structure. To avoid sponge staining and facilitate the visualization of biofilm within it, CLSM can be used in combination with fluorescent in-situ hybridization (FISH) technique. FISH uses fluorescent-labelled nucleic acid probes to attach the bacteria to specific rRNA regions,[152] making sure the sponge is not stained. Biofilms within the sponge are then visualized with CLMS using the fluorescence signal of these nucleic acid probes, while

the sponge structure is visualized using the autofluorescence of the sponge.[137] The images of biofilms and the sponge are then overlapped using post-production software, such as ImageJ[153] or Adobe Photoshop[154], to highlight the position of biofilms in relation to the sponge structure.[137] While the combination of CLSM and FISH enables the visualization of biofilm in kitchen sponges, the requirement of a long hybridization procedure (2 h at 42 °C) and the long washing up of the sample (10 min at 43 °C),[137] do not allow in-situ visualization of biofilm formation within the sponge.

1.3.3 X-ray computed tomography

X-ray computed tomography, compared to CLSM and SEM, can provide non-invasive and non-destructive 3D images of the interiors of porous media[155], thus can visualize biofilm growth within the sponge. [140] Images of the interior of opaque systems, like porous media, are produced by mapping the absorption of X-rays through the sample.[155] The absorption rate depends on the atomic mass of the objects imaged, thus it is related to the chemical composition of the sample.[155] If the sample components have different attenuation coefficients, contrast can be produced and a clear image of sample components can be produced. Unfortunately, biofilms do not provide sufficient difference in contrast with plastic foam matrix. Indeed, biofilms, foam matrices, and aqueous phases have similar X-ray attenuation coefficients, making it challenging to distinguish between the three components in X-ray computed tomography experiments. Where this is the case, contrast agents need to be used to increase the contrast between the three components. Over the years, different approaches and different contrast agents have been used to tackle the problem, which

include the staining of the porous media[156] or the biofilm.[157] For the staining of porous media, particulate barium sulphate suspensions have been used. $BaSO_4$ particles label pores non-colonized by biofilms, while they do not interact with the biofilms.[156] However, since $BaSO_4$ is a heavy compound, it causes sedimentation and aggregation of the particles, which lead to image artefacts and can induce biofilm detachment.[156] For biofilm staining, silver-coated microparticles (10 μm) have been deposited at the biofilm surface, which allowed the visualization of the liquid-biofilm interface.[157] Unfortunately, this method suffers from a non-homogenous distribution of microparticles on biofilm, causing great variation of the images across the sample.[157] Apart for the difficulty in finding appropriate contrast agents, X-ray computed tomography can also suffer from problems caused by the energy of the X-rays used. Indeed, the high energy required for the measurements can potentially damage bacteria during the exposure.[134]

1.3.4 MRI visualization of Biofilms

As biofilms are composed of up to 97% of water, mostly located in the EPS.[1] they can be readily visualised by MRI. MRI typically uses the signal from water protons (^1H) to produce images, so the high percentage of water within biofilms allows them to be directly imaged. Moreover, being non-invasive, MRI allows measurements in the original biofilm cultivation environment, making it possible to monitor the same biofilm as it grows.[158] It is also then possible to follow the same biofilm under a range of conditions that can maybe inhibit their growth and to probe biofilms in a way that it is possible to determine the factors that influence biofilm growth. However, considering biofilms mostly grow in aqueous environments, there is a question concerning whether

there is sufficient contrast between the biofilm and surrounding water, using ^{1}H MRI. Fortunately, MRI offers a range of parameters which through contrast can be achieved, such as NMR relaxation times, flow, and diffusion. For instance, the mobility of water in biofilm is restricted, leading to an enhanced NMR T_1 and T_2 relaxation time. Typically, T_2 relaxation time of pure bulk water is around 1-2 s, while NMR T_2 relaxation time in biofilm is in the order of 100-200 ms.[159] This variation in T_2 has been used to produce contrast. T_2 - and T_1-weighted images have been used to investigate the variations in the structure of different biofilms, such as sludge flocs, carrier-based biofilms, and granulated biofilms.[160] Sludge flocs biofilm were found to be composed of a loose network with small-scale heterogeneity.[160] Carrier-based biofilms and granular biofilms instead showed a more heterogenous internal structure.[160] Studies have also investigated biofilm growth within porous media, like MMBR, to understand how the growth impact the porous media structure. Images of porous media are generally produced indirectly by imaging fluids, commonly water, contained within the voids of the porous media.[161,162] As for water in biofilms, the mobility of water in porous media pores is also restricted because of the its confinement within pores. Thus, a reduction in NMR T_1 and T_2 relaxation times is also observed for water in pores, which makes it more difficult to achieve contrast between the biofilm and bulk water within the porous media. Fortunately, while the NMR T_2 relaxation times of bulk water in pores are similar to the ones of water in biofilm, T_1 are generally different, which can make it possible to obtain a proper contrast acquiring T_1 weighted images.[163] T_1-weighted images have been used to study the development and impact that biofilms growth has on the pore structure of a homogeneous porous media model.[158] The images revealed a heterogeneous spatial distribution of the biomass within the porous media as a

function of biofilm growth. while the homogeneous porous media was transformed into a complex heterogeneous system.[158]

In addtion to MR relaxation time imaging, diffusion MRI has also been used to explore the structure of biofilms and how this structure changes over time. The diffusion coefficient of water within a biofilm is approximately 20 – 30% lower than the diffusion coefficient of free water. [164] Thus once again it is possible to use this variation to generate contrast between biofilms and bulk water. MRI diffusion measurements have been performed on both biofilm mimics[165] (alginate) and real biofilms.[166-169] Time-resolved MRI diffusion images, on *Shewanella oneidensis* biofilms, has shown various diffusion coefficients within the biofilm, suggesting heterogeneity in the biofilm structure.[169] This heterogeneity was found to be higher at the bottom of the biofilms, and also increasing with biofilm ageing, with the diffusion coefficient becoming more restricted with time [169] Similar results were also found for *phormidium* biofilms.[166]

Magnetic resonance imaging can also be used to visualise flow.[170-172] Flow MRI has been applied to the study of biofilms, investigating the effect of fluid flow on biofilm detachment and deformations[173,174], as well as the determination of how biofilms alter the flow pattern in systems like pipes or moving bed biofilm reactors.[175] For example, the study of local flow velocities through T_2 velocity maps within an MMBR, showed a decrease of flow velocities toward the biofilms' surface.[175] Moreover, the flow resistance was found to increase as a function of biofilm growth, which can cause biofilm detachment.[175] Detachment of the biofilm was also observed in regions of higher shear stress.[174,176] An important sector in which flow-MRI has also been

employed is biofilms growth within porous media, like packed bead reactor[177] or homogeneous porous media model[158] (e.g. glass beads).In these systems, flow images were used to link biofilms growth to the hydrodynamic dispersion within pores, providing results suggesting a connection between biofilm growth and the transition from normal diffusive transport to anomalous diffusive transport within the pores.[158,178]

1.4 Thesis outline

The aim of this research project was to develop new multi-vision methodology to visualize the growth of biofilms in porous media in a non-invasive way, which could enable to monitor biofilm development in-situ and in time, and to correlate this growth to porous media properties and food viability within the media. In order to achieve this, we focused on three main objectives: (i) develop new way to characterize polymeric open-cell porous media, when the media are saturated with liquids; (ii) establish new ways to image food and biofilms within porous media in a non-invasive way, which could enable to monitor biofilm development in-situ and in real-time; (ii) correlate this growth to porous media properties and food viability within the media. In this vision, MRI has been used in conjunction with other optical imaging methodologies to characterise the structure, growth, and properties of biofilms in several different environments, with a particular focus on open-cell polyurethane sponges.

Chapter 2 contains the description and characterization of porous media and describes the theoretical background of NMR, MRI, X-ray μCT, and CLSM, which have been used to perform the study.

Chapter 3 focuses on the characterization of an open-cell polyurethane foam, whose properties, such as pore size distribution and porosity, are fundamental for the understanding of the relation between the foam structure and biofilms development. NMR and MRI have been used to evaluate the pore size distribution of a PU open-cell foam. By combining the pore size distribution determined with X-ray μCT, with the MRI and bulk T_2 relaxation time distributions, and their variation upon compression, a correlation between the pore size and the T_2 relaxation times in PU open-cell foam was found, which allows the direct measure of the pore size with magnetic resonance methods.

In chapter 4, the growth of biofilms and the distribution of food within PU foams are investigated. Being able to visualize how food is distributed within a sponge can help to understand how this is linked to biofilm development. For the study, CLSM images of biofilms in sponge and MRI chemical shift selective images (CHESS) of water and oil in sponge are presented. The former shows the difficulties in using CLSM to visualize biofilm in PU foam due to the absorbance of the contrast agent by the polymeric matrix. The latter shows the possibility to use CHESS to spatially visualize possible biofilm nutrients within PU foams.

Chapter 5 focuses on the visualization of biofilms using MRI, with the aim to develop new ways to image biofilms within porous media without the need for contrast agents. In particular, MRI chemical exchange saturation transfer (CEST) method was tested as a new method to visualize biofilm without using contrast agents. Analyses were performed on alginate gel, chosen as biofilm mimic material due to its presence in

different biofilm EPS. The results show the possibility of using CEST for biofilm visualization.

1.5 References

1 Branda, S. S., Vik, S., Friedman, L. & Kolter, R. Biofilms: the matrix revisited. *Trends Microbiol.* **13**, 20, doi:10.1016/j.tim.2004.11.006 (2005).

2 Davey, M. E. & O'toole, G. A. Microbial biofilms: from ecology to molecular genetics. *Microbiol. Mol. Biol. Rev.* **64**, 847 (2000).

3 von Eiff, C., Jansen, B., Kohnen, W. & Becker, K. Infections associated with medical devices. *Drugs* **65**, 179 (2005).

4 Dunsmore, D. & Thomson, M. Bacteriological control of food equipment surfaces by cleaning systems. II. Sanitizer effects. *J. Food Prot.* **44**, 21 (1981).

5 Chmielewski, R. & Frank, J. Biofilm formation and control in food processing facilities. *Compr. Rev. Food Sci. Food Saf.* **2**, 22 (2003).

6 Bower, C., McGuire, J. & Daeschel, M. The adhesion and detachment of bacteria and spores on food-contact surfaces. *Trends Food Sci. Technol.* **7**, 152 (1996).

7 Wirtanen, G., Husmark, U. & Mattila-Sandholm, T. Microbial evaluation of the biotransfer potential from surfaces with Bacillus biofilms after rinsing and cleaning procedures in closed food-processing systems. *J. Food Prot.* **59**, 727 (1996).

8 Holah, J. T. Disinfection of food production areas. *Revue Scientifique et Technique-Office International des Epizooties* **14**, 343 (1995).

9 Wolcott, R. D. *et al.* A review of iodine-based compounds, with a focus on biofilms: results of an expert panel. *J. Wound Care* **29**, S38 (2020).

10 Armon, R., Laot, N., Lev, O., Shuval, H. & Fattal, B. Controlling biofilm formation by hydrogen peroxide and silver combined disinfectant. *Water Sci. Technol.* **42**, 187 (2000).

11 Stojicic, S., Shen, Y. & Haapasalo, M. Effect of the source of biofilm bacteria, level of biofilm maturation, and type of disinfecting agent on the susceptibility of biofilm bacteria to antibacterial agents. *J. Endod.* **39**, 473 (2013).

12 Ronner, A. B. & Wong, A. C. Biofilm development and sanitizer inactivation of Listeria monocytogenes and Salmonella typhimurium on stainless steel and Buna-n rubber. *J. Food Prot.* **56**, 750 (1993).

13 Lagaron, J. M., Ocio, M. J. & Lopez-Rubio, A. *Antimicrobial polymers*. (John Wiley & Sons, 2011).

14 Costerton, J. W., Lewandowski, Z., Caldwell, D. E., Korber, D. R. & Lappin-Scott, H. M. Microbial biofilms. *Annu. Rev. Microbiol.* **49**, 711, doi:10.1146/annurev.mi.49.100195.003431 (1995).

15 Bar-On, Y. M., Phillips, R. & Milo, R. The biomass distribution on Earth. *Proc. Natl. Acad. Sci.* **115**, 6506 (2018).

16 Satpathy, K. Effects of biofouling on the cooling water quality of a nuclear power plant. *Bull. Electrochem.* **15**, 143 (1999).

17 Costerton, J. W., Stewart, P. S. & Greenberg, E. P. Bacterial biofilms: a common cause of persistent infections. *Science* **284**, 1318 (1999).

18 Flemming, H.-C. *et al.* Biofilms: an emergent form of bacterial life. *Nat. Rev. Microbiol.* **14**, 563 (2016).

19 Rasamiravaka, T., Labtani, Q., Duez, P. & El Jaziri, M. The formation of biofilms by Pseudomonas aeruginosa: a review of the natural and synthetic

compounds interfering with control mechanisms. *Biomed. Res. Int.* **2015**, 759348, doi:10.1155/2015/759348 (2015).
20 Konopka, A. What is microbial community ecology? *ISME J.* **3**, 1223 (2009).
21 Stewart, P. S. & Costerton, J. W. Antibiotic resistance of bacteria in biofilms. *Lancet* **358**, 135 (2001).
22 Flemming, H.-C. Biofilms and environmental protection. *Water Sci. Technol.* **27**, 1 (1993).
23 Anderson, G. & O'toole, G. in *Bacterial biofilms* 85 (Springer, 2008).
24 Mah, T.-F. C. & O'Toole, G. A. Mechanisms of biofilm resistance to antimicrobial agents. *Trends Microbiol.* **9**, 34 (2001).
25 Flemming, H.-C. & Wingender, J. The biofilm matrix. *Nat. Rev. Microbiol.* **8**, 623 (2010).
26 Hobley, L., Harkins, C., MacPhee, C. E. & Stanley-Wall, N. R. Giving structure to the biofilm matrix: an overview of individual strategies and emerging common themes. *FEMS Microbiol. Rev.* **39**, 649 (2015).
27 Flemming, H.-C. *et al.* Biofilm and the role of extracellular polymeric substance. *Advances in Biofilm Science and Engineering (Ryan RJJ, Williams DM & Charaf U, eds)*, 86 (2004).
28 Decho, A. W. in *Microbial sediments* 9 (Springer, 2000).
29 Neu, T. R., Flemming, H.-C. & Wingender, J. *Microbial extracellular polymeric substances: Characterization, structure and function*. (Springer, 1999).
30 Sutherland, I. W. Biofilm exopolysaccharides: a strong and sticky framework. *Microbiology* **147**, 3 (2001).
31 Klein, S. *et al.* Adaptation of Pseudomonas aeruginosa to various conditions includes tRNA-dependent formation of alanyl-phosphatidylglycerol. *Mol. Microbiol.* **71**, 551, doi:10.1111/j.1365-2958.2008.06562.x (2009).
32 Mann, E. E. & Wozniak, D. J. Pseudomonas biofilm matrix composition and niche biology. *FEMS Microbiol Rev* **36**, 893 (2012).
33 Stanley, N. R. & Lazazzera, B. A. Defining the genetic differences between wild and domestic strains of Bacillus subtilis that affect poly-γ-DL-glutamic acid production and biofilm formation. *Mol. Microbiol.* **57**, 1143 (2005).
34 O'Gara, J. P. ica and beyond: biofilm mechanisms and regulation in Staphylococcus epidermidis and Staphylococcus aureus. *FEMS Microbiol. Lett.* **270**, 179 (2007).
35 Ghafoor, A., Hay, I. D. & Rehm, B. H. Role of exopolysaccharides in Pseudomonas aeruginosa biofilm formation and architecture. *Appl. and Environ. Microbiol.* **77**, 5238 (2011).
36 Deretic, V., Govan, J., Konyecsni, W. & Martin, D. Mucoid Pseudomonas aeruginosa in cystic fibrosis: mutations in the muc loci affect transcription of the algR and algD genes in response to environmental stimuli. *Mol. Microbiol.* **4**, 189 (1990).
37 Wozniak, D. J. *et al.* Alginate is not a significant component of the extracellular polysaccharide matrix of PA14 and PAO1 Pseudomonas aeruginosa biofilms. *Proc. Natl. Acad. Sci. U.S.A.* **100**, 7907 (2003).
38 Flemming, H.-C., Neu, T. R. & Wozniak, D. J. The EPS matrix: the “house of biofilm cells”. *J. Bacteriol.* **189**, 7945 (2007).
39 Olsen, I. Biofilm-specific antibiotic tolerance and resistance. *Eur. J. Clin. Microbiol. Infect. Dis.* **34**, 877 (2015).

40 Oubekka, S. D., Briandet, R., Fontaine-Aupart, M.-P. & Steenkeste, K. Correlative time-resolved fluorescence microscopy to assess antibiotic diffusion-reaction in biofilms. *Antimicrob. Agents Chemother.* **56**, 3349 (2012).

41 Ordax, M., Marco-Noales, E., López, M. M. & Biosca, E. G. Exopolysaccharides favor the survival of Erwinia amylovora under copper stress through different strategies. *Res. Microbiol.* **161**, 549 (2010).

42 Métivier, R., Bourven, I., Labanowski, J. & Guibaud, G. Interaction of erythromycin ethylsuccinate and acetaminophen with protein fraction of extracellular polymeric substances (EPS) from various bacterial aggregates. *Environmental Science and Pollution Research* **20**, 7275 (2013).

43 Decho, A. W., Visscher, P. T. & Reid, R. P. in *Geobiology: Objectives, Concepts, Perspectives* 71 (Elsevier, 2005).

44 Grumbein, S., Opitz, M. & Lieleg, O. Selected metal ions protect Bacillus subtilis biofilms from erosion. *Metallomics* **6**, 1441 (2014).

45 Körstgens, V., Flemming, H.-C., Wingender, J. & Borchard, W. Influence of calcium ions on the mechanical properties of a model biofilm of mucoid Pseudomonas aeruginosa. *Water Sci. Technol.* **43**, 49 (2001).

46 Rose, R. The role of calcium in oral streptococcal aggregation and the implications for biofilm formation and retention. *Biochim. Biophys. Acta. Gen. Subj.* **1475**, 76 (2000).

47 Battin, T. J., Besemer, K., Bengtsson, M. M., Romani, A. M. & Packmann, A. I. The ecology and biogeochemistry of stream biofilms. *Nat. Rev. Microbiol.* **14**, 251 (2016).

48 González-Pastor, J. E., Hobbs, E. C. & Losick, R. Cannibalism by sporulating bacteria. *Science* **301**, 510 (2003).

49 Ellermeier, C. D., Hobbs, E. C., Gonzalez-Pastor, J. E. & Losick, R. A three-protein signaling pathway governing immunity to a bacterial cannibalism toxin. *Cell* **124**, 549 (2006).

50 López, D., Vlamakis, H., Losick, R. & Kolter, R. Cannibalism enhances biofilm development in Bacillus subtilis. *Mol. Microbiol.* **74**, 609 (2009).

51 Pinchuk, G. E. *et al.* Utilization of DNA as a sole source of phosphorus, carbon, and energy by Shewanella spp.: ecological and physiological implications for dissimilatory metal reduction. *Appl. Environ. Microbiol.* **74**, 1198 (2008).

52 Mulcahy, H., Charron-Mazenod, L. & Lewenza, S. Pseudomonas aeruginosa produces an extracellular deoxyribonuclease that is required for utilization of DNA as a nutrient source. *Environ. Microbiol.* **12**, 1621 (2010).

53 Karimi, A., Karig, D., Kumar, A. & Ardekani, A. Interplay of physical mechanisms and biofilm processes: review of microfluidic methods. *Lab on a Chip* **15**, 23 (2015).

54 Wilking, J. N. *et al.* Liquid transport facilitated by channels in Bacillus subtilis biofilms. *Proc. Natl. Acad. Sci. U.S.A.* **110**, 848 (2013).

55 Roberson, E. B. & Firestone, M. K. Relationship between desiccation and exopolysaccharide production in a soil Pseudomonas sp. *Appl. Environ. Microbiol.* **58**, 1284 (1992).

56 Flemming, H.-C. The perfect slime. *Colloids Surf. B. Biointerfaces* **86**, 251 (2011).

57 Oh, Y., Lee, N., Jo, W., Jung, W. & Lim, J. Effects of substrates on biofilm formation observed by atomic force microscopy. *Ultramicroscopy* **109**, 874 (2009).

58 Zheng, S. *et al.* Implication of surface properties, bacterial motility, and hydrodynamic conditions on bacterial surface sensing and their initial adhesion. *Frontiers in Bioengineering and Biotechnology* **9**, 82 (2021).

59 Zhu, X. *et al.* Polyion multilayers with precise surface charge control for antifouling. *ACS applied materials & interfaces* **7**, 852 (2015).

60 Kovačević, D. *et al.* Influence of polyelectrolyte multilayer properties on bacterial adhesion capacity. *Polymers* **8**, 345 (2016).

61 Chen, C., Petterson, T. r., Illergård, J., Ek, M. & Wågberg, L. Influence of cellulose charge on bacteria adhesion and viability to PVAm/CNF/PVAm-modified cellulose model surfaces. *Biomacromolecules* **20**, 2075 (2019).

62 Gottenbos, B., Van Der Mei, H., Busscher, H., Grijpma, D. & Feijen, J. Initial adhesion and surface growth of Pseudomonas aeruginosa on negatively and positively charged poly (methacrylates). *J. Mater. Sci. Mater. Med.* **10**, 853 (1999).

63 Ueshima, M., Tanaka, S., Nakamura, S. & Yamashita, K. Manipulation of bacterial adhesion and proliferation by surface charges of electrically polarized hydroxyapatite. *Journal of Biomedical Materials Research: An Official Journal of The Society for Biomaterials, The Japanese Society for Biomaterials, and The Australian Society for Biomaterials and the Korean Society for Biomaterials* **60**, 578 (2002).

64 Song, K., Lee, J., Choi, S.-O. & Kim, J. Interaction of surface energy components between solid and liquid on wettability, and its application to textile anti-wetting finish. *Polymers* **11**, 498 (2019).

65 Hwang, G., Lee, C.-H., Ahn, I.-S. & Mhin, B. J. Analysis of the adhesion of Pseudomonas putida NCIB 9816-4 to a silica gel as a model soil using extended DLVO theory. *J. Hazard. Mater.* **179**, 983 (2010).

66 Rigolin, M. S. M. *et al.* Effect of the aging of titanium and zirconia abutment surfaces on the viability, adhesion, and proliferation of cells and the adhesion of microorganisms. *The Journal of prosthetic dentistry* **122**, 564. e1 (2019).

67 Hori, K. & Matsumoto, S. Bacterial adhesion: from mechanism to control. *Biochem. Eng. J.* **48**, 424 (2010).

68 Sheng, X., Ting, Y. P. & Pehkonen, S. O. The influence of ionic strength, nutrients and pH on bacterial adhesion to metals. *J. Colloid Interface Sci.* **321**, 256 (2008).

69 Krasowska, A. & Sigler, K. How microorganisms use hydrophobicity and what does this mean for human needs? *Frontiers in cellular and infection microbiology* **4**, 112 (2014).

70 Bollen, C. M. *et al.* The influence of abutment surface roughness on plaque accumulation and peri-implant mucositis. *Clin. Oral Implants Res.* **7**, 201 (1996).

71 Wu, S. *et al.* Role of the surface nanoscale roughness of stainless steel on bacterial adhesion and microcolony formation. *ACS omega* **3**, 6456 (2018).

72 Paulsen, J. E., Oppen, E. & Bakke, R. Biofilm morphology in porous media, a study with microscopic and image techniques. *Water Sci. Technol.* **36**, 1 (1997).

73 Zhang, Y. *et al.* Non-Invasive Measurement, Mathematical Simulation and In Situ Detection of Biofilm Evolution in Porous Media: A Review. *Applied Sciences* **11**, 1391 (2021).

74 Carrel, M. *et al.* Biofilms in 3D porous media: Delineating the influence of the pore network geometry, flow and mass transfer on biofilm development. *Water Res.* **134**, 280 (2018).

75 Stoodley, P., Cargo, R., Rupp, C. J., Wilson, S. & Klapper, I. Biofilm material properties as related to shear-induced deformation and detachment phenomena. *J. Ind. Microbiol. Biotechnol.* **29**, 361 (2002).

76 Simpson, D. R. Biofilm processes in biologically active carbon water purification. *Water Res.* **42**, 2839 (2008).

77 Chu, L. & Wang, J. Comparison of polyurethane foam and biodegradable polymer as carriers in moving bed biofilm reactor for treating wastewater with a low C/N ratio. *Chemosphere* **83**, 63 (2011).

78 Maddox, I., Qureshi, N. & McQueen, J. Continuous production of 2, 3-butanediol from whey permeate using cells of Klebsiella pneumoniae immobilized on to bonechar. *N. Z. J. Diary Sci. Technol.* **23**, 127 (1988).

79 Galal-Gorchev, H. Chlorine in water disinfection. *Pure Appl. Chem.* **68**, 1731 (1996).

80 Leiknes, T. The effect of coupling coagulation and flocculation with membrane filtration in water treatment: A review. *J. Environ. Sci.* **21**, 8 (2009).

81 Kim, W. H., Nishijima, W., Shoto, E. & Okada, M. Pilot plant study on ozonation and biological activated carbon process for drinking water treatment. *Water Sci. Technol.* **35**, 21 (1997).

82 Dussert, B. The biological activated carbon process for water purification. *Water Eng. Manage.* **141**, 22 (1994).

83 Picanco, A., Vallero, M., Gianotti, E., Zaiat, M. & Blundi, C. Influence of porosity and composition of supports on the methanogenic biofilm characteristics developed in a fixed bed anaerobic reactor. *Water Sci. Technol.* **44**, 197 (2001).

84 Verrier, D., Mortier, B. & Albagnac, G. Initial adhesion of methanogenic bacteria to polymers. *Biotechnol. Lett.* **9**, 735 (1987).

85 Tommaso, G., Varesche, M., Zaiat, M., Vazoller, R. & Foresti, E. Morphological observation and microbial population dynamics in anaerobic polyurethane foam biofilm degrading gelatin. *Braz. J. Chem. Eng.* **19**, 287 (2002).

86 Huysman, P., Van Meenen, P., Van Assche, P. & Verstraete, W. Factors affecting the colonization of non porous and porous packing materials in model upflow methane reactors. *Biotechnol. Lett.* **5**, 643 (1983).

87 Zaiat, M., Vieira, L. G. T. & Foresti, E. Spatial and temporal variations of monitoring performance parameters in horizontal-flow anaerobic immobilized sludge (HAIS) reactor treating synthetic substrate. *Water Res.* **31**, 1760 (1997).

88 Daniel, L. M. C., Pozzi, E., Foresti, E. & Chinalia, F. A. Removal of ammonium via simultaneous nitrification–denitrification nitrite-shortcut in a single packed-bed batch reactor. *Bioresour. Technol.* **100**, 1100 (2009).

89 Bland, R., Chen, H., Jewell, W., Bellamy, W. & Zall, R. Continuous high rate production of ethanol by Zymomonas mobilis in an attached film expanded bed fermentor. *Biotechnol. Lett.* **4**, 323 (1982).
90 Tyagi, R. & Ghose, T. Studies on immobilized Saccharomyces cerevisiae. I. Analysis of continuous rapid ethanol fermentation in immobilized cell reactor. *Biotechnol. Bioeng.* **24**, 781 (1982).
91 Kunduru, M. R. & Pometto, A. Continuous ethanol production byZymomonas mobilis andSaccharomyces cerevisiae in biofilm reactors. *J. Ind. Microbiol.* **16**, 249 (1996).
92 Crueger, W., Crueger, A., Brock, T. D. & Brock, T. D. Biotechnology: a textbook of industrial microbiology. (1990).
93 Demirci, A., Pometto, A. L. & Johnson, K. E. Lactic acid production in a mixed-culture biofilm reactor. *Appl. Environ. Microbiol.* **59**, 203 (1993).
94 Qureshi, N., Annous, B. A., Ezeji, T. C., Karcher, P. & Maddox, I. S. Biofilm reactors for industrial bioconversion processes: employing potential of enhanced reaction rates. *Microb. Cell. Fact.* **4**, 24 (2005).
95 Yadav, M. K., Song, J.-J., Singh, B. P. & Vidal, J. E. in *New and Future Developments in Microbial Biotechnology and Bioengineering: Microbial Biofilms* 1 (Elsevier, 2020).
96 Foreman, A., Boase, S., Psaltis, A. & Wormald, P.-J. Role of bacterial and fungal biofilms in chronic rhinosinusitis. *Curr. Allergy Asthma Rep.* **12**, 127 (2012).
97 You, H. *et al.* Factors affecting bacterial biofilm expression in chronic rhinosinusitis and the influences on prognosis. *Am. J. Otolaryngol.* **32**, 583 (2011).
98 Galli, J. *et al.* Damage to ciliated epithelium in chronic rhinosinusitis: what is the role of bacterial biofilms? *Ann. Otol. Rhinol. Laryngol.* **117**, 902 (2008).
99 Coleman, A. *et al.* The unsolved problem of otitis media in indigenous populations: a systematic review of upper respiratory and middle ear microbiology in indigenous children with otitis media. *Microbiome* **6**, 199 (2018).
100 Høiby, N. *et al.* Pseudomonas aeruginosa infection in cystic fibrosis. Diagnostic and prognostic significance of Pseudomonas aeruginosa pre-cipitins determined by means of crossed immunoelectrophoresis. *Scand. J. Respir. Dis.* **58**, 65 (1977).
101 Khan, M. S., Rehman, S., Ali, M. A., Sultan, B. & Sultan, S. Infection in orthopedic implant surgery, its risk factors and outcome. *J. Ayub Med. Coll. Abbottabad* **20**, 23 (2008).
102 Oliveira, W. *et al.* Staphylococcus aureus and Staphylococcus epidermidis infections on implants. *J. Hosp. Infect.* **98**, 111 (2018).
103 Costerton, J., Montanaro, L. & Arciola, C. R. Biofilm in implant infections: its production and regulation. *Int. J. Artif. Organs* **28**, 1062 (2005).
104 Szymańska, M. *et al.* Glycoside hydrolase (PelAh) immobilization prevents Pseudomonas aeruginosa biofilm formation on cellulose-based wound dressing. *Carbohydr. Polym.* **246**, 116625 (2020).
105 Ismail, N. A., Amin, K. A. M., Majid, F. A. A. & Razali, M. H. Gellan gum incorporating titanium dioxide nanoparticles biofilm as wound dressing:

Physicochemical, mechanical, antibacterial properties and wound healing studies. *Materials Science and Engineering: C* **103**, 109770 (2019).
106 Jones, V., Grey, J. E. & Harding, K. G. Wound dressings. *BMJ* **332**, 777 (2006).
107 Dhivya, S., Padma, V. V. & Santhini, E. Wound dressings–a review. *Biomedicine* **5**, 1 (2015).
108 Stevenson, B. S. *et al.* Microbial communities in bulk fluids and biofilms of an oil facility have similar composition but different structure. *Environ. Microbiol.* **13**, 1078 (2011).
109 Mizan, M. F. R., Jahid, I. K. & Ha, S.-D. Microbial biofilms in seafood: a food-hygiene challenge. *Food Microbiol.* **49**, 41 (2015).
110 Møretrø, T. & Langsrud, S. Listeria monocytogenes: biofilm formation and persistence in food-processing environments. *Biofilms* **1**, 107 (2004).
111 Galie, S., García-Gutiérrez, C., Miguélez, E. M., Villar, C. J. & Lombó, F. Biofilms in the food industry: health aspects and control methods. *Front. Microbiol.* **9**, 898 (2018).
112 Fagerlund, A., Møretrø, T., Heir, E., Briandet, R. & Langsrud, S. Cleaning and disinfection of biofilms composed of Listeria monocytogenes and background microbiota from meat processing surfaces. *Appl. Environ. Microbiol.* **83** (2017).
113 Nahar, S., Mizan, M. F. R., Ha, A. J. w. & Ha, S. D. Advances and future prospects of enzyme-based biofilm prevention approaches in the food industry. *Compr. Rev. Food Sci. Food Saf.* **17**, 1484 (2018).
114 Nott, K. P., Heese, F. P., Paterson-Beedle, M., Macaskie, L. & Hall, L. D. Visualization of the function on a biofilm reactor by magnetic resonance imaging. *Can. J. Chem. Eng.* **83**, 68.
115 Boels, G. (Taylor & Francis, 2011).
116 Callewaert, C., Van Nevel, S., Kerckhof, F.-M., Granitsiotis, M. S. & Boon, N. Bacterial exchange in household washing machines. *Front. Microbiol.* **6**, 1381 (2015).
117 Terpstra, P. M. Domestic and institutional hygiene in relation to sustainability. Historical, social and environmental implications. *Int. Biodeterior. Biodegrad.* **41**, 169 (1998).
118 Arild, A.-H., Brusdal, R., Halvorsen-Gunnarsen, J., Terpstra, P. M. & Van Kessel, I. A. An investigation of domestic laundry in Europe: habits, hygiene and technical performance. *National Institute for Consumer Research, Oslo* (2003).
119 Pakula, C. & Stamminger, R. Electricity and water consumption for laundry washing by washing machine worldwide. *Energy efficiency* **3**, 365 (2010).
120 Munk, S., Johansen, C., Stahnke, L. H. & Adler-Nissen, J. Microbial survival and odor in laundry. *J. Surfactants Deterg.* **4**, 385 (2001).
121 Bloomfield, S. F., Cookson, B., Falkiner, F., Griffith, C. & Cleary, V. Methicillin-resistant Staphylococcus aureus, Clostridium difficile, and extended-spectrum β-lactamase–producing Escherichia coli in the community: Assessing the problem and controlling the spread. *Am. J. Infect. Control* **35**, 86 (2007).
122 Patel, S., Murray-Leonard, J. & Wilson, A. Laundering of hospital staff uniforms at home. *J. Hosp. Infect.* **62**, 89 (2006).
123 Cardinale, M., Kaiser, D., Lueders, T., Schnell, S. & Egert, M. Microbiome analysis and confocal microscopy of used kitchen sponges reveal massive

colonization by Acinetobacter, Moraxella and Chryseobacterium species. *Sci. Rep.* **7**, 1 (2017).
124 Ojima, M. *et al.* Hygiene measures considering actual distributions of microorganisms in Japanese households. *J. Appl. Microbiol.* **93**, 800 (2002).
125 Donofrio, R. S. *et al.* Are we aware of microbial hotspots in our household? *J. Environ. Health* **75**, 12 (2012).
126 Eliandra Mirlei, R., Diane, S., Williani Fabíola, G. & Eduardo Cesar, T. Microbiological contamination and disinfection procedures of kitchen sponges used in food services. *Food Sci. Nutr.* **2012** (2012).
127 Adiga, I. *et al.* Bacterial contamination in the kitchen: could it be pathogenic? (2012).
128 Erdoğrul, Ö. & Erbilir, F. Microorganisms in kitchen sponges. *Int. J. Food. Saf.* **6**, 17 (2005).
129 Marshall, B. M., Robleto, E., Dumont, T. & Levy, S. B. The frequency of antibiotic-resistant bacteria in homes differing in their use of surface antibacterial agents. *Curr. Microbiol.* **65**, 407 (2012).
130 Ikawa, J. Y. & Rossen, J. S. Reducing bacteria in household sponges. *J. Environ. Health* **62**, 18 (1999).
131 Nielsen, P., Brumbaugh, E. & Kananen, L. Evaluation of the use of liquid dishwashing compounds to control bacteria in kitchen sponges. *J. AOAC Int.* **85**, 107 (2002).
132 Bessems, E. The effect of practical conditions on the efficacy of disinfectants. *Int. Biodeterior. Biodegrad.* **41**, 177 (1998).
133 Kusumaningrum, H., Van Putten, M., Rombouts, F. & Beumer, R. Effects of antibacterial dishwashing liquid on foodborne pathogens and competitive microorganisms in kitchen sponges. *J. Food Prot.* **65**, 61 (2002).
134 Vafai, K. *Porous media: applications in biological systems and biotechnology*. (CRC Press, 2010).
135 Kachlany, S. C. *et al.* Structure and carbohydrate analysis of the exopolysaccharide capsule of Pseudomonas putida G7. *Environ. Microbiol.* **3**, 774 (2001).
136 Fassel, T. A. & Edmiston Jr, C. E. in *Methods Enzymol.* Vol. 310 194 (Elsevier, 1999).
137 Cardinale, M., Kaiser, D., Lueders, T., Schnell, S. & Egert, M. Microbiome analysis and confocal microscopy of used kitchen sponges reveal massive colonization by Acinetobacter, Moraxella and Chryseobacterium species. *Sci. Rep.* **7**, 1 (2017).
138 Ribeiro, R., Varesche, M. B. A., Foresti, E. & Zaiat, M. Influence of extracellular polymeric substances on anaerobic biofilms supported by polyurethane foam matrices. *Environ. Eng. Sci.* **20**, 249 (2003).
139 Priester, J. H. *et al.* Enhanced visualization of microbial biofilms by staining and environmental scanning electron microscopy. *J. Microbiol. Methods* **68**, 577 (2007).
140 Woznica, A., Karcz, J., Nowak, A., Gmur, A. & Bernas, T. Spatial architecture of nitrifying bacteria biofilm immobilized on polyurethane foam in an automatic biodetector for water toxicity. *Microsc. Microanal.* **16**, 550 (2010).

141 Little, B., Wagner, P., Ray, R., Pope, R. & Scheetz, R. Biofilms: an ESEM evaluation of artifacts introduced during SEM preparation. *J. Ind. Microbiol.* **8**, 213 (1991).
142 Darkin, M., Gilpin, C., Williams, J. & Sangha, C. Direct wet surface imaging of an anaerobic biofilm by environmental scanning electron microscopy: application to landfill clay liner barriers. *Scanning* **23**, 346 (2001).
143 de Beer, D. & Stoodley, P. Relation between the structure of an aerobic biofilm and transport phenomena. *Water Sci. Technol.* **32**, 11 (1995).
144 Roldán, M. & Hernández-Mariné, M. Exploring the secrets of the three-dimensional architecture of phototrophic biofilms in caves. *Int. J. Speleol.* **38**, 5 (2009).
145 Harrison, J. J. *et al.* The use of microscopy and three-dimensional visualization to evaluate the structure of microbial biofilms cultivated in the Calgary Biofilm Device. *Biol. Proced. Online* **8**, 194 (2006).
146 Neu, T. R. *et al.* Advanced imaging techniques for assessment of structure, composition and function in biofilm systems. *FEMS Microbiol. Ecol.* **72**, 1 (2010).
147 Wimpenny, J., Manz, W. & Szewzyk, U. Heterogeneity in biofilms. *FEMS Microbiol. Rev.* **24**, 661 (2000).
148 De Beer, D., Stoodley, P., Roe, F. & Lewandowski, Z. Effects of biofilm structures on oxygen distribution and mass transport. *Biotechnol. Bioeng.* **43**, 1131 (1994).
149 Stoodley, P., DeBeer, D. & Lewandowski, Z. Liquid flow in biofilm systems. *Appl. Environ. Microbiol.* **60**, 2711 (1994).
150 Percival, S. L., Mayer, D. & Salisbury, A. M. Efficacy of a surfactant-based wound dressing on biofilm control. *Wound Repair Regen.* **25**, 767 (2017).
151 Ullrich, S., Karrasch, B., Hoppe, H., Jeskulke, K. & Mehrens, M. Toxic effects on bacterial metabolism of the redox dye 5-cyano-2, 3-ditolyl tetrazolium chloride. *Appl. Environ. Microbiol.* **62**, 4587 (1996).
152 Cardinale, M., Vieira de Castro Jr, J., Müller, H., Berg, G. & Grube, M. In situ analysis of the bacterial community associated with the reindeer lichen Cladonia arbuscula reveals predominance of Alphaproteobacteria. *FEMS Microbiol. Ecol.* **66**, 63 (2008).
153 Rasband, W. S. (Bethesda, MD, 1997-2018).
154 (Peachpit Press, Berkeley, CA, 2004).
155 Al-Raoush, R. & Willson, C. Extraction of physically realistic pore network properties from three-dimensional synchrotron X-ray microtomography images of unconsolidated porous media systems. *J. Hydrol.* **300**, 44 (2005).
156 Davit, Y. *et al.* Imaging biofilm in porous media using X-ray computed microtomography. *J. Microsc.* **242**, 15 (2011).
157 Iltis, G. C., Armstrong, R. T., Jansik, D. P., Wood, B. D. & Wildenschild, D. Imaging biofilm architecture within porous media using synchrotron-based X-ray computed microtomography. *Water Resour. Res.* **47** (2011).
158 Seymour, J. D., Gage, J. P., Codd, S. L. & Gerlach, R. Magnetic resonance microscopy of biofouling induced scale dependent transport in porous media. *Adv. Water Resour.* **30**, 1408, doi:10.1016/j.advwatres.2006.05.029 (2007).
159 Herrling, M. P., Lackner, S., Nirschl, H., Horn, H. & Guthausen, G. in *Annual Reports on NMR Spectroscopy* Vol. 97 163 (Elsevier, 2019).

160 Herrling, M. P. *et al.* NMR Investigation of Water Diffusion in different Biofilm Structures. *Biotechnol. Bioeng.* (2017).
161 Borgia, G., Bortolotti, V. & Fantazzini, P. Changes of the local pore space structure quantified in heterogeneous porous media by 1 H magnetic resonance relaxation tomography. *J.Appl. Phys.* **90**, 1155 (2001).
162 Attard, J. *et al.* Spatially resolved T1 relaxation measurements in reservoir cores. *Magn. Reson. Imaging* **9**, 815 (1991).
163 Hoskins, B. C., Fevang, L., Majors, P. D., Sharma, M. M. & Georgiou, G. Selective imaging of biofilms in porous media by NMR relaxation. *J. Magn. Reson.* **139**, 67 (1999).
164 Eberl, H. *et al. Mathematical modeling of biofilms*. (IWA, 2006).
165 Fabich, H. T. *et al.* Microbial and algal alginate gelation characterized by magnetic resonance. *J. Biotechnol.* **161**, 320 (2012).
166 Ramanan, B., Holmes, W. M., Sloan, W. T. & Phoenix, V. R. Magnetic resonance imaging of mass transport and structure inside a phototrophic biofilm. *Curr. Microbiol.* **66**, 456 (2013).
167 Phoenix, V. & Holmes, W. Magnetic resonance imaging of structure, diffusivity, and copper immobilization in a phototrophic biofilm. *Appl. Environ. Microbiol.* **74**, 4934 (2008).
168 McLean, J. S., Ona, O. N. & Majors, P. D. Correlated biofilm imaging, transport and metabolism measurements via combined nuclear magnetic resonance and confocal microscopy. *The ISME journal* **2**, 121 (2008).
169 Renslow, R. S. *et al.* In situ effective diffusion coefficient profiles in live biofilms using pulsed-field gradient nuclear magnetic resonance. *Biotechnol. Bioeng.* **106**, 928 (2010).
170 La Heij, E., Kerkhof, P., Kopinga, K. & Pel, L. Determining porosity profiles during filtration and expression of sewage sludge by NMR imaging. *AIChE journal* **42**, 953 (1996).
171 Van As, H. & Lens, P. Use of 1H NMR to study transport processes in porous biosystems. *J. Ind. Microbiol. Biotechnol.* **26**, 43, doi:10.1038/sj.jim.7000087 (2001).
172 Seymour, J. D., Codd, S. L., Gjersing, E. L. & Stewart, P. S. Magnetic resonance microscopy of biofilm structure and impact on transport in a capillary bioreactor. *J. Magn. Reson.* **167**, 322, doi:10.1016/j.jmr.2004.01.009 (2004).
173 Stewart, P. S. Mini-review: convection around biofilms. *Biofouling* **28**, 187 (2012).
174 Manz, B., Volke, F., Goll, D. & Horn, H. Investigation of biofilm structure, flow patterns and detachment with magnetic resonance imaging. *Water Sci. Technol.* **52**, 1 (2005).
175 Herrling, M. P., Guthausen, G., Wagner, M., Lackner, S. & Horn, H. Determining the flow regime in a biofilm carrier by means of magnetic resonance imaging. *Biotechnol. Bioeng.* **112**, 1023 (2015).
176 Manz, B., Volke, F., Goll, D. & Horn, H. Measuring local flow velocities and biofilm structure in biofilm systems with magnetic resonance imaging (MRI). *Biotechnol. Bioeng.* **84**, 424 (2003).
177 Metzger, U., Lankes, U., Hardy, E. H., Gordalla, B. C. & Frimmel, F. H. Monitoring the formation of an Aureobasidium pullulans biofilm in a bead-

packed reactor via flow-weighted magnetic resonance imaging. *Biotechnol. Lett.* **28**, 1305, doi:10.1007/s10529-006-9091-x (2006).

178 Seymour, J. D., Gage, J. P., Codd, S. L. & Gerlach, R. Anomalous fluid transport in porous media induced by biofilm growth. *Phys. Rev. Lett.* **93**, 198103, doi:10.1103/PhysRevLett.93.198103 (2004).

2 METHODS AND THEORY

In this thesis, magnetic resonance and X-ray tomography techniques were employed to characterize polyurethane open-cell foams, image food sources within foams, and develop new methodologies to visualize biofilms. An overview of these techniques, and the characterisation of porous media, are provided in this chapter. Further insights can be found in the different textbooks and papers cited in the chapter.

2.1 NMR principles

Nuclear magnetic resonance (NMR) provides information by using radio-frequency (RF) radiation to probe the environment of NMR active nuclei.[1] When placed in a static magnetic field ($\boldsymbol{B}_0$), nuclei precess at the *Larmor frequency* (ω), which is related to the gyromagnetic ratio, γ, and $\boldsymbol{B}_0$. [1,2]

$$\omega = -\gamma \boldsymbol{B}_0 \qquad 2.1$$

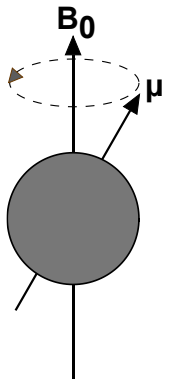


Figure 2.1Schematic diagram showing precession of the nuclear magnetic moment, μ , in a static magnetic field $\boldsymbol{B}_0$.

Moreover, the orientations and the energy levels for each atomic are quantised and nuclei distribute among the two.[2] For instance, For ^{1}H nuclei, two possible orientations are available, defined as spin-up and spin-down.[2] At equilibrium, multiple spins will populate these levels according to the Boltzmann distribution (equation 2.2)[2,3]

$$\frac{N_{-1/2}}{N_{+1/2}} = e^{\frac{-\Delta E}{kT}} \qquad 2.2$$

where T is the temperature, k is the Boltzmann constant, $N_{-1/2}$ and $N_{+1/2}$ are the population spin-down and spin-up states respectively.

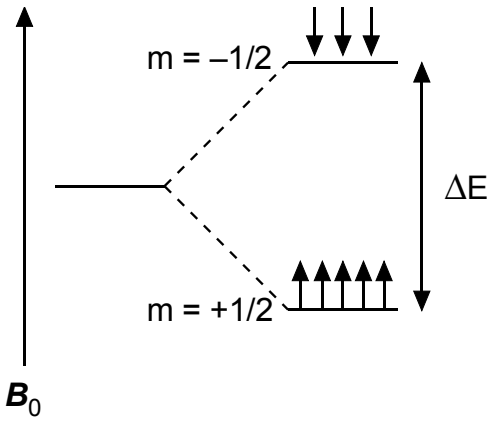


Figure 2.2 Schematic diagram showing the energy levels and the orientation of the spins of an I = $^{1}/_{2}$ nucleus when placed in an external magnetic field $\boldsymbol{B}_0$

Since the spin-up state has slightly lower energy compared to the spin-down, it has a small population excess. This small excess generates the macroscopic magnetization vector ($\boldsymbol{M}_0$), which is aligned in the direction of $\boldsymbol{B}_0$, which is the spin-up state at thermal equilibrium.[2] The population of the states, and therefore net magnetisation, can be

manipulated by applying RF pulses, at the Larmor frequency, along the *x*, *y*, or *z*-axes.[3,4] The duration of the RF pulse, t_p and power, $\boldsymbol{B}_1$, control the degree, or flip angle, θ, of deflection for the net magnetisation, (equation 2.3).[3,4]

$$\theta = \frac{360\gamma}{2\pi}\boldsymbol{B}_1 t_p \qquad 2.3$$

At equilibrium, $\boldsymbol{M}_0$ lies along the direction of $\boldsymbol{B}_0$, which is defined as the *z*-axis. Thus, the application of 90° or 180 ° RF pulses deflects $\boldsymbol{M}_0$ into the *x*-*y* (transverse) plane or onto the *z*-axis, respectively.[3,4] In terms of the population of the state, in the case of a 90° pulse this means equally distributing the spins among the energy levels, while in the case of a 180° pulse it means inverting the spin population. It is important to highlight that the NMR signal is only detectable when $\boldsymbol{M}_0$ lies in the transverse plane[2] where the precessional motion induces an oscillating voltage in the RF coil, leading to the NMR signal, also known as the free induction decay (FID).[4] This signal will decay over time, due to the recovery of the thermal equilibrium. [4,5] The FID is in a time domain. A Fourier transformation is then applied to the FID to determine the frequency domain NMR spectrum.[5]

2.1.1 Chemical shift

The NMR frequency of nuclei is determined by its gyromagnetic ratio and by the strength of $\boldsymbol{B}_0$.[4] However, within different molecules, there is frequently a variation of magnetic field experienced by nuclei, caused by magnetic inhomogeneities generated

by different chemical environments. This results in a chemical shift of the NMR signal[3] and is the foundation of structure elucidation by NMR spectroscopy.[2]

2.1.2 NMR relaxation

NMR relaxation occurs as the system returns to thermal equilibrium after the application of RF radiation.[3,5] Two different relaxation processes can occur, which are defined as spin-lattice relaxation (T_1) and spin-spin relaxation (T_2).[3,4] Local magnetic fields oscillating at the Larmor frequency causes both T_1 and T_2 relaxation.[3,4] However, T_2 relaxation is also affected by non-oscillating local fields.[4] The variation of the local magnetic field is dependent on different factors, such as dipolar coupling and molecular motion.[4,5] Dipolar coupling describes the interaction of the magnetic fields between spins, and it is dependent on the distance $\boldsymbol{r}$ between the two nuclei and on the angle θ of the vector joining the two spins relative to the direction of $\boldsymbol{B}_0$.[3,5] Paramagnetic species possess a strong magnetic moment, caused by unpaired electrons, which enhance the relaxation process caused by dipolar coupling.[5] The angle θ and distance $\boldsymbol{r}$ change in time due to molecular tumbling. This causes a variation of the local magnetic field with time that enhances the relaxation process of the spins.[3,5] Molecular tumbling, is characterised by a rotational correlation time τ_c, which is the average time needed for the root-mean-square deflection of a molecule to tumble by one radiant.[3]

T_1 relaxation is dependent on the probability that local magnetic fields have a component oscillating at the Larmor frequency.[3] At short τ_c, thus at fast tumbling, the frequency generated by the molecular motion will have a high probability to be at higher frequencies compared to the Larmor frequency and they will only slightly affect the T_1.[3,5] Similar effects on the T_1 are observed at slow tumbling (long τ_c), where the

frequencies generated will be lower than the Larmor frequency.[3-5] Instead, when the frequency of the magnetic fluctuations matches the Larmor frequency, the lowest T_1 is achieved.[3,4] Thus, as shown in Figure 2.3, T_1 will be longer at short τ_c, it will decrease and pass through a minimum while the τ_c becomes longer, and then it will increase, reaching again its maximum value at longer τ_c. T_2 instead, is dependent on both fields oscillating at Larmor frequency and non-oscillating fields.[4] Because of the dependence on non-oscillating fields, T_2 will not pass through a minimum as T_1, but it will keep decreasing as τ_c becomes longer.[3]

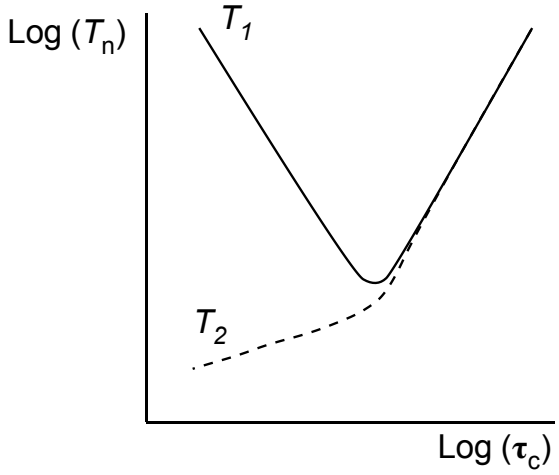


Figure 2.3 Schematic graph showing the T_1 and T_2 relaxation time with the correlation time τ_c

Both T_1 and T_2 relaxation times are used to obtain molecular information on the substances studied. For instance, NMR relaxation time measurement is the main technique used to study the flexibility of proteins and their internal dynamics.[6] This is possible because changes in the global and local motion of the protein, causes a variation of the relaxation times, which can be associated with the protein flexibility.[6]

Changes in T_1 and T_2 relaxation times are also used to study the dynamics of polymers in various environments and their crystallinity. [7] Indeed, an increase in crystallinity causes an increase of dipole-dipole interactions which results in a faster T_2 relaxation time. In porous media instead, relaxation times variations caused by the pore structure are used to evaluate various parameters, such as wettability, fluid distribution, pore size distribution, and permeability.[8,9]

The time taken for the spins to return to thermal equilibrium is defined by T_1 relaxation time. Spin-lattice (T_1) relaxation is frequently determined using an inversion recovery pulse sequence, whose schematic is visible in Figure 2.4.[2-4]

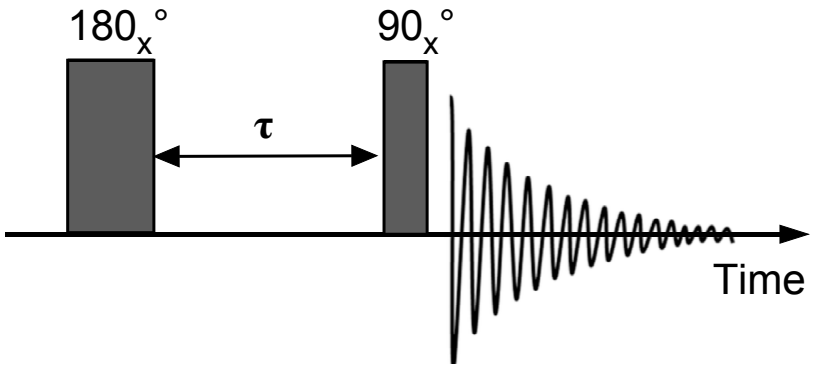


Figure 2.4 Schematic diagram of an inversion recovery pulse sequence.

In this sequence, an initial 180° RF pulse is applied which invert the population of the spins and brings $\boldsymbol{M}_0$ along the – *z*-axis. The system returns to equilibrium during a time τ after the 180° pulse. Finally, a 90° RF pulse is applied, which places $\boldsymbol{M}_0$ in the *x*-*y* plane allowing the FID to be collected. To measure how the magnitude and sign of magnetisation change because of the relaxation process, the pulse sequence is

repeated applying each time a different τ. T_1 relaxation time is then determined by fitting the recorded signal intensity, as a function of τ, to equation 2.4. [3,4]

$$M_z = M_0 \left(1 - 2e^{\frac{-\tau}{T_1}}\right) \quad 2.4$$

T_2 relaxation time is the time required for magnetization in the transverse plane to decay to ~ 37% of its initial value decay, because of spins de-phase and magnetisation decay.[3] When the magnetization is brought in the transverse plane by a 90° RF pulse, the spins are initially phase coherent.[4] However, as described in section 2.1.2, spins experience a range of local magnetic fields from $\boldsymbol{B}_0$ inhomogeneities and intra- or/and intermolecular interactions.[2-5] This causes spins to precess at different frequencies, leading to a loss of coherence and decay of the signal.[4] Both effects give rise to an effective time constant T_2*, described by equation 2.5.[4]

$$\frac{1}{T_2^*} = \frac{1}{T_2} + \frac{1}{T_{2(\Delta B_0)}} \quad 2.5$$

where $T_{2(\Delta \boldsymbol{B}0)}$ considers the effect of the static magnetic field inhomogeneity and T_2 considers the effect of intra- or/and intermolecular interactions. T_2 relaxation time is measured using a spin-echo sequence,[10] shown in Figure 2.5.

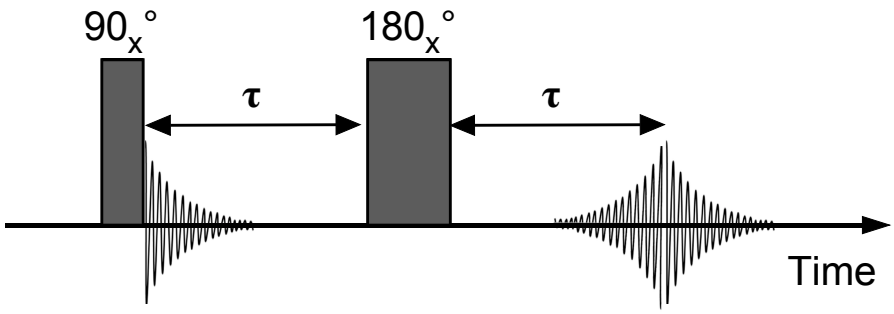


Figure 2.5 Schematic diagram of a spin-echo pulse sequence.

During the sequence, an initial 90° RF pulse is applied which flips the magnetization onto the *x-y* plane. Once on the transverse plane, due to the spins start to de-phase during the first period τ. After this, a 180° RF pulse is applied which inverts the magnetization. During the second τ period, the spins refocus eventually forming a spin echo.[4] However, spins are refocused only if they experience the same magnetic field during the whole spin-echo sequence. Indeed, if the acquisition time the spins diffuse to a position where they experience a different magnetic field, they will not be refocused. Thus, the measured signal is attenuated and the percentage of this attenuation will be exponentially proportional to τ.[11,12] A way to minimize the diffusion effect is using the Carr-Purcell-Meiboom-Gill (CPMG) sequence instead.[4] CPMG sequence (figure 2.6) repeats the τ-180°-τ par of the spin-echo sequence for *n* times, after the application of a single 90° RF pulse, using short τ. In this way, multiple echoes are formed whose decay can be fitted with equation 2.6 allowing the evaluation of T_2.[4]

$$\frac{S(2\tau)}{S(0)} = e^{-\left(\frac{2\tau}{T_2}\right)} \qquad 2.6$$

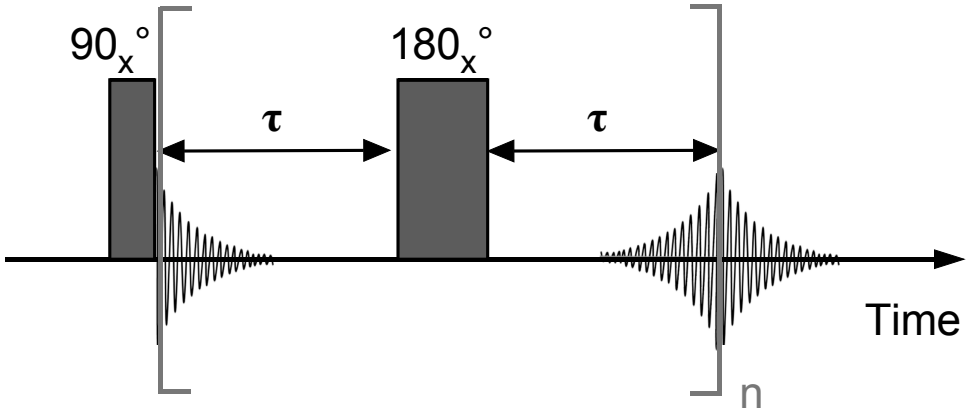


Figure 2.6 Schematic diagram of the CPMG sequence.

2.2 Magnetic resonance imaging

The application of a magnetic gradient to a static magnetic field, causes the precession frequency of the spins to be dependent on their position ***r*** and the gradient strength ***G***.

$$\omega(r) = \gamma \boldsymbol{B_0} + \gamma \boldsymbol{G r} \qquad 2.7$$

This dependency enables to use NMR to obtain spatial information about the sample under investigation. In MRI, images are produced by acquiring ***K***-space data and then applying a Fourier transformation to the data. Since ***K***-space, also known as reciprocal space vector, is dependent on the gradient strength ***G*** and the gradient duration *t* (Equation 2.8), spatial information can be encoded in two way: (i) frequency encoding, when *t* is changed keeping ***G*** constant, and (ii) phase encoding, when ***G*** is varied keeping *t* constant.[13,14]

$$\boldsymbol{k} = \frac{\gamma \boldsymbol{G} t}{2\pi} \qquad 2.8$$

When performing frequency encoding, the gradient is on while the signal is acquired. This makes the spin precession dependent on their position, as described in equation 2.7. Thus, the NMR signal intensity recorded will be dependent on how many spins precess at a precise frequency. In phase encoding the magnetic field, the gradient is applied before the signal is acquired. In this way, the frequency of the spins will remain the same during data acquisition, while their phase will be different depending on the spin position, making the image reconstruction possible. While frequency encoding can be used alone to produce a 1D profile of all the spins projected onto one axis, a combination of frequency and phase encoding is needed to produce 2D and 3D images. Indeed, by applying both frequency and phase encoding, a 2d data set of the in ***k***-space can be produced. A 2D Fourier transformation of this data set produces a real-space 2D profile that is a projection of all the spins onto the third dimension. Important, to produce a 2D image of a plane of the sample, is the slice selection. Slices are selected by applying a soft RF pulse magnetic field gradient perpendicular to the direction of the plane to image, and a soft RF pulse.[15] The RF pulse frequency encodes the spins by only exciting spins with a specific frequency.[13] This is achieved by adjusting the RF duration.[13] In this way, only spins at specific positions are excited, allowing the acquisition of the desired 2D image.

For the acquisition of images, various sequences can be used which are generated by the combination of slice selection, and phase and frequency encoding. One of the most

used is the spin-echo imaging sequence.[14] In the spin-echo sequence, for each data point, a specific magnetic field gradient needs to be used. Thus, for high-resolution images, long experimental times are required.[16]The acquisition time can be reduced by using a Rapid Acquisition with Relaxation Enhancement sequence (RARE).[17] In this sequence, multiple echoes are acquired for every single excitation. The higher the number of echoes used, the shorter the acquisition time is. Images recorded with RARE are dependent on T_2 relaxation time and spin density. The dependency on T_2 relaxation time increases as the rare factor increases. This is related to the fact that as the rare factor is increased, the time between two successive excitations is lengthened, which means the spins have more time to de-phase between the two pulses. This leads to a reduction of the T_2 relaxation time and a formation of T_2 contrast in the image.[14]

2.2.1 MRI Contrast

One of the main advantages of MRI compared to other techniques is the possibility to obtain contrast in different ways, allowing the visualization of specific sample characteristics. Contrast can be generated in four main ways: (i) spin density, (ii) relaxation time, (iii) chemical shift, and (iv) molecular motion (diffusion and flow). [18]

Spin density contrast is achieved by varying the number of excited spins. The more spins are exited, the higher is the signal intensity in a specific pixel.[16] To produce a spin density image, the relaxation time contrast needs to be minimized, which means using a much shorter echo time (T_E) than T_2, and a repetition time (T_R) longer than $5\times T_1$.[16]The variation of the relaxation times within a sample can be used as a contrast, to produce T_1 and/or T_2 weighted images and maps.[14] In this work, only T_2 relaxation time

maps have been acquired. With the acquisition of T_2 relaxation time maps the relaxation time of each pixel is measured.[13] To produce a T_2 relaxation time map, a series of images with different T_E and constant $T_r \geq 5 \times T_1$ are acquired. Long T_r are needed to avoid T_1 contrast in the images. The images acquired are then packed together and the signal intensity decay for each pixel is fitted with equation 2.6. In this way, the relaxation time for each pixel is determined.

In systems with more than one component, the difference in chemical shifts between the component can be used to generate image contrast.[16] In these systems, the spins' frequencies are not only dependent on the position but also on their chemical environment which, as described in section 2.1.1, causes different spins to have different Larmor frequencies. To record a chemical shift image various methods can be applied.[19]In this study, Chemical Shift Selective (CHESS) imaging[20] has been used. This method saturates the unwanted contributions and only excites the desired frequencies so that the signal recorded is generated only by specific spins. The sequence used to perform CHESS is displayed in figure 2.7. A first 90° pulse is applied which flips the spins with undesired frequencies. This is followed by a gradient pulse that de-phases the spins in the transverse plane leading to their saturation. At this point, space selective 90° RF pulse is applied to excite the desired spins. In the end, a spatially selective 180° pulse is applied which refocuses the spins and allows the formation of an echo.

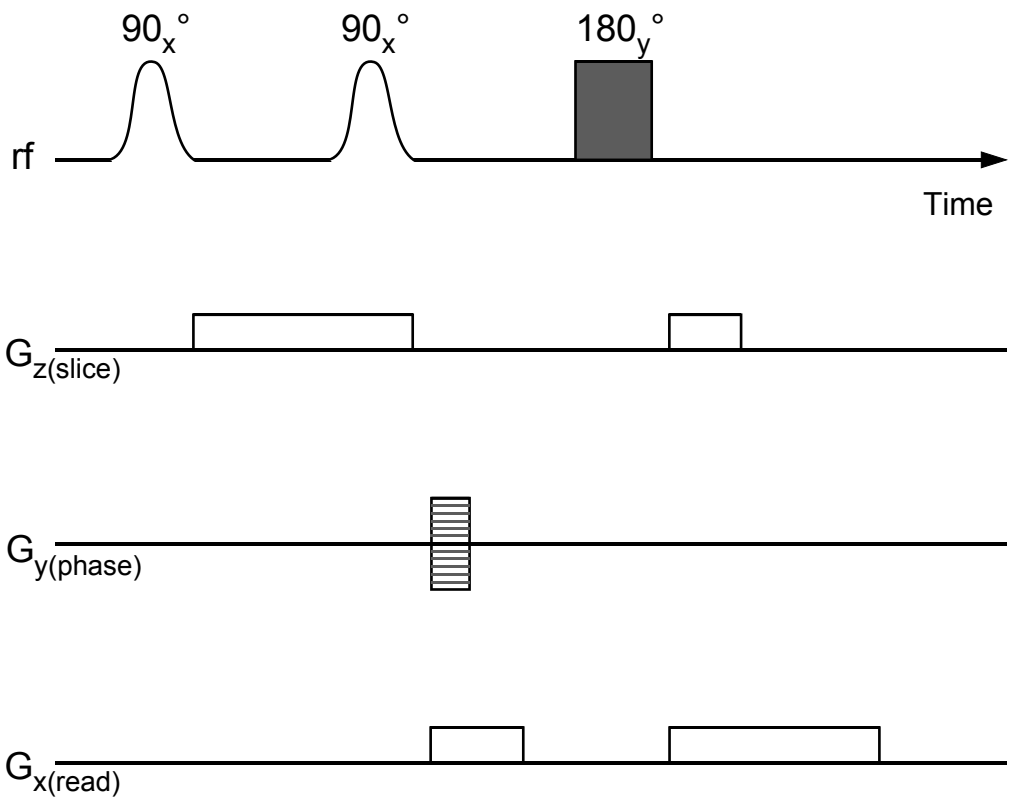


Figure 2.7 Schematic diagram of a CHESS imaging sequence.

2.2.2 Chemical exchange saturation transfer imaging

Chemical exchange saturation transfer (CEST) is an MRI technique that uses the chemical exchange of protons (like the one in the hydroxyl group) of target molecules with water, to indirectly image the former through the water signal.[21-23] To better describe the exchange process and how contrast is generated with CEST, a two-pool system, consisting of a small solute pool, with the solute able to exchange protons, and a larger water (solvent) pool, is generally introduced. In CEST, a frequency-selective RF saturation pulse at the frequency the solute exchangeable protons is applied.[21,22] This frequency-select RF pulse equalize the number of the spin-up and

spin-down protons, generating a not net magnetization, which means there can be no NMR signal. This process is also known as saturation process. This saturation can be transferred from the solute pool to the water pool by a chemical exchange between saturated protons and non-saturated water protons.[21,22] This leads to a reduction of the water signal that is proportional to the solute concentration and the efficiency of the proton exchange process. This process of saturation and exchange between saturated solute protons and non-saturated water protons continues during the whole time the saturation process is applied, amplifying the water signal reduction.

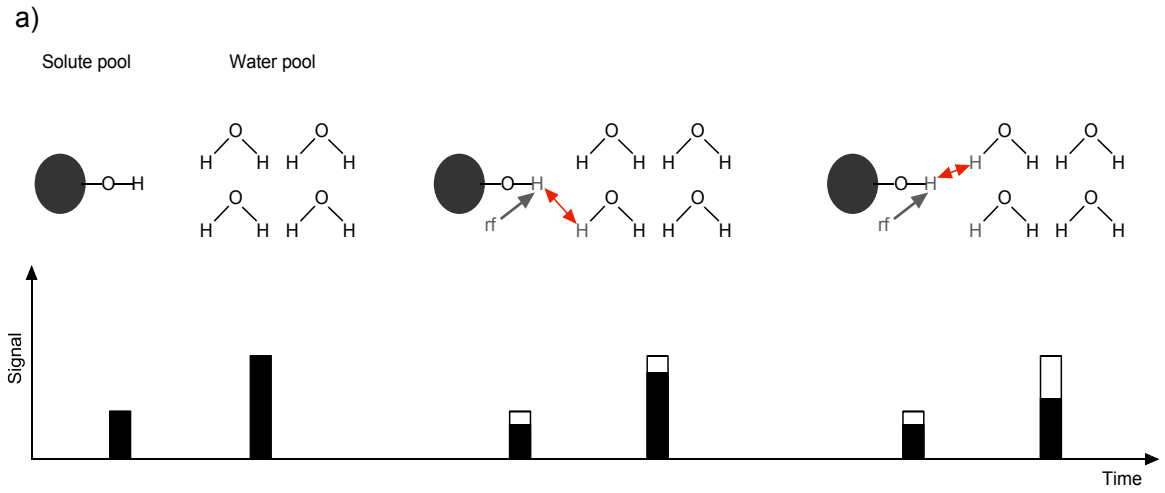


Figure 2.8 Diagram describing the CEST effect. A solute is saturated by an RF pulse, which reduces its signal. The saturated hydrogen is then exchanged with an unsaturated proton of the water, causing a reduction of the water signal. This process continues during the experiment time leading to an amplified decrease in water signal.

Since the exchange of protons occurs only in regions of the sample where the target molecules are, the reduction of the water signal is localized to these regions. This

localized water signal reduction can then be used to generate a contrast that allows the visualization of the solute. However, since frequency-selective RF saturation pulses are generally not perfectly frequency-selective, other processes can occur which cause the reduction of water signal, such as direct saturation of water protons.[21] Direct saturation is caused by the fact that being not perfectly frequency-selective, the RF saturation pulse cantered on solute resonance frequency will have components at the water protons resonance frequency, which cause the saturation of the latter. This generates a reduction of water signal that is not related to chemical exchange. For solid or semisolid-system magnetization transfer (MT) can also occur. Magnetization transfer is similar to the CEST effect. In MT, an exchange of saturated protons occurs between macromolecule and water molecules. However, differently from CEST, MT involves only solid or semi-solid macromolecule and is not dependent on the spectral position of the RF saturation pulse as in CEST. Both direct saturation and magnetisation transfer are dependent on $\boldsymbol{B}_1$. Thus, spatial inhomogeneities can affect DS and MT, causing problems for CEST experiments. To assess these different saturation processes, a z-spectrum is generally produced (figure 2.9).

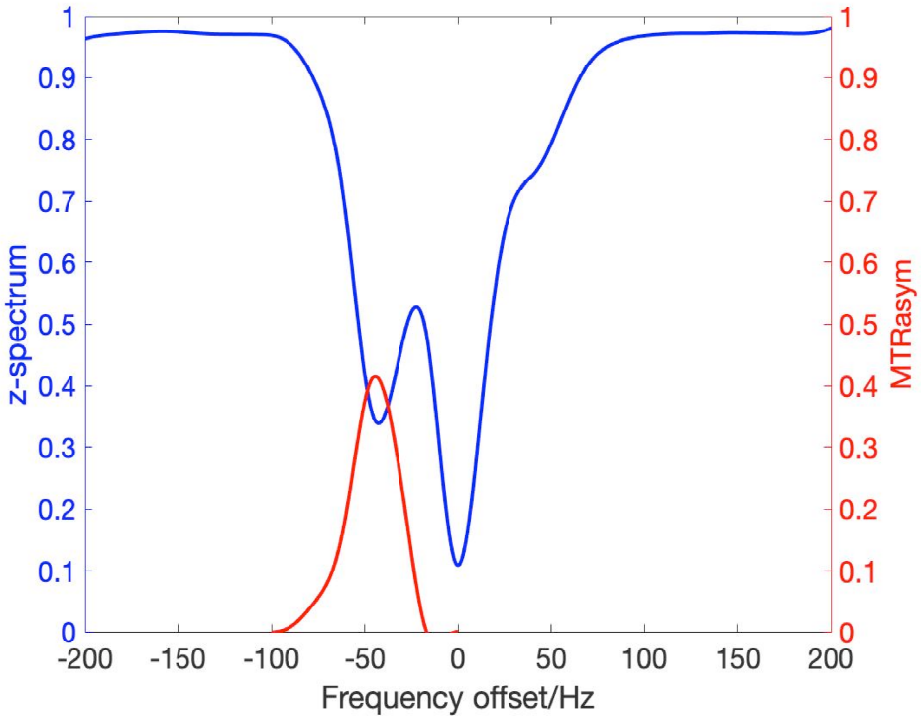


Figure 2.9 example plot of a z-spectrum and MTR_{asym}

In the z-spectrum, the signal of the water is plotted as a function of saturation frequency. In this way, it is possible to visualize eventual water signal reduction caused by chemical exchange saturation transfer, direct saturation and magnetic transfer. Since direct water saturation effects are symmetric with respect to the resonance frequency of the water,[21,24] the CEST effect can be evaluated by subtracting the water signal intensity at a specific chemical shift ($\Delta\omega$) with the water signal at the opposite chemical shift ($-\Delta\omega$), where $\Delta\omega$ is evaluated from the water frequency resonance that is considered at 0 ppm. In this way, the CEST magnetic transfer asymmetric ratio (MTR_{asym}) is derived by :

$$MTR_{asym} = \frac{S(-\Delta\omega) - S(+\Delta\omega)}{S_0} \quad 2.9$$

where S_0 is the water signal in absence of frequency-selective RF saturation pulses. This analysis is also able to remove possible contributions from magnetisation transfer and to correct eventual $\boldsymbol{B}_1$- inhomogeneities. By determining this pixel by pixel, a CEST map can be produced which allows the visualization of the solute or target compound. However, before evaluating the MRT_{asym}, corrections typically need to be performed to the image due to magnetic field ($\boldsymbol{B}_0$) inhomogeneities. $\boldsymbol{B}_0$ inhomogeneities cause a position-dependent shift of each pixel spectrum, meaning that the $\Delta\omega$ can be different for each pixel.[24] To correct this, the z-spectrum for each voxel will be interpolated to find the minimum point. The minimum corresponds to the real water resonance frequency. The frequency of each pixel is then shifted to this point to correct the $\boldsymbol{B}_0$ inhomogeneities.

CEST imaging has several advantages over other MRI imaging techniques (relaxometry or diffusion), such as higher sensitivity, which can be up to 5 times higher compared to other MRI techniques, or the possibility to image only specific compounds. For instance, for biofilms in porous media, T_2-weighted images have difficulties in separating biofilms and water within pores, because the variation of T_2 can be caused both by biofilms and porous media structures. Instead, as described before, CEST effect is frequency-selective. Thus, contrast for a specific compound is only produced when an RF saturation pulse is applied at the resonance frequency of the exchangeable protons of the compound. This means that, depending on the

frequency of RF saturation pulse used, the CEST effect for a specific material can be turned on and off, allowing to identify, with high precision, the presence of the material.

2.3 Complementary techniques

In this work, other techniques complementary to MRI have been used to characterize porous media and visualise biofilm. In particular, μCT has been used to investigate the structure of a polyurethane open-cell foam, while CLSM has been used to visualise biofilm formation within them. As will be described in the next paragraphs, μCT and CLSM enable the possibility to produce a series of information that are not achievable with MRI.

2.3.1 X-ray micro-computed tomography

X-ray tomography is a non-destructive technique that can be used to visualize the 3D internal structure of materials with a micron-scale resolution.[25] Where the spatial resolution is on the order of 50-100 μm, the technique is named X-ray micro-computed tomography or μCT. As the name suggests, μCt is based on the interaction of X-ray photons with the material under study, which is described by the Lambert-Beer equation:[25]

$$I = I_0 e^{-\int \mu(s) ds} \qquad 2.10$$

where I_0 is the intensity of the emitted X-rays before reaching the sample, I is the X-ray intensity after traversing the sample, s in the sample thickness and μ(s) is the X-ray attenuation factor. The value of μ(s) is dependent on the atomic number (Z) and

on the material density (ρ), thus higher X-ray adsorption is achieved for elements with higher atomic numbers.[25,26] To acquire an image, the sample is irradiated with X-rays emitted from an X-ray generator. Meanwhile, the sample is rotated, up to 180° and 360° degrees, at small angle increments. The emitted signal, at each increment, is recorded on a CCD detector, producing 2D projections.[27] These 2D images are then reconstructed to produce a 3D image of the sample.[27] To record the 2D projection, important parameters are the image contrast and spatial resolution. Image contrast, in μCT images, arises through partial and differential X-ray absorption.[27] For the former, part of the irradiated X-rays need to be totally or partially adsorbed. If all or none of the X-rays are adsorbed, no contrast results. The latter arises through differences in X-ray absorption, within the sample, caused by the different chemical nature of the materials composing the sample. If there is no difference in X-ray absorption between the different parts of the sample, there will be a uniform grey level within the image. Spatial resolution is controlled by the X-ray source, the distance between source, sample and detector, and the sample size.[28] Greater resolution is achieved using a micro-focused X-ray beam, reducing the distance between the X-ray source and the sample as well as reducing the sample size.[28] However, when recording an image, the choice of these factors is determined by a combination of the desired field of view and scanning time.

Compared to MRI, which usually has a resolution of 10s-100s of microns, μCT offers a much higher resolution (around 50 μm), which allows the direct visualization of porous media internal structures, providing information such as the dimension and the surface area for every single pore. However, the fact that images are produced using the variation of intensity caused by differences in electron density between the different

part of a sample, and the long experimental times, do not allow the study of the fluid transport within porous media. MRI instead, produces images of porous media indirectly, by imaging the fluid contained with it. The lower resolution does not allow the characterisation of every single pore. However, as described in paragraphs 2.4.2 and 2.4.3, with MRI it is possible to evaluate the pore size distribution of the media, the permeability, and to evaluate flow processes that will be impossible to visualize using μCT.

2.3.2 Confocal laser scanning microscopy

Confocal microscopy is a technique used to visualize high-resolution structures in different fields. The confocal microscope was introduced in 1957, by Marvin Minsky[29], to improve the resolution of the conventional microscopes by reducing the amount of light coming from out of focus planes of the sample. A confocal microscope is composed of a laser source, a scanning mechanism, a light detector with a pinhole placed in front of it, and lenses to direct and focus the light.[30] The pinhole plays an important role in the operation of the microscope. As illustrated in figure 2.10, only the light coming from the focal plane passes through the pinhole, while the light from out of focus plane is blocked by the pinhole walls.[30] Thus, reflected light originated from sections that are not in the focal plane is omitted, yielding to a sharper image compared to the one acquired with a standard microscope. Another advantage of confocal microscopy over conventional microscopy is the possibility of imaging different optical sections (*x-y* planes) through the sample along the axial axes,[31] permitting the acquisition of 3D images by simply recording different sections and reconstructing them using computer software. [31]

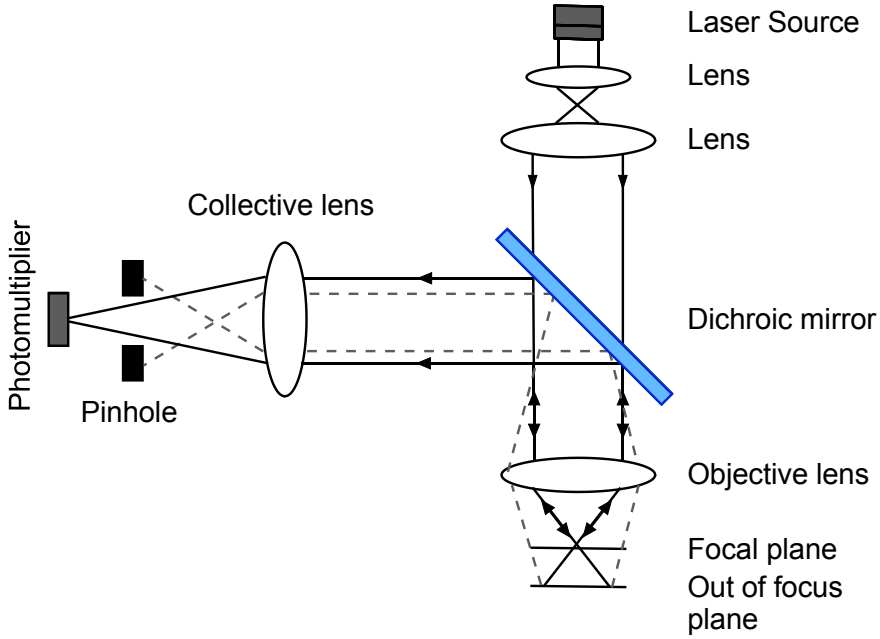


Figure 2.10 Confocal diagram configuration.

The confocal microscope can be used in different modes. The most commonly used, also utilized in this work, is the fluorescent mode. In this mode, the laser is used to selectively excite fluorescent molecules or tags intrinsic, or added, to the sample. Backscattered fluorescence is then used to record the image.[31] Moreover, confocal microscopy also offers the possibility to select the range of wavelength to detect. As a result, dual-channel images can be recorded, where different features within the sample are stained with two different dies, and images of the same focal plane are recorded using two different channels and subsequently overlapped.[31]

2.4 Porous media characterization

All the previous techniques introduced in this chapter have been used, throughout years, to study and characterised porous media and the various processes occurring

within them (flow, biofilm growth, filtration, and so on). Before going into details on how it possible to use these techniques to extract information on porous media, it is important to define what a porous medium is, and which are the parameter used to characterise it.

A porous medium can be defined as a single object, or an ensemble of solids objects, with open spaces within or around them, large enough to let a fluid flow.[32] This definition is quite broad and includes two main concepts of porous media. The first one considers a porous medium as a single continuous object containing holes within it, which can be connected or not, such as a sponge. The second considers a porous medium as a collection of objects packed together in a way that fluid can move between them, like a tube filled with glass spheres. Depending on which concept is used, the medium can be defined respectively as consolidated or unconsolidated.[32] In this work, we will refer to the first concept (consolidate) when using the term porous medium.

2.4.1 Pore structure parameters

A wide range of natural or man-made materials can be defined as porous media. Among these, we can find biological tissues (wood, bones), soil, rocks (e.g. sandstone),[33] ceramics, cement, and polymeric foams.[34] Regardless of their composition, porous media are frequently characterized by three important parameters: porosity, specific surface area, and permeability.[35],[36] Porosity (φ) defines the fraction of bulk volume sample occupied by pores,[35] and its value can change depending on the nature of the porous medium. For instance, open-cell metal

(aluminium, copper) foam or polymeric foam usually have high porosity (> 80%),[37] while in rocks, porosity typically does not exceed 40%. Important, in the definition of the porosity and on the typology of porous media, is the pore classification. Indeed, within porous media, it is possible to encounter three kinds of void spaces: effective/ interconnected, dead-end/blind, and isolated/non-interconnected.[35] As the name suggests, the former are pores connected to other pores and they constitute a continuous phase in the medium.[35] The dead-end pores are connected to other pores only from one side [35] (like a *cul-de-sac* street). The latter instead are completely isolated.[35] If more than half of the pores of a porous media are interconnected porous, the media is defined as open-cell. Conversely, the media is defined as closed-cell. The type of pores plays also an important role in flow within porous media. Indeed, only interconnected pores and dean-end pores contribute to the transfer of fluid within the sample.[35] However, the contribution of the latter is generally so low that can be neglect.[35] To keep into consideration the percentage of pores that actively contribute to fluid flow, the effective porosity has been introduced, where effective porosity is the percentage of pores that actively contribute to fluid transport.[38]

Specific surface area (*S*) is the sum of all the surface areas of the pores within the medium. Its evaluation is fundamental in assessing the efficiency of filters, industrial adsorbents, etc. [35,39] Surface area is also related to the permeability (*k*) of the medium, which is defined as the measure of the flowing ability of fluid through the porous specimen.[36] These three parameters are interconnected with each other and are fundamental to the characterization of the media. Depending on the application of the porous media, other parameters can be used for characterization, like tortuosity (*T*).

Tortuosity is geometrically defined as the shorter path length through a porous structure dived by its thickness.[40] Tortuosity, permeability and porosity are important to the understanding and description of fluid transport in porous media, and related by the Carman-Kozeny equation:[41]

$$k = \frac{\varphi^3}{cT^2S^2} \qquad 2.11$$

with *c* shape factor.

The kinetic of the liquids in porous media however is dependent not only on the porous structure of the media (e.g. porosity, pore size, permeability), but also on the surface energy of the material composing the media, and on the nature of the liquid. These parameters are all included in the Lucas-Washburn equation, which is generally used to describe liquid flow in porous materials: [42]

$$l(t) = \sqrt{\left(\frac{\gamma\, r\, cos\theta}{2\mu}\right) t} \qquad 2.12$$

where *l* is the fluid front distance, *r* the effective porosity, θ the contact angle between the solution and the porous media, γ the surface tension of the fluid, and μ the fluid viscosity. *T* represents the elapsed time. Lucas-Washburn equation shows that the fluid transport and capillary penetration in porous media exhibit a diffusive behaviour. An increase in θ will cause a decrease of the wettability and a reduction of liquid uptake. However, the effect of contact angle has to be considered in conjunction with γ. Indeed, from equation 2.12, a decrease of γ should results in a reduction of wicking.

At the same time, a reduction of the surface tension will also cause a reduction of the contact angle, which, has described above, will cause an increase of liquid uptake. Therefore, the effect of the surface tension and contact angle cannot be considered separately, but the whole $\gamma cos\theta$, known as wettability function, has to be considered.[43] Viscosity also plays an important role. Indeed, an increase in viscosity will lead to a decrease of the sample transport rate.[44]

Lucas-Washburn equation has been extensively used in different area of research, such as contact angle measurements and porous media characterization.[45,46] However, it is important to highlight that equation 2.12 assumes that the media is composed by a bundle of parallel capillary tubes which have the same radius, and that the liquid properties, such as surface tension and dynamic viscosity, are constant.[47] Moreover, it does not take into consideration the influence of gravity.[48] Per contra, in real porous media, the dimensions of the pores is usually not constant, and media are generally tortuous. Because of this, the applicability of Lucas-Washburn equation to real porous medias have been extensively studied and it still is under investigation nowadays.[46]

2.4.2 NMR relaxation time for measuring the pore size distribution

NMR T_1 and T_2 relaxation time measurements have been widely employed to characterise porous media, including determination of pore size distributions of porous media saturated with fluid, such as water.[49,50] This is achieved by the dependence of T_1 and T_2 relaxation times on the size and shape of pores, the water content inside pores, and the type of material constituting the pore matrix.[51-53] When a fluid is

contained in a porous media, the fluid molecules, are displaced at the centre of the pores and absorbed on the surface of the pores.[51] Because of the presence of bulk molecules and adsorbed molecules, the spin-lattice relaxation rate can be given by:

$$\frac{1}{T_1} = \frac{x}{T_{1S}} + \frac{(1-x)}{T_{1B}} \qquad 2.13$$

Where x is the fraction of water molecule adsorbed on the surface, T_{1S} is the surface relaxation rate and T_{1B} is the bulk relaxation time. T_{1s} is generally shorter than T_{1B}, because of dipolar interactions between surface groups and molecules adsorbed on the surface, the presence of paramagnetic species in the matrix solid, and the reduced mobility of adsorbed molecules. If we define the pore volume as *V*, the pore surface area as *S,* and the fluid surface layer thickness as *h*, equation 2.13 can be rearranged as:

$$\frac{1}{T_1} = \frac{1}{T_{1B}} + \frac{Sh}{V}\left(\frac{1}{T_{1S}} - \frac{1}{T_{1B}}\right) \qquad 2.14$$

which is generally written in the following form

$$\frac{1}{T_1} = \frac{1}{T_{1B}} + \rho_1 \frac{S}{V} \qquad 2.15$$

where ρ_1 is defined as the surface relaxivity parameter.

In the case of T_2 relaxation rate, a new term needs to be added to the equation to account for the reduction of the relaxation rate caused by molecule diffusion within internal magnetic field gradient,[52,53] since the porous matrix and water possess different magnetic susceptibilities, χ_{pm} and χ_w. This difference in magnetic susceptibility ($\Delta\chi$) generates, within the pores, an internal magnetic field gradient.[54] Protons diffusing within the pore will experience a different magnetic field depending on their position. This causes an enhanced dephasing of magnetisation which leads to a shorter T_2 relaxation time. Therefore, the relaxation rare for T_2 can be written as:[52]

$$\frac{1}{T_2} = \frac{1}{T_{2B}} + \rho_1 \frac{S}{V} + \frac{1}{T_{2D}} \qquad 2.16$$

From equations 2.15 and 2.16, it is clear how both T_1 and T_2 relaxation rates can be used to evaluate the pore size distribution of porous media. However, T_2 relaxation time measurements are generally performed, since it is possible to measure it with a single experiment using a Carr-Purcell-Meiboom-Gill CMPG sequence.[51] Most of the research performed using relaxation time concerns rocks and macro-porous materials as a result of the high commercial importance these materials play in well logging. For instance, different studies have been conducted on shale rocks to evaluate the pore structure, which is fundamental for oil recovery.[55-57] Few or no studies have being performed on polyurethane foams.

2.4.3 MRI for porous media characterization

MRI is extensively used to study porous media, in particular rocks. The possibility to directly visualize liquids within the media, and to study how the NMR liquid properties

(relaxation time and diffusion) are influenced by the pore structure, make it possible to evaluate permeability, tortuosity, pore size distribution, and surface to volume ratio.[18] However, MRI suffers from a lower resolution, usually 10s-100s of microns, compared to other techniques, which makes it difficult to visualize a single pore. The lower resolution is related to the way MRI works. In MRI, images reproduce the signal intensity for each voxel, where signal intensity is proportional to the number of nuclei within each pixel and is also affected by relaxation times of nuclei.[58] An increase of resolution means that a voxel will contain fewer nuclei, which translates in a lower intensity and an increase of signal to noise ratio (SRN). Similarly, a decrease of T_2 relaxation times lead to lower signal intensity and thus to a higher SRN.[58] T_2 relaxation times play an important role in determining the resolution achievable with MRI to visualize porous media. Indeed, as described in section 2.3.4, the reduced mobility of water within pores,[18] and the difference in magnetic susceptibility between the pore matrix and the water,[54] causes an enhancement of the T_2 relaxation process, which limits the resolution achievable.

Despite the lower resolution compared to other techniques, MRI enabled to study of different processes occurring within porous media that would have been impossible to study with μCT, SEM, or CLSM. For instance, the phase transition from solid to liquid, and its impact on pore size distribution has been observed through T_2 - contrast images in porous media containing water/tetrahydrofuran (THF) solution.[59] Indeed, solid THF hydrates possess a lower signal intensity compared to water/THF solution, which generates a proper contrast between the hydrates and the solution and it allows the visualization of solid hydrates formation over time. T_2 relaxation time and its dependence on paramagnetic species (described in section 2.1.2), such as Cu^{2+}, or

Mn^{2+} can also be used to map the spatial distribution of these species. Moreover, using the RARE sequence, it also possible to evaluate the concentration of the paramagnetic species in porous media.[60] Indeed, in the RARE sequence, a relation exists between the T_2 and the signal intensity. If the relaxivity of the species under investigation is known, its concentration can be evaluated from signal intensity.[61] When relaxation methods are not able to differentiate different chemicals, CHESS or chemical shift imaging (CSI) can be used as an alternative to generating contrast. These image sequences have been employed for the spatial visualization of oil and water in porous media such as sandstones,[62] limestones, [62] or mimic porous media composed of glass beads.[63] For instance, the effect of water and oil saturation on water displacement within carbonated rock media has been observed using CHESS imaging,[62] which is important for petroleum extraction processes. Moreover, CHESS imaging also enabled to resolve oil and water coexisting in a Bentheim sandstone as mixed immiscible phases.[62] The possibility to spatially separate two different fluids or substances within a porous media can potentially be used to study how food and liquid are trapped within a PU open-cell foam, how this affects the formation of biofilms within it, and how detergents penetrate within porous media and remove both food residues and biofilms.

2.4.4 Micro-CT for porous media characterization

X-ray micro-computed tomography is probably the best technique to investigate the three-dimensional internal structure of a porous media, such as open-cell foam, in a non-destructive way. From 3D images produced by μCT measurements, global, and local structural features can be extracted.[64,65] Global structural features include porosity, cell density, and length and thickness of pore struts.[64,65] Local structural

features instead refer to pores position, orientation, shape, sphericity, maximum opening, equivalent diameter, and surface area.[64,65] To evaluate all these features, different processing steps needs to be performed. At first, grey-scale images need to be generated from μCT reconstructed images, which are then denoised by the applications of filters.[65] At this point, the images are segmented by thresholding and labelling, where in the thresholding step each voxel is defined as polymer matrix or void, while in the labelling step the cell's borders are reconstructed and a label number is assigned for each cell.[64,65] Moreover, cells in contact with the borders of the image are generally removed.[65] The images produced after these steps are then analysed to extract all the local and global structure features of the porous medium, such as maximum opening and surface relaxation.[65] Of particular interest, for the studies performed in this thesis, is the maximum opening, which defines the diameter of the biggest sphere that can be fitted within a pore (figure 2.11).

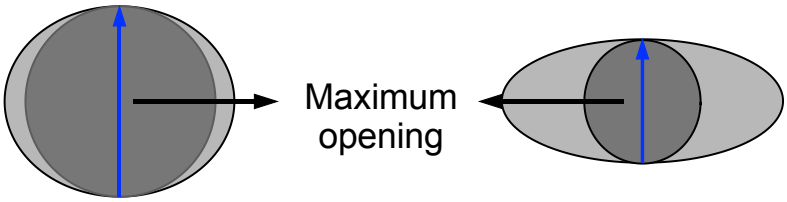


Figure 2.11 Schematic diagram showing two different pores and the spheres (dark grey) used to evaluate the maximum opening (blue arrow).

Micro-CT has been successfully used to characterize both metallic and polymeric open-cell foam. However, while, for metallic foams the high X-ray absorption of the metals lead to high contrast between the pore matrix and air, in polymeric foam, the

weak X-ray absorption of polymers causes low contrast, which can affect the reconstruction of the pores features.[65]

2.5 Flexible polyurethane foams

Flexible polyurethane foams (FPU) are one of the most used polymeric foam in the world and are used in various applications, from filtration to insulation, packaging, and house utensils.[66-70] This wide use is related to their great deformation recovery and elastic properties, and to the possibility of producing them with different structures and densities.[71,72] In particular, polyurethane foams can be defined as open-cell foams or closed-cell foams (Figure 2.12). The formers are characterized by interconnected pores and are mostly used for cushioning, sponges, and sound insulation.[73-75] The latter are instead composed of isolated voids and are more suitable for automotive materials and thermal insulation.[76,77] Polyurethane open-cell foam are characterized by a high porosity (>90%), and large surface area. The range of pore sizes instead, can largely change depending on the application the foam is going to be used for.[78] However, independently of the size, pores are characterized by an irregular polyhedral shape with a number of faces that can vary from 9 to 17.[79] All these factors can influence PU open-cell foam properties, like their flexibility or their ability to retain liquids.

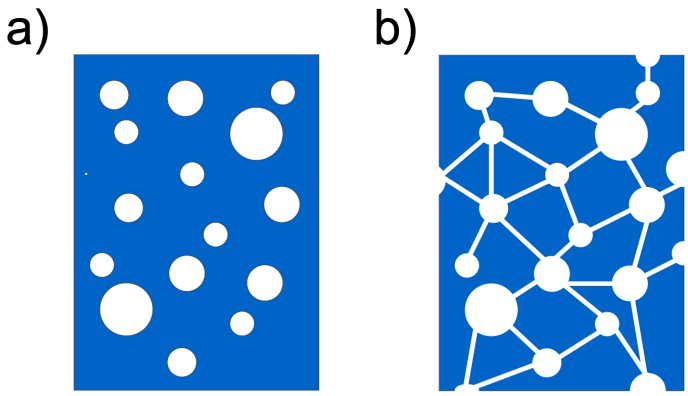


Figure 2.12. A schematic representation of a) a closed-cell foam, and b) an open-cell foam

Porosity, pore size, and pore cell are controlled by the way the foam is produced. The basic ingredients for the formation of FPU are isocyanate, chemicals containing OH groups, such as a polyol, and water.[80,81] These three ingredients react in a two-step reaction called respectively "gel" (Fig. 2.13) and "blow" (Fig 2.14) reaction.[81] During the gel reaction, isocyanate reacts with the polyol OH groups to gel the polymer by creating polyurethane linkage (Fig 2.13). On the second step, isocyanate reacts with water to produce an intermediate product (Fig. 2.14a), carbamic acid, that quickly decomposes forming an amine and releasing CO_2 (Fig 2.14b). This CO_2 then acts as a blowing agent causing the expansion of the polymer melt. Moreover, the amine further reacts with the isocyanate present in the mix, producing urea (Fig 2.14c).[80,81]

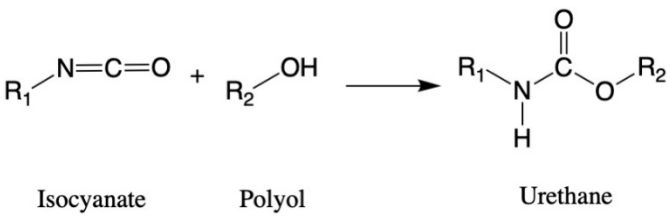


Figure 2.13 Gel reaction

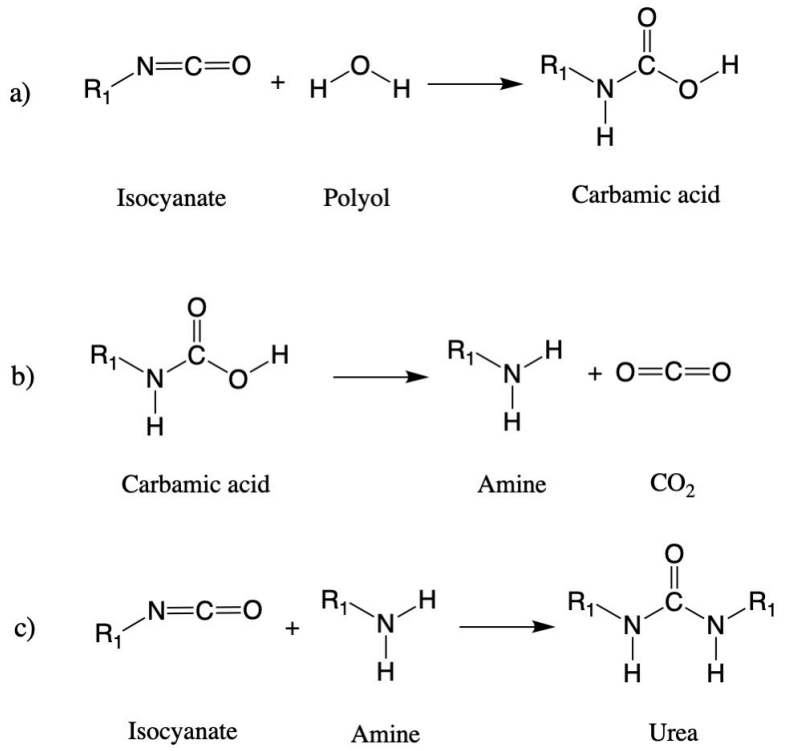


Figure 2.14 Blow reaction: a) first stage; b) decomposition step; c) urea formation

The urea and urethane generated are responsible for the hard part of the foam, while polyols are associated with the flexible segments. Thus, a higher concentration of isocyanate leads to more stiff foams. In the same way, polyols with higher functionality and/or lower molecular weight will generate more rigid foams. *Vice versa*, less isocyanate and/or more water facilitate the formation of more flexible foams.[80-82]

Isocyanate, polyol, and water are the main ingredients for the formation of FPU, but, during the production, other materials are also generally used to control or improve the mechanical or physical properties of the foam. Among these, we find colorants, catalysts, antioxidants, light stabilizers, flame retardants, and surfactants.[83-85] Colorants, light stabilizers, and antioxidants have primarily an aesthetic function. FPF

are generally white. Moreover, they tend to yellowing with time. Colorants, introduced as liquid or paste, give colour to the foam and help to cover the yellowing. In the same way, light stabilizers protect the foam from light, reducing the yellowing effect over time.[81] Antioxidants, instead, protect the foam from the high temperatures of the foaming process. Indeed, the reaction of water with isocyanate is exothermic. During this reaction, temperatures can reach 170 °C causing discoloration. Antioxidants help to prevent this from happening. [81,83]

Surfactants are important in determining the final structure of the FPF. In the foaming process, they have three main roles: (i) to decrease the surface tension in the starting mix, which helps the bubbles to form at the low energies available within the system, (ii) to help the emulsification of the different components in the liquid, which is important to have a good homogeneity within the final foam, (iii) to stabilize the cell structure.[81,85]

Catalysts help in controlling and accelerating the foam rise. This is important because long rise time can lead to the shrinking and collapse of the cell, which will then results in a poor cell structure of the final foam.[81,84]

2.6 References

1 Blumich, B. *NMR imaging of materials*. Vol. 57 (OUP Oxford, 2000).
2 Levitt, M. H. *Spin dynamics : basics of nuclear magnetic resonance*. 2nd edn, (John Wiley & Sons, 2008).
3 Hore, P. J. *Nuclear magnetic resonance*. (Oxford University Press, USA, 2015).
4 Claridge, T. D. W. *High-resolution NMR techniques in organic chemistry*. 1st edn, (Pergamon, 1999).
5 Keeler, J. *Understanding NMR spectroscopy*. (John Wiley & Sons, 2011).
6 Egelman, E. H. *Comprehensive biophysics*. (Elsevier, 2012).
7 Jonas, J. High Pressure Studies Using NMR Spectroscopy. (1999).
8 Al-Mahrooqi, S., Grattoni, C., Muggeridge, A., Zimmerman, R. W. & Jing, X. Pore-scale modelling of NMR relaxation for the characterization of wettability. *J. Petrol. Sci. Eng.* **52**, 172 (2006).
9 Lewis, R. *et al.* in *SPE Unconventional Resources Conference-USA*. (Society of Petroleum Engineers).
10 Hahn, E. L. Spin echoes. *Phys. Rev.* **80**, 580 (1950).
11 Carr, H. Y. & Purcell, E. M. Effects of diffusion on free precession in nuclear magnetic resonance experiments. *Phys. Rev.* **94**, 630 (1954).
12 Meiboom, S. & Gill, D. Modified spin-echo method for measuring nuclear relaxation times. *Rev. Sci. Instrum.* **29**, 688 (1958).
13 Britton, M. M. Magnetic resonance imaging of chemistry. *Chem. Soc. Rev.* **39**, 4036 (2010).
14 Callaghan, P. T. *Principles of nuclear magnetic resonance microscopy*. (Oxford University Press on Demand, 1993).
15 Edelstein, W. A., Hutchison, J. M., Johnson, G. & Redpath, T. Spin warp NMR imaging and applications to human whole-body imaging. *Phys. Med. Biol.* **25**, 751 (1980).
16 Freeman, R. *Magnetic resonance in chemistry and medicine*. (Oxford University Press on Demand, 2003).
17 Hennig, J., Nauerth, A. & Friedburg, H. RARE imaging: a fast imaging method for clinical MR. *Magn. Reson. Med.* **3**, 823 (1986).
18 Britton, M. M. Porous Media Studied by MRI. *eMagRes*, doi:10.1002/9780470034590.emrstm1263 (2011).
19 Joseph, P. M. & Shetty, A. A comparison of selective saturation and selective echo chemical shift imaging techniques. *Magn. Reson. Imaging* **6**, 421 (1988).
20 Haase, A., Frahm, J., Hanicke, W. & Matthaei, D. 1H NMR chemical shift selective (CHESS) imaging. *Phys. Med. Biol.* **30**, 341 (1985).
21 Kogan, F., Hariharan, H. & Reddy, R. Chemical exchange saturation transfer (CEST) imaging: description of technique and potential clinical applications. *Curr. Radiol. Rep.* **1**, 102 (2013).
22 McMahon, M. T., Gilad, A. A., Bulte, J. W. & Van Zijl, P. C. *Chemical Exchange Saturation Transfer Imaging: Advances and Applications*. Vol. 1 (CRC Press, 2017).
23 Vitaliy, K., van der Kemp Wybe, J., Hoogduin, H., WJ, K. D. & Prompers, J. J. Analysis of chemical exchange saturation transfer contributions from brain

metabolites to the Z-spectra at various field strengths and pH. *Scientific Reports (Nature Publisher Group)* **9** (2019).
24 Wu, B. *et al.* An overview of CEST MRI for non-MR physicists. *EJNMMI physics* **3**, 19 (2016).
25 Cnudde, V. & Boone, M. N. High-resolution X-ray computed tomography in geosciences: A review of the current technology and applications. *Earth-Sci. Re.* **123**, 1 (2013).
26 Duane, W., Fricke, H. & Stenström, W. The Absorption of X-Rays by Chemical Elements of High Atomic Numbers. *Proc. Natl. Acad. Sci. U.S.A.* **6**, 607 (1920).
27 Kachelrieß, M. in *Molecular Imaging I* 23 (Springer, 2008).
28 Landis, E. N. & Keane, D. T. X-ray microtomography. *Mater. Charact.* **61**, 1305 (2010).
29 Minsky, M. Patent US3013467A. *Microscopy Apparatus* (1957).
30 Cho, H. *Optomechatronics: Fusion of optical and mechatronic engineering*. (CRC press, 2005).
31 Rossetti, F. b. C., Depieri, L. v. V. & Bentley, M. Confocal laser scanning microscopy as a tool for the investigation of skin drug delivery systems and diagnosis of skin disorders. *Confocal Laser Microscopy-Principles and Applications in Medicine, Biology, and the Food Sciences* (2013).
32 Shamey, R. & Zhao, X. *Modelling, simulation and control of the dyeing process*. (Elsevier, 2014).
33 Haberlandt, R. Transport processes in porous media: diffusion in zeolites. *Thin Solid Films* **330**, 34 (1998).
34 Ganji, D. D. & Kachapi, S. H. H. *Application of nonlinear systems in nanomechanics and nanofluids: analytical methods and applications*. (William Andrew, 2015).
35 Dullien, F. A. *Porous media: fluid transport and pore structure*. (Academic press, 2012).
36 Muir, C. E. & Balcom, B. J. in *Annual reports on NMR spectroscopy* Vol. 77 81 (Elsevier, 2012).
37 Alhusseny, A. N. M., Nasser, A. & Al-zurfi, N. M. *High-porosity metal foams: potentials, applications, and formulations*. (IntechOpen, 2018).
38 Koponen, A., Kataja, M. & Timonen, J. Permeability and effective porosity of porous media. *Phys. Rev. E* **56**, 3319 (1997).
39 Song, K.-H. & Young, J. C. Media design factors for fixed-bed filters. *J. Water Pollut. Control Fed.*, 115 (1986).
40 Tjaden, B., Finegan, D. P., Lane, J., Brett, D. J. & Shearing, P. R. Contradictory concepts in tortuosity determination in porous media in electrochemical devices. *Chem. Eng. Sci.* **166**, 235 (2017).
41 Graczyk, K. M. & Matyka, M. Predicting porosity, permeability, and tortuosity of porous media from images by deep learning. *Sci. Rep.* **10**, 1 (2020).
42 Merkoci, A. *Paper Based Sensors*. (Elsevier, 2020).
43 Delkumburewatte, G. in *Advances in knitting Technology* 287 (Elsevier, 2011).
44 Fu, E. & Downs, C. Progress in the development and integration of fluid flow control tools in paper microfluidics. *Lab on a Chip* **17**, 614 (2017).

45 O'Loughlin, M., Wilk, K., Priest, C., Ralston, J. & Popescu, M. Capillary rise dynamics of aqueous glycerol solutions in glass capillaries: A critical examination of the Washburn equation. *J. Colloid Interface Sci.* **411**, 257 (2013).
46 Xue, H., Fang, Z., Yang, Y., Huang, J. & Zhou, L. Contact angle determined by spontaneous dynamic capillary rises with hydrostatic effects: Experiment and theory. *Chem. Phys. Lett.* **432**, 326 (2006).
47 Cummins, B. M., Chinthapatla, R., Ligler, F. S. & Walker, G. M. Time-dependent model for fluid flow in porous materials with multiple pore sizes. *Anal. Chem.* **89**, 4377 (2017).
48 Hu, Y. *et al.* Mechanisms of fracturing fluid spontaneous imbibition behavior in shale reservoir: A review. *Journal of Natural Gas Science and Engineering*, 103498 (2020).
49 Gallegos, D. P., Munn, K., Smith, D. M. & Stermer, D. L. A NMR technique for the analysis of pore structure: application to materials with well-defined pore structure. *J. Colloid Interface Sci.* **119**, 127 (1987).
50 Hodgkins, M. & Howard, J. Application of NMR logging to reservoir characterization of low-resistivity sands in the Gulf of Mexico. *Aapg Bulletin* **83**, 114 (1999).
51 Barrie, P. J. Characterization of porous media using NMR methods. (2000).
52 Stingaciu, L. *et al.* Determination of pore size distribution and hydraulic properties using nuclear magnetic resonance relaxometry: A comparative study of laboratory methods. *Water Resour. Res.* **46** (2010).
53 Zhang, G. Q., Hirasaki, G. J. & House, W. V. in *SPWLA 41st Annual Logging Symposium.* (Society of Petrophysicists and Well-Log Analysts).
54 Hürlimann, M. D. Effective gradients in porous media due to susceptibility differences. *J. Magn. Reson.* **131**, 232 (1998).
55 Zhao, P., Wang, Z., Sun, Z., Cai, J. & Wang, L. Investigation on the pore structure and multifractal characteristics of tight oil reservoirs using NMR measurements: Permian Lucaogou Formation in Jimusaer Sag, Junggar Basin. *Mar. Pet. Geol.* **86**, 1067 (2017).
56 Zhang, S. *et al.* Integrated NMR and FE-SEM methods for pore structure characterization of Shahejie shale from the Dongying Depression, Bohai Bay Basin. *Mar. Pet. Geol.* **100**, 85 (2019).
57 Pires, L. O., Winter, A. & Trevisan, O. V. Dolomite cores evaluated by NMR. *J. Petrol. Sci. Eng.* **176**, 1187 (2019).
58 Carmi, E., Liu, S., Alon, N., Fiat, A. & Fiat, D. Resolution enhancement in MRI. *Magn. Reson. Imaging* **24**, 133 (2006).
59 Liu, Y., Song, Y., Chen, Y., Yao, L. & Li, Q. The detection of tetrahydrofuran hydrate formation and saturation using magnetic resonance imaging technique. *J. Nat. Gas Chem.* **19**, 224 (2010).
60 Graf von der Schulenburg, D. *et al.* Spatially resolved quantification of metal ion concentration in a biofilm-mediated ion exchanger. *Biotechnol. Bioeng.* **99**, 821 (2008).
61 Britton, M. M. Spatial quantification of Mn2+ and Mn3+ concentrations in the Mn-catalyzed 1, 4-cyclohexanedione/acid/bromate reaction using magnetic resonance imaging. *J. Phys. Chem. A* **110**, 2579 (2006).

62 Chang, C. & Edwards, C. Proton MR two-component chemical shift imaging of fluids in porous media. *The Log Analyst* **34** (1993).
63 Okamoto, I., Hirai, S. & Ogawa, K. MRI velocity measurements of water flow in porous media containing a stagnant immiscible liquid. *Meas. Sci. Technol.* **12**, 1465 (2001).
64 Michaeli, W., Schrickte, L. & Berdel, K. in *Proceedings of the Skyscan User Meeting 2009.* 51.
65 Nacucchi, M., De Pascalis, F., Scatto, M., Capodieci, L. & Albertoni, R. in *AIP Conf. Proc.* 020009 (AIP Publishing LLC).
66 Hnatow, M. F., Bonaddio, V. A., Chan, C. Y., Tursi, D. V. & Rucker, J. R. (Us Patents 6508362B2, 2003).
67 Shastry, A. *et al.* In-Situ High Resolution Dynamic X-ray Microtomographic Imaging of Olive Oil Removal in Kitchen Sponges by Squeezing and Rinsing. *Materials* **11**, 1482 (2018).
68 Starry, G. L. Sponge cleaning device. US patent 3,345,669 (1967).
69 Kumaran, M. & Bomberg, M. Thermal performance of sprayed polyurethane foam insulation with alternative blowing agents. *J. Therm. Insul.* **14**, 43 (1990).
70 Ma, Q., Cheng, H., Fane, A. G., Wang, R. & Zhang, H. Recent development of advanced materials with special wettability for selective oil/water separation. *Small* **12**, 2186 (2016).
71 Gong, L., Kyriakides, S. & Jang, W.-Y. Compressive response of open-cell foams. Part I: Morphology and elastic properties. *Int. J. Solids Struct.* **42**, 1355 (2005).
72 Lei, Y., Zhou, S., Zou, H. & Liang, M. Effect of crosslinking density on resilient performance of low-resilience flexible polyurethane foams. *Polym. Eng. Sci.* **55**, 308 (2015).
73 Jahani, D. *et al.* Open-cell cavity-integrated injection-molded acoustic polypropylene foams. *Mater. Des.* **53**, 20 (2014).
74 Krueger, J. J. *et al.* (US Patent 7,358,282, 2008).
75 Sims, G. & Bennett, J. Cushioning performance of flexible polyurethane foams. *Polym. Eng. Sci.* **38**, 134 (1998).
76 Roberts, R. D. & Kwok, J. C. Styrene–maleic anhydride copolymer foam for heat resistant packaging. *J. Cell. Plast.* **43**, 135 (2007).
77 Subramonian, S., Filiccia, P. & Alcott, J. Novel soft touch, low abrasion, fine cell polyolefin foams. *J. Cell. Plast.* **43**, 331 (2007).
78 Landers, R., Modro, H. & Hubel, R. in *Proceedings of the 2014 Polyurethane Technical Conference, Dallas, TX, USA.* 22.
79 Jang, W.-Y., Kraynik, A. M. & Kyriakides, S. On the microstructure of open-cell foams and its effect on elastic properties. *International Journal of Solids and Structures* **45**, 1845 (2008).
80 Gama, N. V., Ferreira, A. & Barros-Timmons, A. Polyurethane foams: past, present, and future. *Materials* **11**, 1841 (2018).
81 Eaves, D. Handbook of polymer foams. *polimeri* **25**, 1 (2004).
82 Ashida, K. *Polyurethane and related foams: chemistry and technology*. (CRC press, 2006).
83 Gray, R. L., Lee, R. E. & Sanders, B. M. Low volatility antioxidants for scorch protection of polyurethane foams. *J. Vinyl Addit. Technol.* **2**, 265 (1996).

84 Dworakowska, S., Bogdał, D., Zaccheria, F. & Ravasio, N. The role of catalysis in the synthesis of polyurethane foams based on renewable raw materials. *Catal. Today* **223**, 148 (2014).

85 Zhang, X., Macosko, C., Davis, H., Nikolov, A. & Wasan, D. Role of silicone surfactant in flexible polyurethane foam. *J. Colloid Interface Sci.* **215**, 270 (1999).

3 POLYURETHANE OPEN-CELL SPONGES CHARACTERIZATION

3.1. Introduction

Open-cell foams are porous media, with high permeability and high surface-to-volume ratios and are typically produced from a range of polymers, such as polyurethane, polystyrene[1] and polyethylene[2]. Polyurethane (PU) foams are widely used in cleaning[3], filtration[4] and thermal insulation[5]. More recently, polyurethane foams have found applications in medical procedures, such as wound dressing[6], where they have been shown to reduce the risk of nosocomial infection and stimulate soft tissue regrowth[7]. This broad range of applications relies on the properties of these foams, such as high tensile strength[8], high liquid retention[9] and antimicrobial action[10]. Another important property of the PU foams is their compressibility, and their ability to recover from compression, which is linked to their capacity to absorb fluids and energy[11].

A limitation observed in applications of polyurethane foams is that they can exhibit inconsistent behaviour, even between samples from the same production batch, which is associated with variations in structural properties across the foam caused during the production process. Open-cell flexible polyurethane foams are produced by mixing polyol and diisocyanate[12]. Water is added to the mixture to cause the expansion of the foam by the formation of gaseous CO_2, which results from a reaction between water and isocyanate[12,13]. Surfactants are often added to promote the nucleation of bubbles and pore cell stabilization, which are essential for the control of pore size and permeability within the foam[14]. During expansion, CO_2 gas distributes unevenly within

the growing bubbles, causing anisotropic expansion of cells [15], especially along the axis of expansion. This exothermic reaction leads to variability in pore size, even between sponges produced from the same batch, which results in inconsistent behaviour in these types of foams. Thus, in order to test the performance of PU foams, for a range of applications, it is important to be able to characterise their pore network and relate this to their structure, behaviour and compressibility.

The structure and properties of porous media have been studied extensively using a wide range of techniques, including mercury intrusion porosimetry (MIP)[16], scanning electron microscopy (SEM)[17], X-ray micro computed tomography (μCT)[18], nuclear magnetic resonance and magnetic resonance imaging (MRI)[19]. While MIP and SEM are widely used for studying rocks and other solid scaffolds, they have drawbacks when studying flexible or polymeric porous media, such as sponges. In the case of MIP, which is based on the intrusion of mercury within the porous medium[20], it requires the application of external pressures, up to 10^8 Pa. The application of such of high-pressures can cause sample deformation and compression[21], which leads to inaccuracies in measurements. As a result, MIP is not suitable for flexible foams with porosities higher[20] than 90%. In the case of SEM, it has excellent spatial resolution ($50 \times 10^{-9} – 100 \times 10^{-9}$ m)[22], and has been widely used to analyse the morphological properties of PU foams[23-25]. However, samples of PU foams need to be sectioned, which is invasive and can cause edge effects and errors in the measurements[20].

Magnetic resonance (MR) and X-ray μCT are both non-invasive techniques which offer complementary information about the structure and properties of porous media. X-ray

μCT is capable of visualizing internal structures within porous objects[18], resulting in 3D images. Image contrast is based on differences in X-ray attenuation coefficient, which depends on both the chemical composition and density of constituent materials. In single-material objects, such as the foams investigated here, the 3D volume can be considered as a distribution of localised density. Within certain boundaries, the spatial resolution is largely limited by the discretization of the 3D volume, hence it is restricted by the sample size. Selecting the appropriate resolution for imaging a porous object is a compromise between the pore size and representative element volume for the specific object of interest[26]. From 3D images, it is possible to extract quantitative parameters including density, porosity and pore size[27-29]. Recent developments in X-ray μCT have also allowed to evaluate flow processes in porous media filled with water and oil[30,31]. One of the major challenges for studying flow processes in porous media such as sponge consisting of polyurethane foam is related to the small difference in contrast between fluids and the low-density porous substrates and, hence, there is a need for contrast agents to be added to the fluid[31].

MRI typically has lower spatial resolution than X-ray μCT, usually on the order of 10^{-5} – 10^{-2} m, and probes the 3D structure of a porous medium indirectly, through detection of the signal of fluid contained within[32-35]. MRI is able to image the fluid within porous media without the need for additional contrast agents[36]. Moreover, the measurement of NMR relaxation times and diffusion coefficients, for fluid within a porous medium, has been employed to provide information on the structure of the pore network, including pore size distribution and porosity and permeability[33-36]. In particular, T_2 NMR relaxation times are influenced by surface relaxation, especially in the presence of

paramagnetic ions on the surface of the pore matrix, reduced mobility, when molecules temporarily adsorb on to the pore surface[37], and internal magnetic field inhomogeneities ($\boldsymbol{B}_i$) produced by magnetic susceptibility differences ($\Delta\chi$) between the solid matrix and fluid[38]. In each of these situations, the T_2 relaxation time of fluid within a pore is reduced, compared to bulk fluid, and is sensitive to the size of the pore. Hence, for a given porous medium, it is generally found that the smaller the pore, the shorter the T_2 relaxation time. Thus, by knowing the relationship between T_2 relaxation time and pore size, it is possible to determine the distribution of pore sizes within a porous medium[39]. In the case of rocks, it is found that the presence of a variety of paramagnetic ions, and the large difference in magnetic susceptibility between matrix and fluids, leads to a strong correlation between pore size and T_2 relaxation time, which has been extensively studied[40-42]. However, while flow MRI has been used to characterise the pore structure of PU foams[43], no MRI studies using T_2 relaxation times have been undertaken to characterise polymeric porous systems. This is because, in contrast to rocks, polymeric porous systems, such as polyurethane foam, do not contain paramagnetic ions and the difference in magnetic susceptibility, between the porous matrix and the fluid within, is low.

In this study, high-resolution X-ray μCT of dry foam samples and ^{1}H T_2 NMR relaxation time of water-filled foam samples, were acquired to characterize the structure of open-cell polyurethane foams. These experiments were performed on both uncompressed and 60% compressed samples. Pore size distributions were evaluated, for uncompressed and compressed sponge samples, by X-ray μCT and compared with T_2 NMR relaxation times of water in the same foam samples, acquired using both MR

images and bulk measurements. The relationship between maximum opening, for pores within each foam sample, with ^1H T_2 NMR relaxation times, for water within the pores, was investigated.

3.2. Materials and Methods

3.2.1. Sample preparation

X-ray µCT and magnetic resonance experiments were conducted on plugs extracted from polyurethane sponges (Spontex, Colombes, France, Batch n° = 7124813). The cylindrical plugs, of diameter 15 mm and height 40 mm, were extracted from three sponges using a 15 mm cork borer (Fisher scientific UK Ltd, Loughborough, UK). Each plug was placed into a 10 ml Terumo® syringe (Terumo®, Binan, Philippines), to position the sponges in the MRI and CT instruments, as well as control their compression. A plastic disk of 15 mm was also placed in the syringe, at the top of the sponge, as visible on figure 1, to enable homogeneous compression. Each plug was reproducibly compressed by adjusting the plunger, in the syringe, to a fixed position, resulting in 60 % compression. Care was taken to ensure no tilting of the plastic disk during compression, leading to non-uniform compression across the plug. For the magnetic resonance measurements, plugs were saturated with 7° dH water, which has been prepared by dissolving in 1 L of deionized water 0.099 g of $CaCl_2$, 0.033 g of $MgCl_2$, and 0.095 g of $NaHCO_3$. Air bubbles were removed by submerging the plugs under water and placing them under vacuum for one hour. Only data from the PU form (blue part of the sponge) were considered and the scourer pad (white part of the sponge) was not considered.

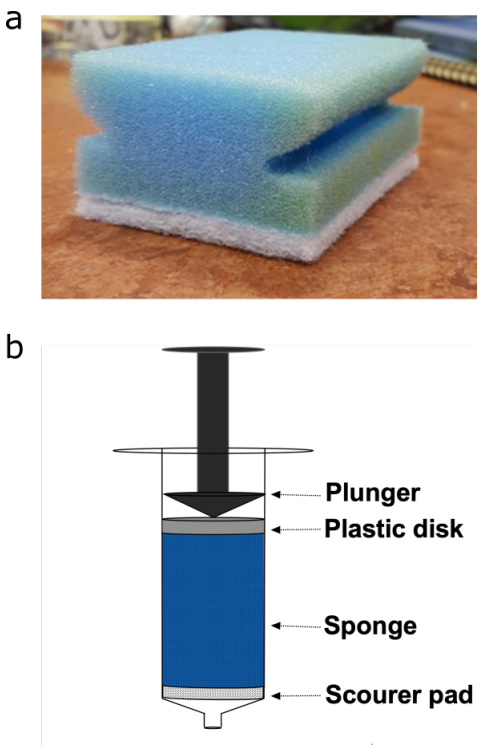


Figure 3.1 a) Photograph of polyurethane sponge. b) Schematic diagram for the set-up used to hold and compress sponge plugs.

3.2.2. X-ray micro-computed tomography

Data were acquired on the High-Energy CT System Optimized for Research (HECTOR)[44] at the Centre for X-ray Tomography (UGCT) at Ghent University, Belgium. This system consists of an XWT240 X-ray tube (X-ray WorkX, Garbsen, Germany) and a PerkinElmer flat-panel detector. For each scan, 2401 projections, of 1 s exposure time per projection, were acquired over the full 360° rotation. The tube was set at a voltage of 70 kV and a target power of 20 W, with 0.5 mm Al filter on the X-ray source to reduce beam hardening effects. Reconstruction of radiographs was conducted using Octopus reconstruction[45]. The reconstructed data has a voxel size of $40 \times 40 \times 40$ μm^3. Octopus Analysis[29] was used to evaluate the morphology of each

plug. The volume of the sponge plug was segmented by grey-value thresholding to obtain quantitative information. Maximum opening was used as an indirect measure of the size pores. The distributions were normalized for the number of pores in each plug. The 3D rendering of the plugs was made using VGStudio MAX 3.2 (Volume Graphics GmbH, Heidelberg, Germany).

3.2.3. Magnetic resonance

Magnetic resonance data were collected on a Bruker Avance III HD spectrometer, equipped with a 7 T vertical wide-bore superconducting magnet, operating at a proton resonance frequency of 300.13 MHz. All experiments were recorded using a micro2.5 imaging probe at 293 ± 0.3 K, which was maintained by the temperature of water-cooled gradient coils. ^{1}H MR images were collected using a 25 mm quadrature ^{1}H radio frequency (RF) WB40 birdcage coil. Bulk T_2 MR relaxation measurements were collected using a 25 mm ^{1}H/^{19}F radio frequency (RF) WB40 birdcage coil. Sagittal (vertical) two-dimensional (2D) T_2 MR relaxation images of water within the plugs were acquired using the spin echo imaging sequence RARE (Rapid Acquisition with Relaxation Enhancement)[46]. Images were recorded using 1 mm slice thickness and a 64 × 128 pixel matrix, with a field of view of 25 × 50 mm. T_2 MR relaxation maps were produced from eight echo images, with a RARE factor of 128, echo time of 8 ms and repetition time of 15 s. A Carr-Purcell-Meiboom-Gill (CPMG) pulse sequence was employed for bulk T_2 measurements, collecting 64 spectra, varying the number of echoes from 0 to 2048, logarithmically spaced, with an echo time of 2 ms and repetition time of 15 s and a spectral width of 100,000 Hz.

All MR data were analysed using the software package *Prospa*[47]*.* A correction was required for the MR T_2 relaxation maps, to compensate for the effects of diffusion, which were found to be sensitive to both the RARE factor and T_2 relaxation time of the liquid.[48] Details of the calibration used can be found in section 2.4. Averaged T_2 relaxation times were determined from bulk CPMG data by fitting to a single exponential, or where a single exponential would not fit the data, a double exponential. The data were fitted to a minimum number of T_2 time constants. T_2 relaxation time distributions ($G(T_2)$ vs $\log(T_2)$) were determined from the CPMG data using a 1D non-negative least square algorithm (NNLS 1D) [49], where $G(T_2)$ is the distribution function with respect to T_2. A regulation parameter, α, was used to assess the smoothness of $G(T_2)$[49]. The ideal value of α was estimated by calculating χ^2, with α fit error as a function of α. The lowest value of χ^2 was chosen before a rapid increase of χ^2, which resulted in the narrowest distributions, without introducing spurious peaks from fitting to the noise[50].

3.2.4. MR T_2 relaxation time maps correction

T_2 relaxation times for a sample, recorded using RARE imaging sequence, are generally affected by signal attenuation arising from the self-diffusion of water, duration the application of the read gradient ($\boldsymbol{g}_R$). Thus, the observed T_2 relaxation time contains a diffusion weighted component, which needs to be corrected. In order to evaluate the correction factor for each sample, four $CuSO_4$ solutions (0 M, 1 M, 2 M, 5 M) were prepared in 7° dH water. Each solution was transferred in to a 5 mm NMR tube. The parameters used for NMR relaxation time measurements and magnetic resonance imaging acquisition are the same as the ones used for the study of water in sponge,

and can be found in section 2.3. For each sample, the ratio (*R*) between the CPMG T_2 relaxation time and T_2 maps was evaluated and plotted against the CPMG T_2 relaxation time. This plot is shown in figure 3.2, which highlights that the ratio is not constant but has a linear dependence with T_2 relaxation time.

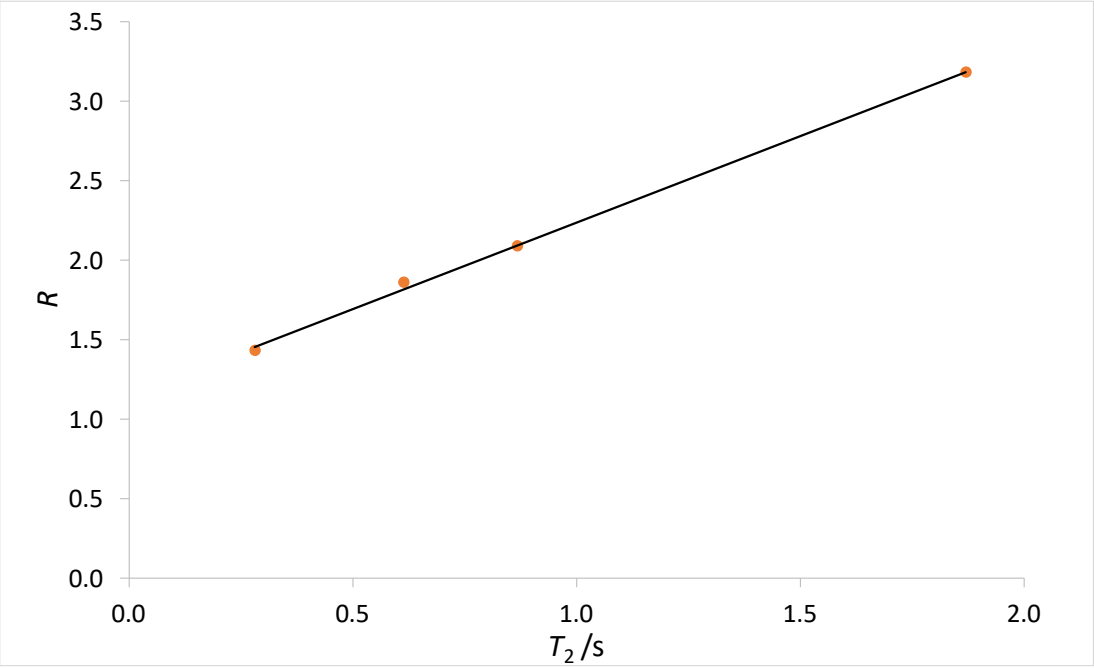


Figure 3.2 Plot of the ratio between the CPMG T_2 relaxation time and T_2 evaluated from T_2 maps R vs T_2 obtained from RARE sequence. The black line represents a linear fit of the data. CPMG data were recorded collecting 64 spectra, varying the number of echoes from 0 to 2048, logarithmically spaced, with an echo time of 2 ms and repetition time of 15 s and a spectral width of 100,000 Hz. T_2 relaxation time maps were acquired with a RARE factor of 128, echo time of 8 ms and repetition time of 15 s. a 64 × 128-pixels matrix, with a field of view of 25 × 50 mm.

3.2.5. Statistical analysis

Scatter plots of X-ray μCT maximum opening versus bulk T_2 relaxation time or MRI T_2 relaxation time, were created. Linear regression analysis was performed on both sets of data to evaluate the correlation between MR T_2 relaxation times and maximum

opening. SPSS version 25 was used for statistical analysis[51], and the statistical significance was set as $p < 0.05$.

3.3. Results

Figure 3.3 shows 3D rendered X-ray μCT images for a single uncompressed and compressed sponge plug. In the X-ray μCT images (figure 3.3a, b), the typical open-cell structure is visible, composed of polymeric struts (blue) and void (black). Figure 3.3b also shows that the compression of the sponge causes some pores to collapse, while others elongate. The change in pore dimensions can be more easily observed in figures 3.3c and d, which show sections of maximum opening for the compressed and uncompressed plug, for a plane through the centre of the sponge. From analysis of the data in figures 3.3b and d, it was observed that when evaluating the maximum opening for compressed plugs, smaller pores are aggregated to generate a single maximum opening value. This is supported by the data shown in Table 3.1, which reports the number of pores for all the uncompressed and compressed plugs studied. Here, the number of pores was found to be lower for compressed plugs. This can be explained by the collapse of smaller pores and their subsequent amalgamation by the software, which considers them to be a single pore rather than a number of smaller pores.

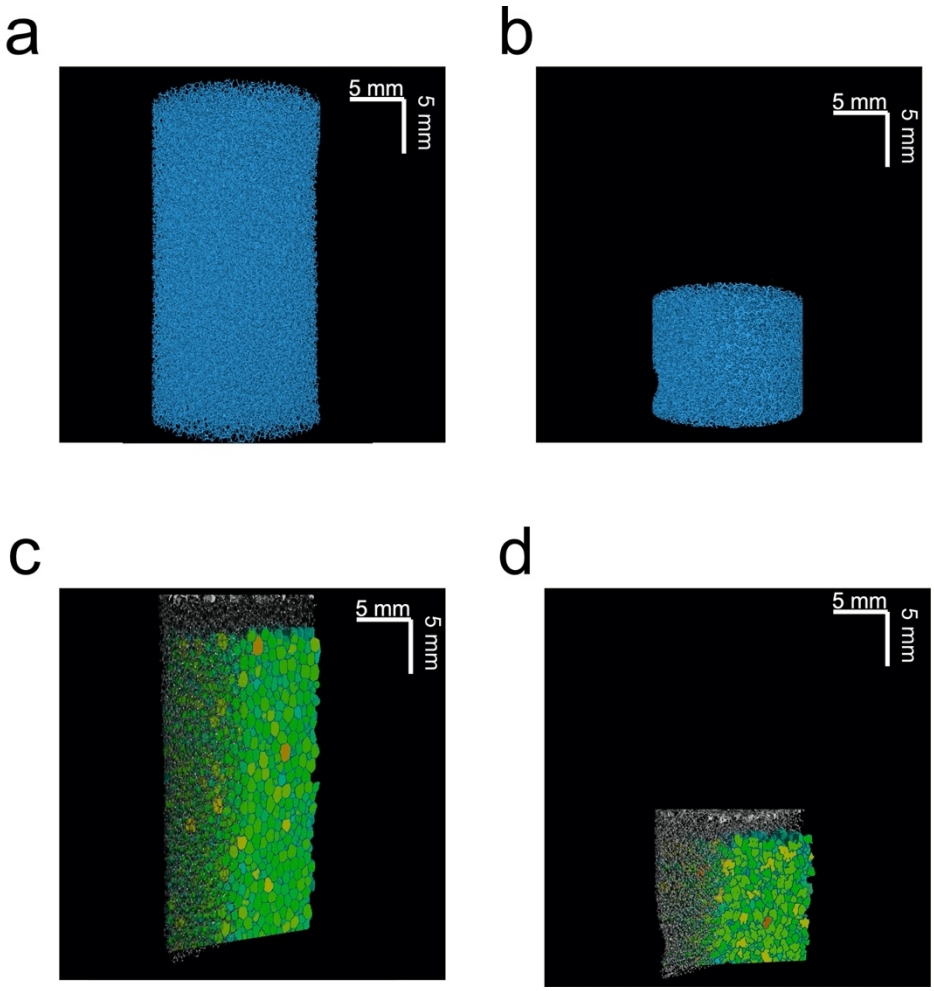


Figure 3.3 3D μCT renderings of an a) uncompressed and b) 60 % compressed plug. 3D renderings of a vertical clipping plane, with the maximum opening distribution for c) uncompressed and d) 60 % compressed plug. All images are for the same plug (plug B_2).

	Plug	Uncompressed	60 % compressed
Number of pores	**A1**	7882	2560
	A2	8475	3575
	A3	8396	3921
	B1	9919	3497
	B2	9135	3051
	B3	8851	2837
	C1	8400	2885
	C2	7662	3018
	C3	6405	3007

Table 3.1: Total number of pores for uncompressed and compressed plugs from X-ray μCT.

Figure 3.4a shows T_2 relaxation maps for water in the same plug as figure 3.3. These images show a decrease in T_2 relaxation time when the sponge is compressed (figure 3.4a) compared to the uncompressed sponge (figure 3.4b).

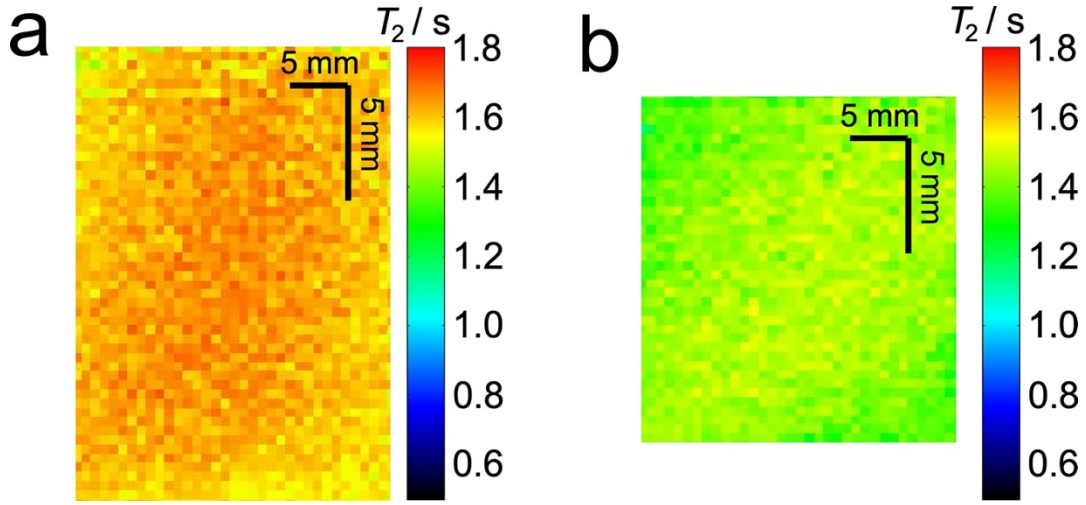


Figure 3.4 . Extracted sections from 2D ^{1}H MR T_2 relaxation maps of 7° dH water in an uncompressed (a) and 60% compressed (b) sponge plug. Both images are for the same plug (plug B_2).

Figure 3.5, 3.6, and 3.7 show the distributions of maximum opening (figure 3.5), determined by X-ray μCT, and T_2 relaxation times (Figure 3.6, and 3.7), determined from MRI and bulk NMR measurements, respectively, for the same uncompressed and 60 % compressed plugs. All distributions, indicate an average smaller maximum opening and shorter T_2 relaxation time for compressed sponge plugs compared to uncompressed plugs. The average maximum opening and T_2 relaxation times, for these distributions, are given in table 3.2.

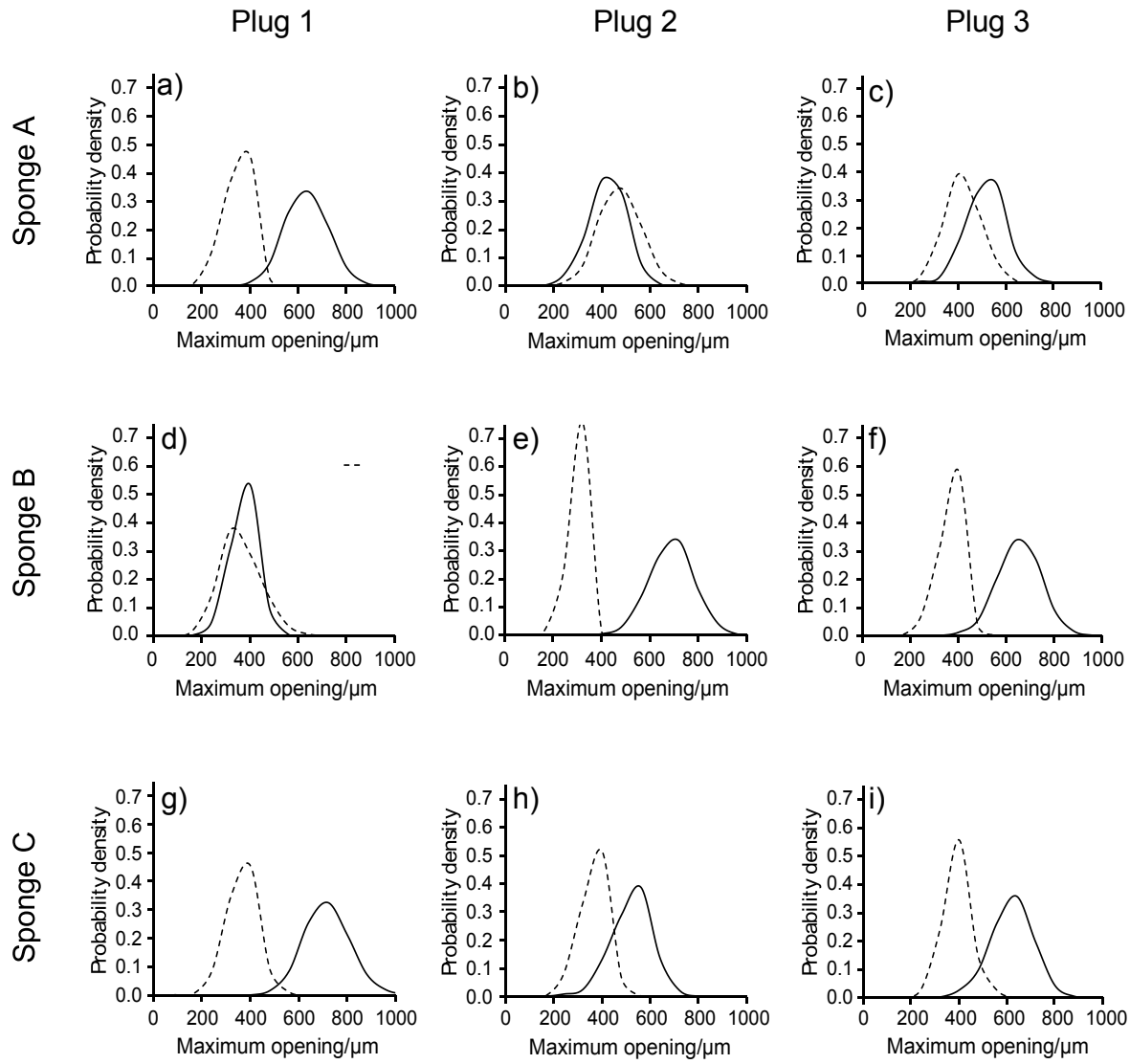


Figure 3.5 Plots of the distribution of maximum opening determined from μCT for compressed (- -) and uncompressed (—) plugs extracted from sponge A (a-c), sponge B (d-f), and sponge C (g-i).

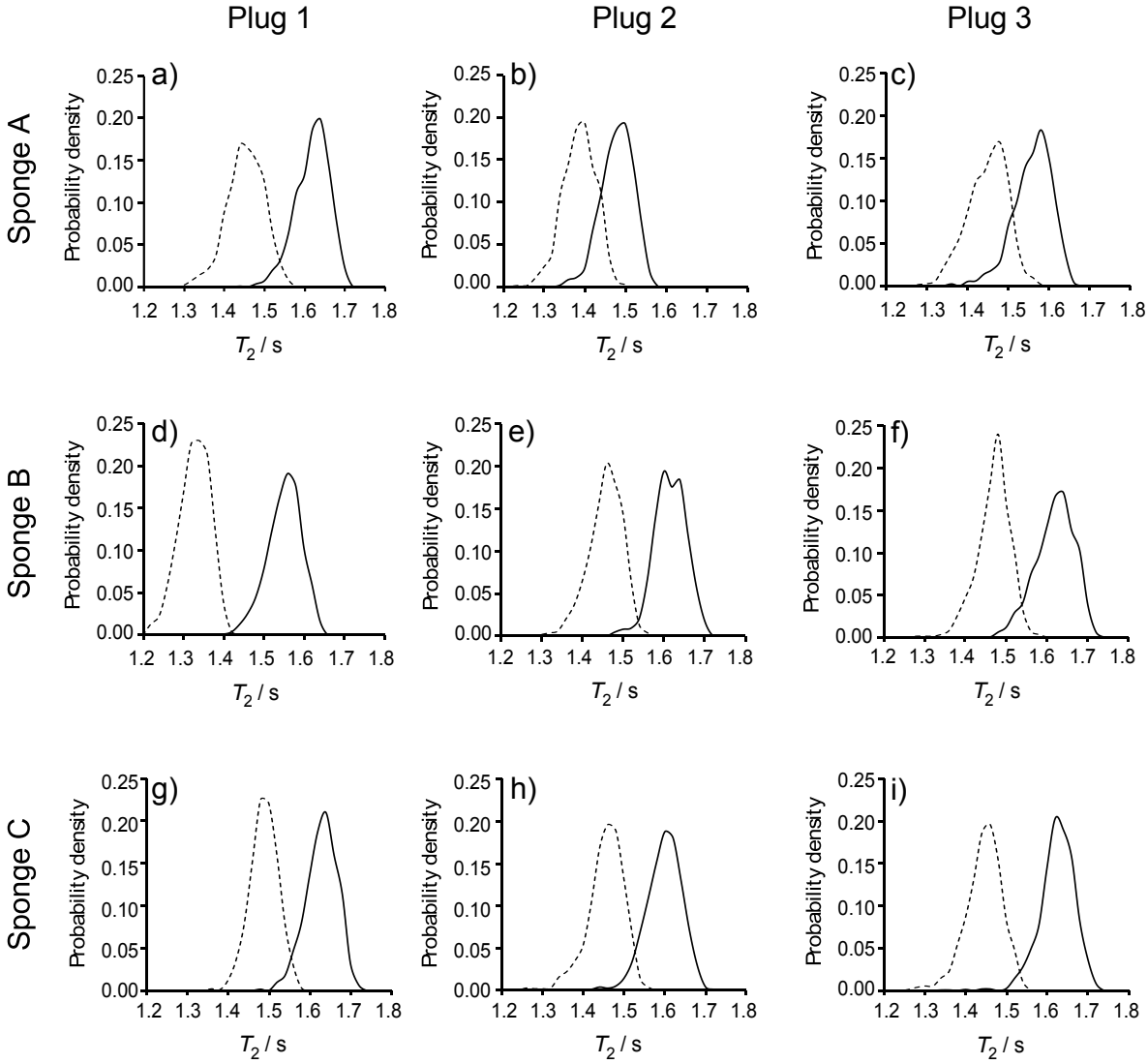


Figure 3.6 Plots of the distribution of T_2 relaxation time determined from T_2 relaxation MR maps for compressed (- -) and uncompressed (¯) plugs extracted from sponge A (a-c), sponge B (d-f), and sponge C (g-i).

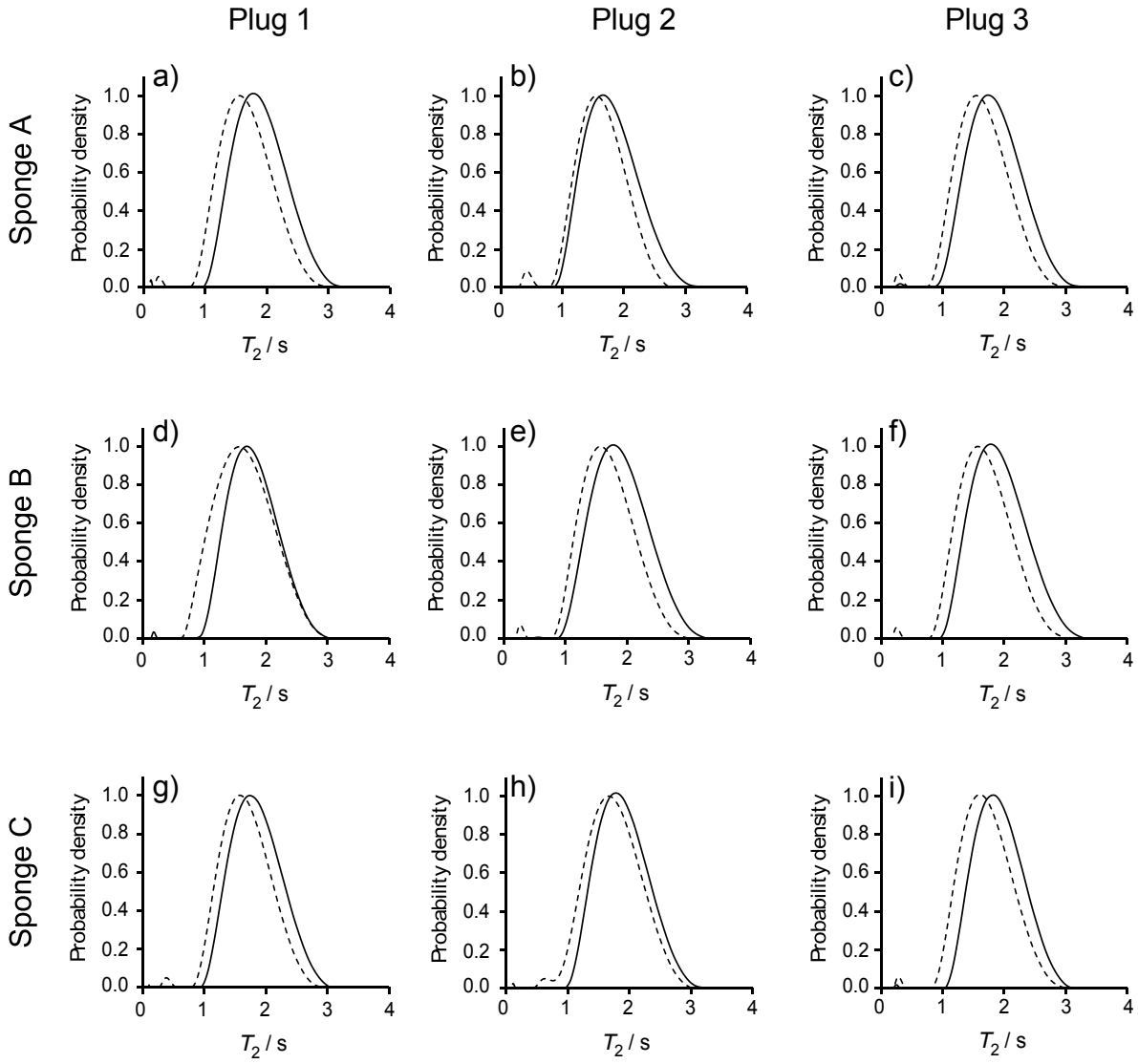


Figure 3.7 *Plots of the distribution of T_2 relaxation time determined from bulk T_2 relaxation time measurements for compressed (- -) and uncompressed (—) plugs extracted from sponge A (a-c), sponge B (d-f), and sponge C (g-i).*

	Plug	Average Max. Op. / μm	Average T_2 from MRI / s	Bulk T_2 / s
Uncompressed	**A1**	633 ± 98	1.61 ± 0.04	1.7
	A2	422 ± 79	1.47 ± 0.04	1.47
	A3	517 ± 86	1.57 ± 0.05	1.64
	B1	375 ± 59	1.54 ± 0.04	1.61
	B2	689 ± 96	1.63 ± 0.04	1.71
	B3	653 ± 84	1.61 ± 0.05	1.73
	C1	716 ± 100	1.62 ± 0.04	1.68
	C2	521 ± 87	1.59 ± 0.04	1.72
	C3	620 ± 92	1.62 ± 0.04	1.76
Compressed	**A1**	351 ± 32	1.44 ± 0.05	1.470
	A2	473 ± 92	1.38 ± 0.04	1.36
	A3	421 ± 81	1.44 ± 0.05	1.47
	B1	440 ± 88	1.32 ± 0.04	1.26
	B2	301 ± 39	1.45 ± 0.04	1.46
	B3	367 ± 56	1.46 ± 0.04	1.51
	C1	365 ± 69	1.48 ± 0.03	1.47
	C2	365 ± 61	1.45 ± 0.04	1.46
	C3	391 ± 28	1.44 ± 0.04	1.56

Table 3.2 Average maximum opening from μCT, average MR T_2 relaxation time from T_2 relaxation MR map and bulk T_2 relaxation time determined from a mono- or bi-- exponential fit to the CPMG data. The variability in average maximum opening and T_2 relaxation time from MR maps, comes from the standard deviation of values across the sample.

The relationship between average maximum opening with average T_2 relaxation time, determined from MRI (Figure 3.8a) and bulk NMR measurements (Figure 3.8b), are plotted in figure 3.8, for all uncompressed and compressed plugs.

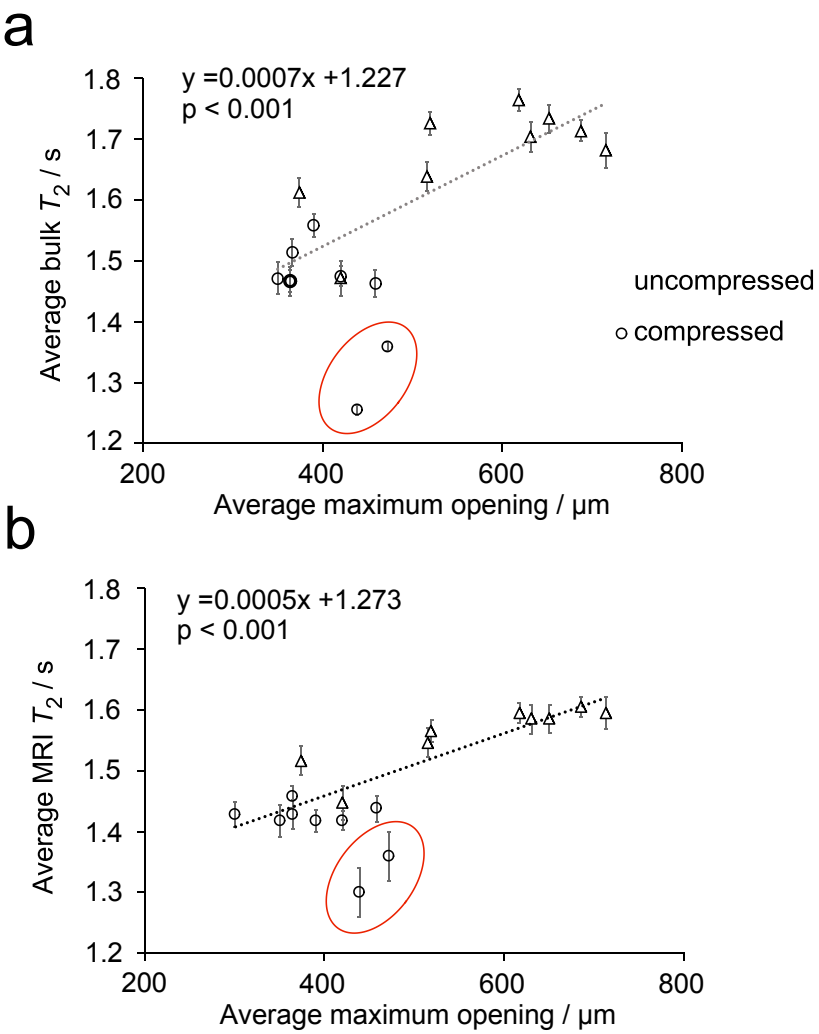


Figure 3.8 Plot of the average maximum opening vs bulk T_2 MR relaxation time (a) and average T_2 relaxation time determined from T_2 relaxation MR maps (b) for 7° dH water in uncompressed and compressed sponge plugs. The dotted lines are a linear fit of the data. Two outlying samples are circled in each plot.

It can be seen that, for both plots in figure 3.8, there appears to be a linear relationship between the maximum opening and the T_2 relaxation time, where T_2 relaxation time

decreases with decreasing maximum opening. Statistical analysis of these data found a p-value < 0.001 for both sets of data, which indicates a correlation between these parameters. In both plots, two outlying points can be observed, which are circled. These outlying plugs are from two compressed sponge plugs and are believed to be related to a bending of the plug when compressed. This deformation can be observed in figure 3.9. As a result of this non-uniform compression in these plugs, these values were not included for the data fitting.

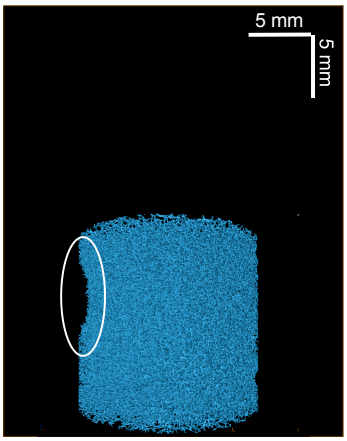


Figure 3.9 3D μCT reconstructed image of one of the two 60 % compressed plug related to the outliers points in figure 7. An indentation, caused by a bending of the plug when compressed, is highlighted by a white circle.

3.4. Discussion

Our results, across multiple sponges and compression, have revealed a correlation between pore maximum opening and T_2 relaxation time for fluid with pores. From a close inspection of the X-ray μCT images in figure 3.3, it can be observed that, when compressed, some pores collapse while others are elongated. This observation is confirmed by the decrease in the average maximum opening. However, it appears that the maximum opening tends to overestimate the actual real pore size of single pores

in compressed plugs. Despite this, maximum opening can still be considered a reliable measure for sponge compression, because it represents a local, rather than a single pore, characteristic. We found that maximum opening correlates with the T_2 relaxation time for fluid within the pore network (figure 3.8) and correlates better than pore size (equivalent diameter). This is possibly the case because MRI is not able to distinguish single pores, because it has lower spatial resolution compared to X-ray μCT. Thus, T_2 relaxation times also represent a local property rather than a single pore characteristic, which is comparable with maximum opening. While the characterisation of the pores is limited by the resolution, and image processing modalities (segmentation), the resolution at which scans were acquired was sufficient to visualise the pores of the sponge both at uncompressed and 60% compressed conditions.

Comparison of maximum opening values, between different foam plugs, has also revealed a significant variability in pore dimensions between samples within the same production batch, and even within the same sponge. In our experiments, plugs were extracted from three different sponges within the same production batch. The variation in average maximum opening, between uncompressed plugs, was observed to be 422 ± 79 μm to 633 ± 97 μm (sponge A), 375 ± 59 μm to 688 ± 96 μm (sponge B) and 520 ± 87 μm to 716 ± 100 μm (sponge C). This shows that there is variability in the average maximum opening between sponges. This demonstrated the heterogeneity in pore dimensions within the polyurethane block from which the sponges were cut.

Linear regression analysis, for the data in figure 3.8, demonstrates a positive linear correlation between bulk and MRI T_2 relaxation time (R^2 = 0.868, $p<0.001$ and R^2 =

0.915, $p<0.001$ respectively), with the maximum opening of the pore. In particular, figure 3.8 shows that as the pore decreases in size, there is a corresponding reduction in T_2 relaxation time. While this effect has been observed in rock samples, it has not been previously observed in polymeric foams. Moreover, this relationship is found to be much subtler in PU foams than in rocks, which is to be expected given the lack of paramagnetic species and small difference in magnetic susceptibility. Yet, these results demonstrate a valuable technique by which these materials can be characterised, supporting studies investigating the application of foams in a variety of environments.

3.5. Conclusion

In this chapter, we have shown that despite the similar magnetic susceptibilities between water and polyurethane, ^{1}H magnetic resonance T_2 relaxation times are sensitive to pore sizes within PU open-cell foams. Plots of maximum opening, determined by X-ray μCT, *vs* T_2 MR relaxation time are found to have a linear correlation. We have observed, using both X-ray μCT and MR relaxation times, that when a sponge is compressed, there is a decrease in pore dimensions. These X-ray μCT and MR measurements have also demonstrated that it is possible to characterise the pore dimensions across different sponges, showing the variability resulting from the manufacturing process. We believe such measurements will be of benefit to those studying the performance and behaviour of polyurethane open-cell foams in a variety of applications, where there is a link between pore size distribution and performance of the sponge or products within the sponge. In particular, if combined with MRI measurements on food residues within sponges (explored in chapter 4), and MRI direct

visualization of biofilm in sponges (explored in chapter 5), these results offer the opportunity for a real time visualization of biofilm growth in relation to sponge characteristics and food viability to a new way to study.

3.6. References

1 Aubert, J. & Clough, R. Low-density, microcellular polystyrene foams. *Polymer* **26**, 2047, doi:doi.org/10.1016/0032-3861(85)90186-7 (1985).
2 Fossey, D. & Smith, C. Fabrication of Open-Cell Polyethylene Foam. *J. Cell. Plast.* **9**, 268 (1973).
3 Starry, G. L. Sponge cleaning device. US patent 3,345,669 (1967).
4 Ma, Q., Cheng, H., Fane, A. G., Wang, R. & Zhang, H. Recent development of advanced materials with special wettability for selective oil/water separation. *Small* **12**, 2186 (2016).
5 Kumaran, M. & Bomberg, M. Thermal performance of sprayed polyurethane foam insulation with alternative blowing agents. *J. Therm. Insul.* **14**, 43 (1990).
6 Jones, V., Grey, J. E. & Harding, K. G. Wound dressings. *BMJ* **332**, 777 (2006).
7 Pollak, A. N. Use of negative pressure wound therapy with reticulated open cell foam for lower extremity trauma. *J. Orthop. Trauma* **22**, S142 (2008).
8 Menges, G. & Knipschild, F. Estimation of mechanical properties for rigid polyurethane foams. *Polym. Eng. Sci.* **15**, 623 (1975).
9 Yong, W. & Jie, L. Use of polyurethane foams complex material to preserve moisture and fertility. *Polymer-Plastics Technology and Engineering* **46**, 943 (2007).
10 llabres, C. M. & rose, B. E. Antibacterial properties of retail sponges. *J. Food Prot.* **52**, 49 (1989).
11 Gong, L., Kyriakides, S. & Jang, W.-Y. Compressive response of open-cell foams. Part I: Morphology and elastic properties. *Int. J. Solids Struct.* **42**, 1355 (2005).
12 Gama, N. V., Ferreira, A. & Barros-Timmons, A. Polyurethane foams: past, present, and future. *Materials* **11**, 1841 (2018).
13 Ashida, K. *Polyurethane and related foams: chemistry and technology*. (CRC press, 2006).
14 Lee, S.-T. & Ramesh, N. S. *Polymeric foams: mechanisms and materials*. (CRC press, 2004).
15 Blazejczyk, A. Morphometric Analysis of One-Component Polyurethane Foams Applicable in the Building Sector via X-ray Computed Microtomography. *Materials* **11**, 1717 (2018).
16 Van Brakel, J., Modrý, S. & Svata, M. Mercury porosimetry: state of the art. *Powder Technol.* **29**, 1 (1981).
17 Ziel, R., Haus, A. & Tulke, A. Quantification of the pore size distribution (porosity profiles) in microfiltration membranes by SEM, TEM and computer image analysis. *J. Membr. Sci.* **323**, 241 (2008).
18 Cnudde, V. & Boone, M. N. High-resolution X-ray computed tomography in geosciences: A review of the current technology and applications. *Earth-Sci. Re.* **123**, 1 (2013).
19 Marica, F. *et al.* Spatially resolved measurement of rock core porosity. *J. Magn. Reson.* **178**, 136 (2006).
20 Ho, S. T. & Hutmacher, D. W. A comparison of micro CT with other techniques used in the characterization of scaffolds. *Biomaterials* **27**, 1362 (2006).

21 Yao, Y. & Liu, D. Comparison of low-field NMR and mercury intrusion porosimetry in characterizing pore size distributions of coals. *Fuel* **95**, 152 (2012).
22 Swapp, S. *Scanning Electron microscopy*, <https://serc.carleton.edu/research_education/geochemsheets/techniques/SEM.html> (2016).
23 Bang, S. S., Galinat, J. K. & Ramakrishnan, V. Calcite precipitation induced by polyurethane-immobilized Bacillus pasteurii. *Enzyme Microb. Technol.* **28**, 404 (2001).
24 Wu, D., Wu, W., Yu, Z., Zhang, C. & Zhu, H. Facile preparation and characterization of modified polyurethane sponge for oil absorption. *Ind. Eng. Chem. Res.* **53**, 20139 (2014).
25 Souza, D. A. d., Araujo, D. M. d., Carvalho, C. d. F. & Yoshida, M. I. Physico-chemical analysis of flexible polyurethane foams containing commercial calcium carbonate. *Mater. Res.* **11**, 433 (2008).
26 Peng, S., Hu, Q., Dultz, S. & Zhang, M. Using X-ray computed tomography in pore structure characterization for a Berea sandstone: Resolution effect. *J. Hydrol.* **472**, 254 (2012).
27 Maire, E. & Withers, P. J. Quantitative X-ray tomography. *Int. Mater. Rev.* **59**, 1 (2014).
28 Long, H., Swennen, R., Foubert, A., Dierick, M. & Jacobs, P. 3D quantification of mineral components and porosity distribution in Westphalian C sandstone by microfocus X-ray computed tomography. *Sediment. Geol.* **220**, 116 (2009).
29 Brabant, L. *et al.* Three-dimensional analysis of high-resolution X-ray computed tomography data with Morpho+. *Microsc. Microanal.* **17**, 252 (2011).
30 Shastry, A. *et al.* In-Situ High Resolution Dynamic X-ray Microtomographic Imaging of Olive Oil Removal in Kitchen Sponges by Squeezing and Rinsing. *Materials* **11**, 1482 (2018).
31 Bultreys, T. *et al.* Fast laboratory-based micro-computed tomography for pore-scale research: illustrative experiments and perspectives on the future. *Adv. Water Resour.* **95**, 341 (2016).
32 Borgia, G., Bortolotti, V. & Fantazzini, P. Changes of the local pore space structure quantified in heterogeneous porous media by 1 H magnetic resonance relaxation tomography. *J.Appl. Phys.* **90**, 1155 (2001).
33 Attard, J. *et al.* Spatially resolved T1 relaxation measurements in reservoir cores. *Magn. Reson. Imaging* **9**, 815 (1991).
34 Guillot, G. *et al.* Characterisation of wetting heterogeneities in sandstone rocks by MRI. *Magn. Reson. Imaging* **12**, 365 (1994).
35 Merrill, M. Porosity measurements in natural porous rocks using magnetic resonance imaging. *Appl. Magn. Reson.* **5**, 307 (1993).
36 Britton, M. M. Porous Media Studied by MRI. *eMagRes*, doi:10.1002/9780470034590.emrstm1263 (2011).
37 Watson, A. T. & Chang, C. P. Characterizing porous media with NMR methods. *Prog. Nucl. Magn. Res. Sp.* **31**, 343 (1997).
38 Hürlimann, M. D. Effective gradients in porous media due to susceptibility differences. *J. Magn. Reson.* **131**, 232 (1998).

39 Stingaciu, L. *et al.* Determination of pore size distribution and hydraulic properties using nuclear magnetic resonance relaxometry: A comparative study of laboratory methods. *Water Resour. Res.* **46** (2010).
40 Wang, R. *et al.* Xenon NMR measurements of permeability and tortuosity in reservoir rocks. *Magn. Reson. Imaging* **23**, 329 (2005).
41 Schoenfelder, W., Gläser, H.-R., Mitreiter, I. & Stallmach, F. Two-dimensional NMR relaxometry study of pore space characteristics of carbonate rocks from a Permian aquifer. *J. Appl. Geophys.* **65**, 21 (2008).
42 Washburn, K. E. & Madelin, G. Imaging of multiphase fluid saturation within a porous material via sodium NMR. *J Magn. Reson.* **202**, 122 (2010).
43 Von Der Schulenburg, D. G., Paterson-Beedle, M., Macaskie, L., Gladden, L. & Johns, M. Flow through an evolving porous media—Compressed foam. *J. Mater. Sci.* **42**, 6541 (2007).
44 Masschaele, B. *et al.* HECTOR: A 240kV micro-CT setup optimized for research. *J. Phys. Conf. Ser.* **463**, 012012 (2013).
45 Vlassenbroeck, J. *et al.* Software tools for quantification of X-ray microtomography at the UGCT. *Nucl. Instrum. Methods Phys. Res. B.* **580**, 442 (2007).
46 Hennig, J., Nauerth, A. & Friedburg, H. RARE imaging: a fast imaging method for clinical MR. *Magn. Reson. Med.* **3**, 823 (1986).
47 Prospa, Magritek, Wellington, New Zealand.
48 Bray, J. M., Davenport, A. J., Ryder, K. S. & Britton, M. M. Quantitative, In Situ Visualization of Metal-Ion Dissolution and Transport Using 1H Magnetic Resonance Imaging. *Angew. Chem. Int. Ed.* **55**, 9394 (2016).
49 Provencher, S. W. A constrained regularization method for inverting data represented by linear algebraic or integral equations. *Comput. Phys. Commun.* **27**, 213 (1982).
50 Law, S. J. & Britton, M. M. Sizing of reverse micelles in microemulsions using NMR measurements of diffusion. *Langmuir* **28**, 11699 (2012).
51 IBM SPSS statistics for Macintosh v. 25.0 (NY: IBM corp, Armonk, 2017).

4 VISUALIZATION OF BIOFILMS AND BIOFILM NUTRIENTS IN POLYURETHANE SPONGES

4.1 Introduction

Sponges are extensively used to clean surfaces inside houses and other human environments, such as hospitals or industries. Synthetic sponges were first introduced in the 1940s and since then they have become established as the market leader, thanks to their low cost and ease of production.[1] Sponges are most commonly used to remove soil from surfaces, especially kitchen surfaces. However, due to their porous structure, soil can get trapped within sponges. The ease of soil removal can be dependent on the part of the sponge it is trapped in. For instance, solid food residues, like food particles or solid fat, are generally deposited on the external part of the sponge and are easy to remove. Alternatively, liquid soils, such as vegetable oils, starch, or dissolved proteins, can be trapped inside the porous structure, through processes such as capillary force.[2,3] In these cases, removal of these soils is much harder. The food and the water trapped within the sponge constitute a perfect environment for bacteria and biofilm growth. Indeed, studies have found that kitchen sponges are the second-highest source of bacteria within the house,[4,5] where bacteria populations can reach densities of up to 10^3 CFU per gram.[6] Bacteria and biofilms can cause malodour of the sponge and can cross-contaminate surfaces and humans, causing bacterial infections. Understanding how biofilm develops within sponges and how this is related to the soil distributed within the porous structure, could help to understand biofilm formation and its prevention. To achieve this, biofilm and soil visualization within sponges is necessary.

Imaging biofilms within a porous medium is challenging, because porous systems are usually opaque and irregular. For instance, optical techniques are strongly affected by the irregularity and opacity of the porous media because the former causes image blurriness and background signal, while the latter limits the depth of field of observation.[7]. Different techniques have been used to overcome this issue, like X-ray micro-CT (μCT), scanning electron microscopy (SEM), Transmission electron microscopy (TEM), and confocal laser scanning microscopy (CLSM). CLSM can visualise biofilms in their native hydrated state, making it possible to understand the biofilm structure in sponges.[6] However, CLSM requires the use of dyes to stain the bacteria[8] which can be problematic when the porous media tends to retain liquids, due to the stain of the sponge itself. One of the advantages of CLSM, is the ability to use dyes which can selectively stain either the bacteria or extra polysaccharides (EPS) matrix. For studies on porous media, both types of dyes have been used. For instance, *syto9*, which stains nucleic acids within bacteria, has been used to investigate the clogging of porous media caused by biofilm growth.[9] Similar studies have been also conducted using fluorescent labelled lectins, which specifically stain the EPS of biofilm.[10] Yet, while this works well for non-absorbing porous media, problems can arise for porous systems like flexible open-cell polyurethane sponges (FPU), because of their ability to retain liquids used to dye biofilms.

The visualization of biofilms is not enough in itself to understand the development of biofilms within FPU. For greater understanding of biofilm growth and in FPU, a correlation between the growth behaviour and food availability within the sponge is

necessary. To achieve this, techniques need to be used that are able to generates contrast between food and biofilms within open-cell polyurethane, and that are able to visualize biofilm growth in a non-invasive way. µCT has been successfully used to visualize the displacement and relocation of olive oil inside an open-cell foam in a multiphase fluid environment and to assess the level of soil removal.[3] However, pre-treatments were necessary to add a contrast agent to the oil to be able to distinguish the oil from the pore matrix.[3] The use of contrast agents is also required when using µCT to image biofilm in porous media, because of the similar X-ray attenuation coefficient between biofilms and water.[11] The use of contrast agents, such as barium sulphate or silver microparticles can both produce artefacts in the image or have negative effects on bacteria growth.[12] The needs of pre-treatments and use of contrast agents limits the use of µCT for in-situ visualization on biofilm development via µCT. The requirement of using a contrast agent to visualize oil, within a polyurethane sponge, and separate it from other substances can be overcome by using magnetic resonance imaging (MRI). Using MRI, contrast can be generated between the porous media matrix and the fluid within it by using relaxation times, molecular motion and chemical shift.[13] For instance, liquids have longer T_2 relaxation times compared to solids, which enable contrast between the former and the latter. MR Chemical Shift Selective Saturation (CHESS) sequence is able to selectively observe difference components in multicomponent systems by using the difference in chemical shift between protons within the different species. This enables the generation of separate images, for each chemical species containing NMR active species, in the system. For instance, CHESS has been successfully used to selectively image oil and water in systems where these were mixed, by selectively exciting water and oil protons.[14] In

this regard, CHESS has been successfully used to improve the understanding of mixing in oil-water flow in within the petrochemical industry.[14] However, CHESS imaging porous media can be challenging because of the line broadening for peaks in spectra caused by the porous media itself.[15] Indeed, a reduction of the MR T_2 relaxation time of liquids in porous media is observed, which generates the broadening of the peaks. This broadening can prevent the discrimination of peaks in the NMR spectra related to water protons and peaks related to protons within the oil, making difficult or even impossible the application of CHESS imaging.[15]

In this chapter, CLSM, for biofilm visualization, and chemical shift selective MRI, to visualize biofilm nutrients within open-cell polyurethane sponges have been tested. For biofilm visualization using CLSM, two different dyes have been used: acridine orange, which stains bacteria, and calcofluor white, which stains the EPS of the biofilm. For soil visualization, MR CHESS sequence have been tested to selectively visualise water and oil in sponges containing the two liquids

4.2 Materials and methods

4.2.1 Biofilm growth in sponge

4.2.1.1 Sample preparation

Sponge cubes, of 1 cm^3 in volume, were produced using scissor from polyurethane sponges (Spontex, Colombes, France, Batch n° = 7124813). They were washed with distilled water to remove any residual particles from manufacturing trapped within the porous matrix. After washing, the cubes were left to dry for a few hours. Once dry, the cubes were autoclaved in a glass jar for 30 minutes at 121°C.

4.2.1.2 Bacteria and Biofilm growth

For growth of bacteria, a colony of *Pseudomonas fluorescens* was transferred from an old agar plate to a new one. The plate was incubated at 25°C for 24 h. After 24 h, a bacteria colony was transferred from the agar plate into a 250 ml flask containing 50 ml of Trypticase soy broth (TSB) (30g/L). This was then incubated at 25°C for 16 h to a final bacteria concentration of 2 x 10^9 CFU/ml.[16] After 16 h, 40 µl of the solution was transferred in each well of a 6 well plate, each containing 10 ml of fresh TSB. A single sponge cube previously prepared was then inserted in each well (figure 4.1). The plate was sealed and inserted in a water bath at 25°C for 72 h. All solutions and glassware were autoclaved for 30 minutes at 121° C before use.

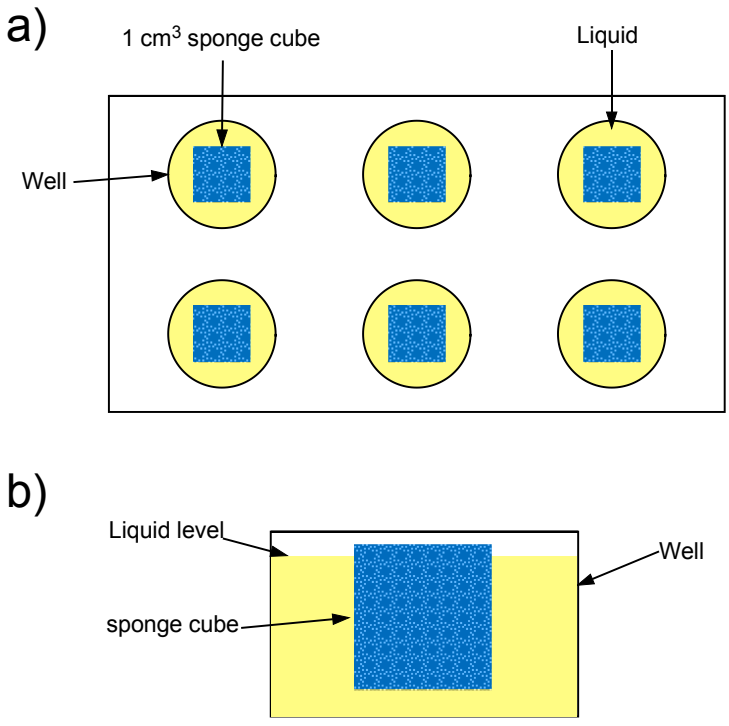


Figure 4.1 Schematic diagram of a) a six well-plate, observed from the top, showing the growth liquid (yellow) and the sponge cube (blue) within each well and b) a side view of a single well.

4.2.1.3 Biofilm staining and confocal microscopy

After 72 h, the sponge cubes were removed from the 6-well plate and washed three times with phosphate buffered saline (PBS) to remove non-adhered cells. For the staining of the biofilm within the sponge, two different dyes were used: acridine orange (Thermo-Fisher) and calcofluor white m2r (Sigma-Aldrich). Both acridine orange and calcofluor white m2r were prepared at three different concentrations, by dilution with PBS. The three dye concentrations were 0.002 % w/v, 0.001 % w/v, and 0.0005 % w/v for acridine orange and 0.1 % w/v, 0.05 % w/v and 0.025 w/v for calcofluor white m2r. For the staining, two different procedures were followed: (i) sponge cubes were immersed in the dye solution and left to stain in the dark for 20 minutes; (ii) 1 ml of dye was injected in sponge cubes using a syringe, and left 20 minutes in the dark. After 20 minutes, the cubes were washed three times with PBS, to remove excess dye. Confocal microscopy images were acquired using a Confocal Leica TCS SPE microscope with a 40x magnification oil lens. Acridine orange was excited by a 405 nm laser and emission was detected in the range of 488 - 550 nm. Calcofluor white M2R was instead excited by a 405 nm laser and emission was detected in the range 430 – 550 nm. Confocal microscopy was also performed on pure sponge cubes to test the auto-fluorescence of the sponge matrix. For the image acquisition, a Confocal Leica TCP SPE microscope with a 40x magnification oil lens was used. The excitation and emission wavelength ranges used for the experiment are visible in table 4.1

Excitation wavelength / nm	Emission wavelengths range / nm
405	- 470 - 530 - 560 - 630 - 670 - 730
488	- 490 - 550 - 550 - 610
532	- 550 - 610
635	- 670 - 730

Table 4.1 List of the excitation and emission wavelengths used for the CLSM image acquisition of pure polyurethane sponge cubes without biofilm.

4.2.2 Chemical shift selective imaging

4.2.2.1 Sample preparation

For the optimization of CHESS imaging, phantom samples were prepares using three NMR 5 mm tubes filled with sunflower oil, water, and a 50 - 50 mixture of sunflower oil and water respectively. The three tubes were inserted in an appropriate sample holder (visible in figure 4.2). For CHESS imaging of water and oil in sponges, three cylindrical plugs, of diameter 5 mm and height 1 cm, were extracted from polyurethane sponges (Spontex, Colombes, France, Batch n° = 7124813). Phantom samples of oil and water in sponge were prepared soaking the three sponge plugs in water, sunflower oil, and a 1% v/v of oil in water mixture respectively. For the NMR spectroscopy measurement, each sponge plug was inserted in a 10 mm NMR tube, while for CHESS experiments, the three sponges were inserted togheter in a 20 mm diameter vials.

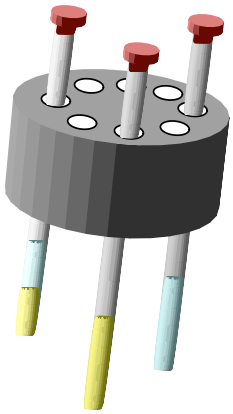


Figure 4.2 Schematic diagram of the sample holder and the positioning of the NMR tubes for the CHESS experiments on water (light blue) and sunflower oil (yellow).

4.2.2.2 NMR spectroscopy and CHESS experiments

NMR spectroscopy and CHESS images were collected on a Bruker DMX 300 spectrometer, equipped with a 7 T vertical wide-bore superconducting magnet, operating at a proton resonance frequency of 300.13 MHz. All experiments were recorded using a micro2.5 imaging probe at 293 ± 0.3 °K, which was maintained by the temperature of water-cooled gradient coils. Samples were inserted in a ^{1}H 25 mm quadrature radiofrequency birdcage coil (WB40). For spectroscopy measurments on water within the 5 mm NMR tubes, water + oil within the 5 mm NMR tubes, water within sponge plugs and water+oil within sponge plugs, ^{1}H NMR spectra were recorded using the following parameters: number of points 16384, spectral width 10000 Hz, repetition time of 1 s and 2 averages. Axial (horizontal) T_2 relaxation time weighted images of a phantom, composed of 5 mm NMR tubes containing oil, water, and water + oil, and a phantom containing three soaked sponge plugs, were acquired using the spin-echo sequence imaging RARE (Rapid Acquisition with Relaxation Enhancement). Images were recorded using a 1 mm slice thickness and a 128 × 128 pixel matrix, with a field

of view of 30 mm × 30 mm. A RARE factor of 1, echo time of 3.16 ms and repetition time of 15 s were used. Axial CHESS images were recorded using the m-chess sequence from ParaVision software (version 5, Bruker Biospin, Ettlingen, Germany). For the phantom containing the three 5 mm NMR tubes, the images were recorded using 1 mm slice thickness and a 64 × 64 pixel matrix, with a field of view of 30 mm × 30 mm. The minimum echo time was used , with a 15 s repetition time. For the phantom containing the sponge plugs soaked with water, oil, and oil + water, four 2D axial slices of 1mm slice thickness were acquired (figure 4.3).

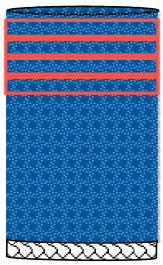


Figure 4.3 Diagram representing a sponge plug used for CHESS images of oil and water in sponge, with the position of the four 1 mm 2D axial slices (red rectangles) recorded.

Images were recorded using 1 mm slice thickness and a 64 × 64 pixel matrix, with a field of view of 16 mm × 16 mm. A minimum echo time mode and a 15 s repetition time were used. For selective exctitation of oil and water peaks, a gaussian RF pulse with spectral width of 500 Hz. Images of water within sponge plugs were produced using an offset of 200 Hz to selective excite water protons, while images of oil where produced usign an offsett of –1200 Hz to selective excit oil aliphatic protons. The 2D axial images produce by selectivly exciting the aliphaitc protons of the oil and the water protons, were subsequentially merged using Matlab, to generate a distribution map of

oil and water within the sponge. The blending was performed by thresholding the water and oil CHESS images, and then by overlapping them.

4.3 Results

4.3.1 Confocal microscopy of biofilm in sponge

Figure 4.4 displays the CLSM images of cubic sponges after 3 days of biofilm growth, dyed with the bath method (figure 4.4a, 4.4b, and 4.4c) and the syringe method (figure 4.4d, and 4.4e) and different concentrations of acridine orange.

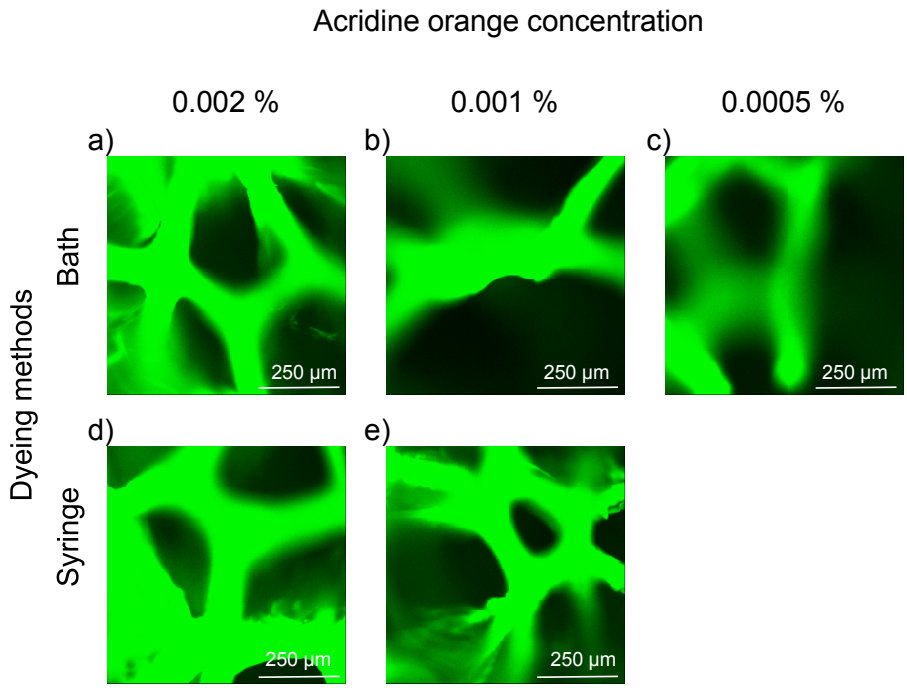


Figure 4.4 CLSM images of sponges after 72h of bacteria growth stained with acridine orange using a bath staining method with different dye concentration a) 0.002 % w/v, b)0.001 % w/v, c) 0.0005 % w/v, and using a syringe staining method with two different dye concentrations d) 0.002 % w/v, and e) 0.001 % w/v. Acridine orange was excited by a 405 nm laser and emission was detected in the range of 488 - 550 nm. Calcofluor white was excited by a 405 nm laser and emission was detected in the range 430 – 550 nm.

For samples dyed with the bath method and showed in figure 4.4a, 4.4b, and 4.4c, the structure of the polyurethane sponge is clearly visible. Images also show halos around the sponge struts, which could be caused by the staining of biofilms. However, this hypothesis cannot be confirmed due to the lack of contrast between the sponge structure and the halo surrounding it. Similar features were observed for samples dyed using a syringe and displayed in figure 4.4d and 4.4e. Indeed, also in these two images, the structure of the sponge is clearly observable with halos surrounding it. However, once again, no biofilm can be detected due to the lack of contrast between the biofilm itself and the sponge structure.

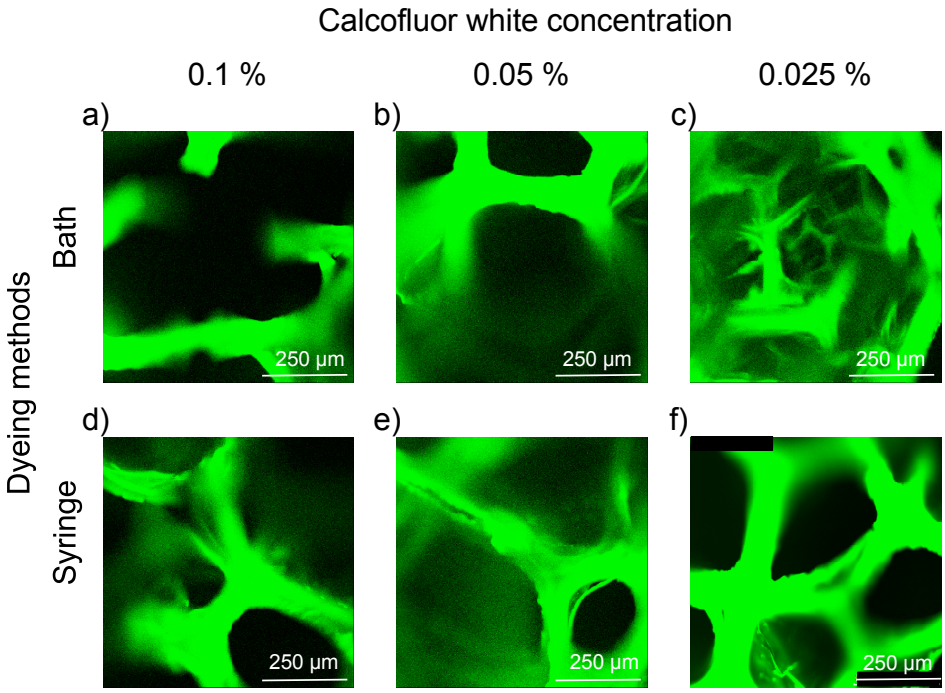


Figure 4.5 CLSM images of sponges after 72h of bacteria growth stained with Calcofluor white using a bath staining method with different dye concentration a) 0.1 % w/v, b)0.05 % w/v, c) 0.025 % w/v, and using a syringe staining method with three different dye concentrations d) 0.1 % w/v, and e) 0.05 % w/v and 0.025 %w/v. Calcofluor white was excited by a 405 nm laser and emission was detected in the range 430 – 550 nm.

CLSM images of samples stained with different concentrations of calcofluor are shown in figure 4.5. As for sponges stained with acridine orange, also in this case the polyurethane sponge struts are clearly visible, surrounded by halos possibly caused by the presence of biofilms. This was the case for all concentrations of dye used, independently for the dying procedure utilized.

4.3.2 Confocal microscopy on sponge

CLSM images acquired for clean sponge plug in absence of biofilms are shown in figure 4.6. Sponge autofluorescence was detected in the range 470 -630 nm (figure 4.6a and 4.6b) when excited with a 405 nm laser. When excited with a laser at 488 nm

instead, the sponge showed a maximum fluorescence intensity between 490 nm and 550 nm (figure 4.6d), while almost no light was detected for wavelengths longer than 550 nm (figure 4.6e). No fluorescence was observed when using an excitation light at 532 nm (figure 4.6f) and 635 nm (figure 4.6g). These results show that even in absence of external dyes, the sponge emits fluorescence light when excited at particular wavelength. This emission can be caused by the dye use to colour the sponge.

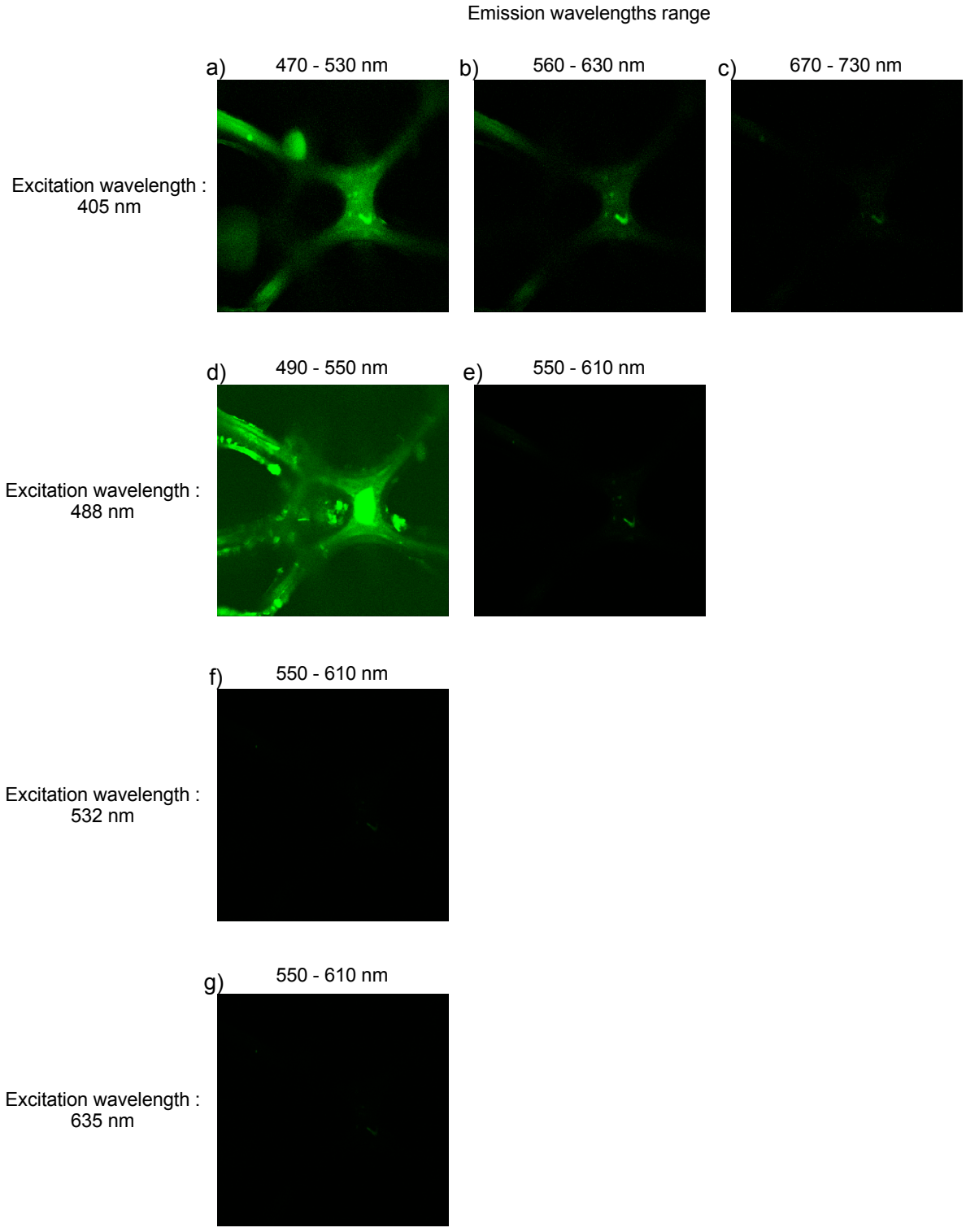


Figure 4.6 CLSM images of a clean sponge in absence of biofilms. The sponge was excited with four different wavelengths using four different lasers. For image acquisition, fluorescence emissions were acquired at various wavelength ranges.

4.3.3 NMR spectroscopy and MR CHESS imaging on water and oil

Figure 4.7 shows the NMR spectrum of sunflower oil and a 50 -50 mixture of water and sunflower oil in 5 mm NMR tubes.

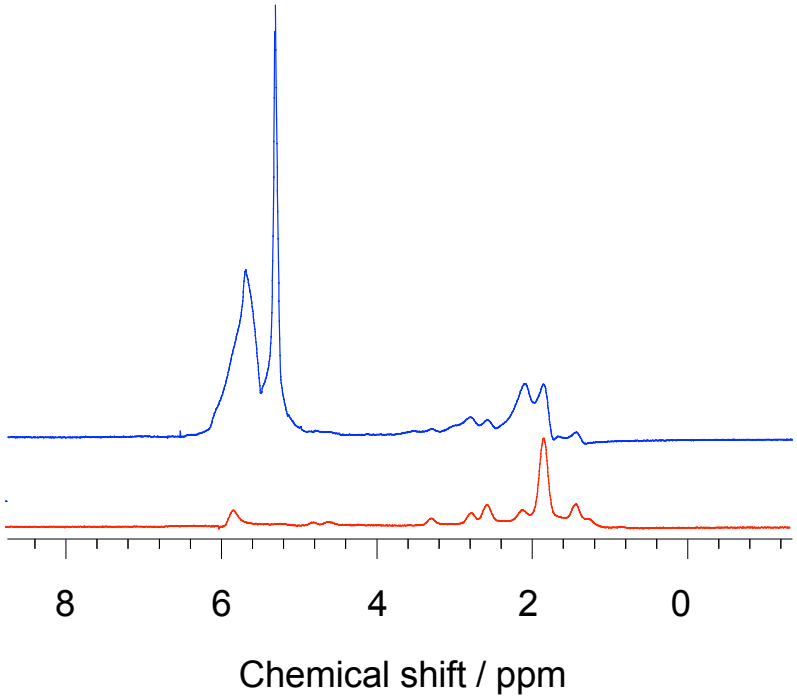


Figure 4.7 NMR spectra of sunflower oil (red) and of a mixture of water and sunflower oil (blue)in five mm NMR tubes.

For the oil, a range of peaks are observed between 1 to 3.5 ppm associated with aliphatic protons. For the oil, a small peak was also detected at 5.8 ppm. For the water and oil mixture, an additional peak is visible at 5.3 which is related to water. The presence of distinct proton resonances, for both water and oil, enables selective excitation enabling the acquisition of CHESS images. For CHESS images, a phantom composed of three tubes as in figure 4.2 was used.

A 2D axial MR T_2 weighted image of the phantom composed of the three 5 mm NMR tubes containing water, oil, and mixture of water and oil respectively is visible in figure

4.8. In the image, the three tubes are visible. CHESS images are shown in figure 4.8b and 4.8c for oil and water, respectively. As expected, for CHESS image of oil in figure 4.8b, only the tube containing oil was visible. The CHESS image of water recorded instead, two tubes were visible. The one containing only water, and the one containing water and oil. The presence of the latter is related to a phase separation between the oil and water within the tube, which causes to have no oil in the field of view imaged.

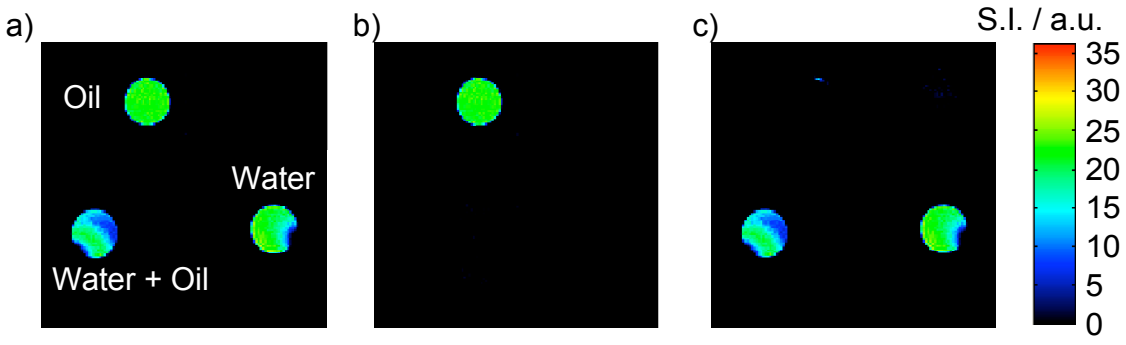


Figure 4.8 a) 2D axial T_2 weighted image of the phantom containing three 5 mm NRM tubes filled with water, oil, and a mixture of water-oil, and CHESS images acquired by selectively exciting b) the aliphatic protons of oil, and c) water protons.

4.3.4 NMR spectroscopy and MR CHESS imaging on sponge plugs filled with water and oil.

Figure 4.9 shows NMR spectra of water and a mixture of water and oil within sponge plugs. ^{1}H NMR spectrum of water in red, shows a broad peak (FWHM 2 ppm) cantered at 5.3 ppm. ^{1} H NMR spectra for the water and oil mixture in sponge, in blue, shows two peaks arising from water protons at 5.3 ppm, and from oil, which goes from 0 to 4.6 ppm, related to the aliphatic part of the oil. It is also important to highlight that the peak at 5.8 ppm observed for the oil in an NMR tube at 5.8 ppm, is not visible when oil

and water are mixed in a sponge because it is covered by the broadening of the water peak.

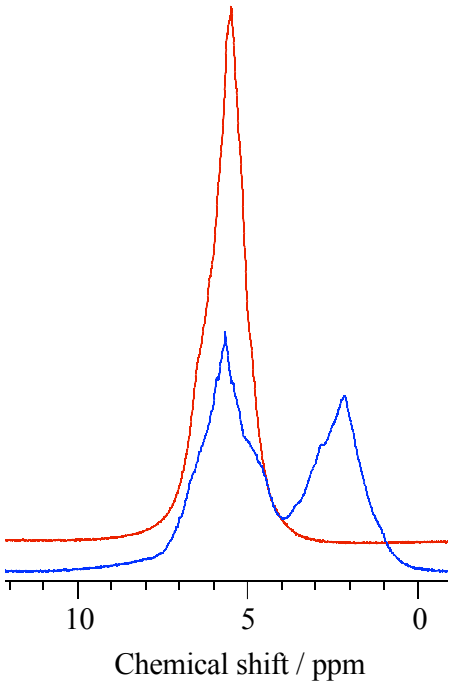


Figure 4.9 ^{1}H NMR spectra of water (red) and of a mixture of water and sunflower oil (blue) within sponge plugs.

A 2D axial T_2-weighted MR image, of the phantom composed of three sponge plugs filled with water, oil, and a mixture of water and oil can be seen in figure 4.10. In the image, all three sponges are visible.

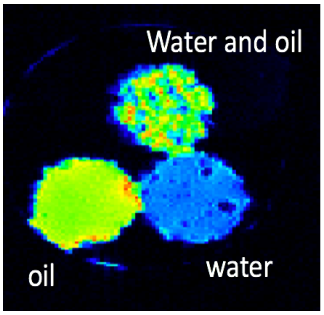


Figure 4.10 T_2 weighted image of the phantom containing three different sponge specimens soaked with water, oil, and a mixture of water and oil.

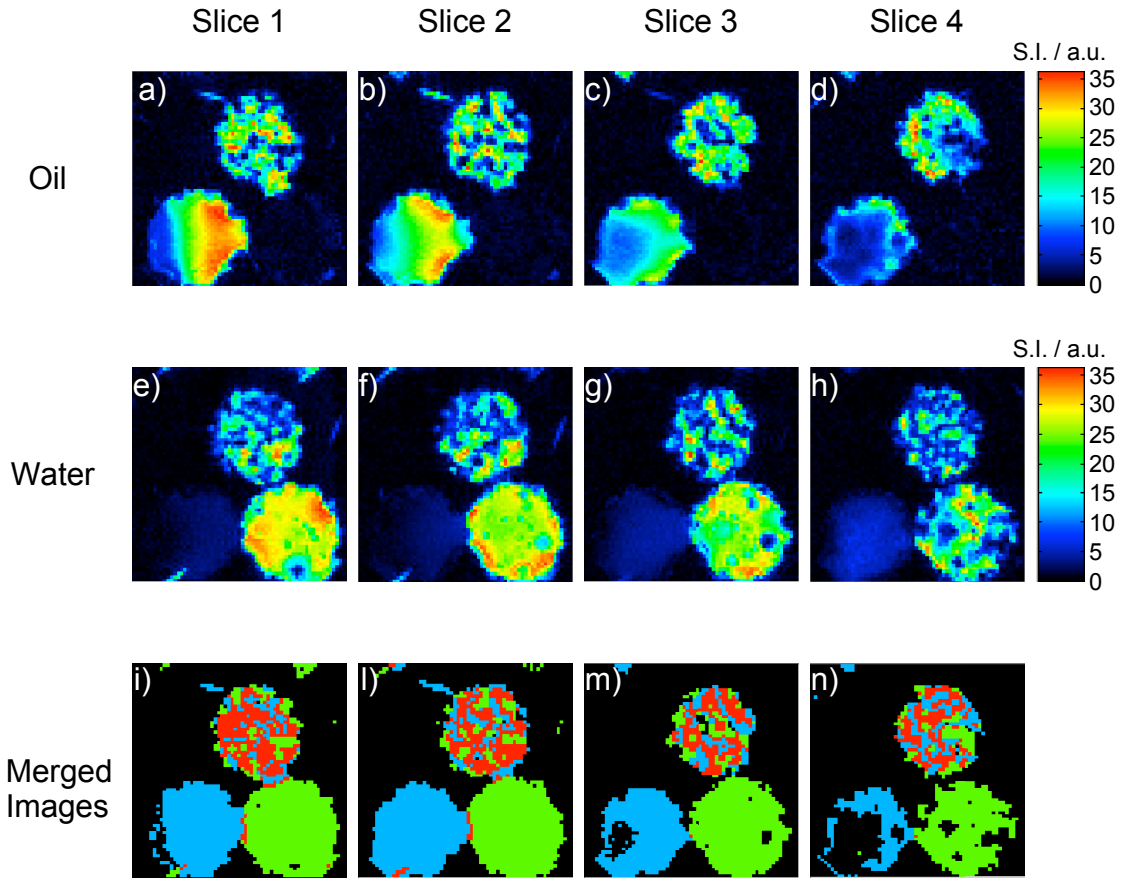


Figure 4.11 MR oil CHESS images (a-d), MR water CHESS images (e-h), and distribution maps of oil and water (i-n) within four slices of the phantom containing three different sponge specimens soaked with water, oil, and a mixture of water and oil. For the distribution map, the oil domains are represented in blue, the water domains in green, and the domains where both substances are present are represented in red.

In figure 4.10 a, b, c and d showing CHESS images produced by exciting the oil aliphatic protons, the oil distribution within four different slices of sponge plugs is visible. From the images, the oil distribution within the two plugs containing oil and a mixture of water and oil was visible, while no signal was detected for the sponge plug filled with water. Moreover, for the sponge plug filled only with oil, a decrease of signal intensity is noticeable comparing slice 1 to slice 4. This was related to the presence of an air bubble within the plug. CHESS images produced by exciting water protons show the water distribution within the two plugs filled with water and water and oil for the same slices. However, for all four slices, a weak signal coming from the plug filled with oil was also detected, making the plug containing only oil visible. This is probably due to the fact that upon exciting the water, the oil peak at 5.8 ppm beneath the water one was excited as well, giving rise to the weak oil signal. The oil and water CHESS images were merged together to generate distributions maps of oil and water within sponge plugs. The distributions maps for the four slices are visible in figure 4.10 i, l, m, and n. In these images, water and oil domains are visible, as well as regions where both substances are present. In figure 4.10 m and n, black regions are visible in both plugs containing water and oil, which are related to the presence of air bubbles.

4.4 Discussion

4.4.1 CLSM on sponge and biofilm in sponge

In this work, two different dyes have been used to try to visualize biofilms within sponges. Clean sponges have also been studied with CLSM without using contrast agents. Acridine orange is a fluorochrome that binds the nucleic acid of the bacteria and other cells within the biofilm. Calcofluor white instead, is a polysaccharide binding

dye, thus it stains the biofilm EPS. After the biofilm growth process, biofilm was clearly visible by eye within the sponge. However, despite the different binding nature of the two dyes, from a close inspection of the CLSM images in figure 4.2 a-e and 4.3 a-f, biofilms where not distinguishable from the sponge. From the images, it appears that both dyes are absorbed by the polymeric matrix of the sponge, making difficult to distinguish between the sponge structure and biofilms. From CLSM images in section 4.3.1 it can also be seen that clean sponges themselves give rise to fluorescence when excited with light at 405 nm and 488 nm. Both the autofluorescence of clean sponges and the difficulty to differentiate between the sponge structure and biofilms when the latter are present within the former, highlight the difficulty of using CLSM for biofilm visualization in sponge.

4.4.2 CHESS imaging of biofilm nutrients.

NMR spectroscopy on oil and water in 5 mm NMR tube has highlighted the presence of distinct proton resonances for oil and water that could be used to selectively excite the two substances. Chemically selective MR images of the phantom comprising three tubes, containing water, oil and a 50-50 mixture of oil and water, confirm it is possible to selectively image each fluid. For oil and water within the sponge, separate imaging of the two substances results a little more challenging, because of the broadening of the peaks corresponding to water protons and aliphatic protons of the oil. The broadening of both the water and oil peaks and the consequent loss of the fine structure is due to the presence of the sponge, which causes a reduction of the NMR relaxation times and therefore a loss of resolution. The widening of the water peak, caused the little peak at 5.8 correlated to oil, to be cover. This caused a weak oil signal

to be present when also for CHESS images of water acquired with an RF pulse centred on water resonance.

Differently to what happens in NMR tubes, where there is phase separation over time between water and oil, in sponge, the distribution maps generated for water and oil highlighted the presence of zones where the two substances are mixed. This is expected to happen within sponges because of surface properties of polyurethane and to the porous structure of the sponge. Polyurethane is a sticky hydrophobic material that causes the attachment of water molecules to its surface when in contact.[17] Oil instead interacts with the foam mainly by two mechanisms: capillary force with smaller pore, and void filling with larger pore.[17] The presence of large pores also allowed the water to be stored.[17] Thus, within a sponge soaked with oil and water it is expected to have areas where both liquids are present, which is confirmed by the CHESS merged images.

4.5 Conclusion

Understanding how biofilms growth within sponges is related with the food source viability is important to develop methodologies that can prevent biofilm from growing in these environments. The visualization of both biofilm and nutrients within sponges is thus fundamental to improve our understanding of the relationship between the two. In this chapter, we have tested confocal laser scanning microscopy and magnetic resonance imaging to visualize biofilm and food sources within a polyurethane sponge. Despite being one of the most used technique for biofilm visualization on surfaces, CLSM has proven to be challenging for biofilm visualization in polyurethane open-cell

foams. Irrespective of the characteristics of the dye used to stain biofilms, and the way it is applied, staining of the sponge structure also occurs. This makes it impossible to differentiate the biofilm from the sponge itself. Moreover, even in the absence of fluorescent dye, the sponge has shown autofluorescence, caused by the dye used to colour the sponge. Because of this, dyes with an excitation wavelength different from the sponge colorant excitation wavelength need to be selected, which reduces the quantity of dyes available for the analysis. Thus, alternative visualisation techniques are required to image biofilms in polyurethane open-cell foams, which is explored in chapter 5.

In this chapter, we have also investigated the use of chemically selective MRI to visualize food sources for bacteria, within polyurethane open-cell foams. The results confirmed the possibility to use MRI to selectively visualize in oil and water within porous media, and to understand how these are distributed in relation to the each other. This was possible even if the presence of the sponge causes a broadening of the NMR peak related to water and oil protons. This result open to the possibility to use MRI to directly visualize a correlation between food viability and biofilm development in porous media. Indeed, if associated with an MRI sequence that can turn on and off the contrast within biofilm (explored in chapter 5), MRI can give the possibility to separately visualize food and biofilm within the same sponge, without the necessity of using contrast agents or the requirements of pre-treatments like in SEM and TEM., and thus understand how food affect biofilm growth.

4.6 References

1 Austin, A. THe European flexible PU foam market report for 2018. *PU magazine* **16**, 206 (2018).

2 Chatterjee, S., Doshi, P. & Kumaraswamy, G. Capillary uptake in macroporous compressible sponges. *Soft Matter* **13**, 5731 (2017).

3 Shastry, A. *et al.* In-Situ High Resolution Dynamic X-ray Microtomographic Imaging of Olive Oil Removal in Kitchen Sponges by Squeezing and Rinsing. *Materials* **11**, 1482 (2018).

4 Ojima, M. *et al.* Hygiene measures considering actual distributions of microorganisms in Japanese households. *J. Appl. Microbiol.* **93**, 800 (2002).

5 Donofrio, R. S. *et al.* Are we aware of microbial hotspots in our household? *J. Environ. Health* **75**, 12 (2012).

6 Cardinale, M., Kaiser, D., Lueders, T., Schnell, S. & Egert, M. Microbiome analysis and confocal microscopy of used kitchen sponges reveal massive colonization by Acinetobacter, Moraxella and Chryseobacterium species. *Sci. Rep.* **7**, 1 (2017).

7 Vafai, K. *Porous media: applications in biological systems and biotechnology*. (CRC Press, 2010).

8 Woznica, A., Karcz, J., Nowak, A., Gmur, A. & Bernas, T. Spatial architecture of nitrifying bacteria biofilm immobilized on polyurethane foam in an automatic biodetector for water toxicity. *Microsc. Microanal.* **16**, 550 (2010).

9 Kim, J.-W., Choi, H. & Pachepsky, Y. A. Biofilm morphology as related to the porous media clogging. *Water Res.* **44**, 1193 (2010).

10 Yun, M.-A. *et al.* Characterization of biofilm structure and its effect on membrane permeability in MBR for dye wastewater treatment. *Water Res.* **40**, 45 (2006).

11 Ivankovic, T. *et al.* Development and evaluation of an experimental protocol for 3-D visualization and characterization of the structure of bacterial biofilms in porous media using laboratory X-ray tomography. *Biofouling* **32**, 1235 (2016).

12 Davit, Y. *et al.* Imaging biofilm in porous media using X-ray computed microtomography. *J. Microsc.* **242**, 15 (2011).

13 Britton, M. M. Porous Media Studied by MRI. *eMagRes*, doi:10.1002/9780470034590.emrstm1263 (2011).

14 Lakshmanan, S., Maru, W. A., Holland, D. J., Mantle, M. D. & Sederman, A. J. Measurement of an oil–water flow using magnetic resonance imaging. *Flow Meas. Instrum.* **53**, 161 (2017).

15 Chang, C. P., Watson, A. T. & Edwards, C. M. in *Experimental Methods in the Physical Sciences* Vol. 35 387 (Elsevier, 1999).

16 Haktanir, I., Masoura, M., Mantzouridou, F. T. & Gkatzionis, K. Mechanism of antimicrobial activity of honeybee (Apis mellifera) venom on Gram-negative bacteria: Escherichia coli and Pseudomonas spp. *AMB Express* **11**, 54, doi:10.1186/s13568-021-01214-8 (2021).

17 Pinto, J., Athanassiou, A. & Fragouli, D. Surface modification of polymeric foams for oil spills remediation. *J. Environ. Manage.* **206**, 872 (2018).

5 BIOFILM MIMIC MATERIAL

5.1 Introduction

Biofilm visualization is extremely important for the understanding of biofilm properties. Different techniques have been developed to directly visualize biofilms formation and its exopolysaccharide (EPS) matrix.[1-4] Among these, the most used are electron microscopy,[2] confocal laser scanning microscopy (CLSM) and magnetic resonance imaging (MRI).[4] All of these techniques have their advantages and disadvantages in studying biofilm, as described in section 1.2.5. Scanning electron microscopy (SEM) and transmission electron microscopy (TEM) have the advantage of providing near-nanometer resolution, allowing the visualization of features which are impossible to image with other techniques.[5] However, pre-treatments are required for both of these techniques, such as fixation, drying and coating with conductive materials, which can cause the alteration of the biofilm structure.[6-8] Alternatives techniques can be used to reduce pre-treatments such as environmental SEM (ESEM), which allows the preservation of the matrix but requires the presence of metals ions within the biofilm to obtain contrast.[9] However, the non-homogeneous distribution of metal ions within biofilms can cause great variation in image intensity across the sample. Moreover, ESEM is limited to the visualization of biofilm growing in the presence of metals.[6]

CLSM has the advantage of imaging biofilm under fully hydrated conditions and the possibility of studying the physical and chemical relationship which exists between different biofilm components, such as bacteria and EPS,.[3] However, in order to perform CLSM on biofilms, fluorescents dyes need to be used, which can have a negative

impact on cellular metabolism.[10] Moreover, as demonstrated in chapter 4, the presence of absorbing porous materials, such as polyurethane sponges, dyes can also stain the porous matrix, making it difficult to distinguish between the matrix itself and the biofilm.

Unlike these other techniques, MRI offers the possibility to image biofilms, without the need for contrast agents, by observing changes in the NMR signal for water within.[4] MRI relaxation time and diffusion images have been used to visualize biofilms,[11,12] thanks to the confinement of liquids in biofilm. This reduces the mobility of liquids which causes the reduction of both T_1 and T_2 relaxation times, and diffusion. This reduction in relaxation time or self-diffusion co-efficient can be used to generate contrast between biofilms and their external environment, allowing their visualization.[13,14] However, the MR relaxation times of water can also change as a result of the porous media matrix itself and its pore size. As a consequence, when biofilms are present within a foam, it becomes difficult to associate a variation in T_2 relaxation time to the presence of the biofilm or the presence and characteristics of the foam matrix. This makes biofilm visualization challenging, in these media, through T_2 relaxation contrast.[11] To bypass this problem, MRI contrast agents, such as Cu^{2+} and La^{3+}, can be flushed through the system in order to stain the biofilm and induce an increased T_2 relaxation time reduction, which enhances the contrast between biofilm and matrix.[15] However, contrast agents flushed through the foam, are trapped within the matrix of the foam, causing stain of the latter. To remove the metal ions trapped within the foam, further flushes of the system with deionized water need to be flushed within the system. To ensure that metals are removed from the foam, multiple imaging acquisition are

necessary after every flush of the system with deionised water, which causes long experimental times. Moreover, as described in section 1.3.2, metals can be toxic to bacteria and thus can cause variation in biofilm formation and structure.[16]

In this chapter, chemical exchange saturation transfer (CEST) MRI is tested on a biofilm mimic material. CEST enables the visualization of the location of target molecules with exchangeable protons.[17,18] This is achieved by the exchange of protons between the target molecule and bulk water protons, whose spins population has been saturated. This causes a reduction of signal intensity in that region, which can be used as contrast., enabling the localization of this molecules of interests[18] Thus, images can be obtained without the need for an additional contrast agent. Moreover, CEST offers the possibility to turn the contrast on and off in a controllable fashion, making it easier to observes than T_2 contrast, with is always present. It allows you then to be more discerning on the origins of signal variation. To test the possibility of using CEST MRI to image biofilms, sodium alginate was selected as a material to mimic the biofilm EPS. Alginate was chosen because it is found in the EPS for a range of different biofilms, such as *P*. *aeruginosa* and *P. fluorescens.*[19] Alginates are naturally-occurring polysaccharides composed of a linear block copolymer containing (1-4) linked *b-D-mannuronic* and *a-L-guluronic acid,* and possess different exchangeable protons, which are required to perform CEST.

5.2 Materials and methods

5.2.1 Sample preparation

5.2.1.1 Solutions preparation

Sodium alginate solutions were prepared using Protonal 20/40 sodium alginate (FMC biopolymer), which comprises > 60% guluronic acid. Sodium alginate was dissolved under stirring, for five minutes, in de-ionised water at 60°C, at a concentration of 2% w/w. Once all the sodium alginate was dissolved, the solutions were transferred into 5 mm NMR tubes. A solution of $CaCl_2$ 0.2 M was also prepared by dissolving $CaCl_2$ (SLS) in distilled water.

5.2.1.2 Sodium alginate beads

Alginate beads were prepared from Protonal 20/40 sodium alginate (FMC biopolymer). 2% w/w Protonal 20/40 alginate solution was prepared as described in section 5.2.1.1. Once prepared, the alginate solution was dropped into $CaCl_2$ (SLS) 0.2 M solution using a Pasteur pipette to form the beads. The beads were left to rest for 48 h in order to stabilize the system. For MRI measurements, sodium alginate beads with $CaCl_2$ solution were transferred in a 5 mm NMR tube.

5.2.1.3 $CaCl_2$ and Sodium alginate gel in sponge

Cylindrical plugs, of diameter 4 mm and height 40 mm, were extracted from a single polyurethane sponge (Spontex, Colombes, France, batch n° = 7124813) using a 4 mm corkborer (Fisher scientific UK Ltd,). Plugs were saturated with $CaCl_2$ solution. Air bubbles were removed by submerging plugs under the $CaCl_2$ solution and placing it under vacuum for 1h. For alginate gel formation within plugs containing $CaCl_2$, 2 %

w/w sodium alginate solution was injected using a syringe with needle, after air bubble removal, within some sponge plugs. Both sponge plugs containing $CaCl_2$ solution, and $CaCl_2$ solution plus alginate gel, were inserted in two separated 5 mm NMR tube. To avoid air bubbles entering the sponge during its insertion within the NMR tube, the insertion was performed while keeping the plugs and the tubes within $CaCl_2$ solution.

5.2.2 MRI CEST and T_2 map experiments

Magnetic resonance imaging data were collected on a Bruker Avance III HD spectrometer, equipped with a 7 T vertical wide-bore superconducting magnet, operating at a proton resonance frequency of 300.13 MHz. All experiments were recorded using a micro2.5 imaging probe at 293 ± 0.3°K. which was maintained by the temperature of water-cooled gradient coils (WB40). ^{1}H MR images were collected using a quadrature ^{1}H 25 mm radio frequency (RF) birdcage coil. T_2 relaxation time maps, of alginate gel, alginate beads and sponge plug containing alginate gel, were acquired using the spin echo imaging sequence RARE (Rapid Acquisition with Relaxation Enhancement). Images were recorded using a 1 mm slice thickness and a 64 × 64 pixel matrix, with a field of view of 10 × 10 mm. T_2 MR relaxation maps were produced from 8 echo images, with a RARE factor of 8, echo time of 4 ms and repetition time of 5 s.

CEST was performed on sodium by acquiring axial (horizontal) two-dimensional images using a RARECEST sequence. For the alginate solution in a 5 mm NMR tube, CEST images were recorded using a 1 mm slice thickness and a 64 × 64-pixel matrix, with a field of view of 10 × 10 mm. A RARE factor of 8 was used, with an echo time of

2.5 ms and a repetition time of 1 s. For the alginate bead CEST images, a rare factor of 1 and repetition time of 5 s was used. CEST images of alginate gel in sponge were recorded using the same parameters used for alginate beads. For all the CEST experiments, a single Gaussian pulse was used for pre-saturation irradiation. The pulse had a duration of 27.4 ms, with a bandwidth of 100 Hz. A flip angle of 120□ was used. For the alginate solution and the alginate bead, the frequency offsets for the pre-saturation irradiation were varied from 6 to 4 ppm (1800 Hz – 1200 Hz), with a step size of 0.050 ppm, resulting in 41 images for each experiment. For the alginate gel in sponge, the frequency offsets for the pre-saturation irradiation were varied from 7 to 3 ppm (2100 Hz – 900 Hz), with a step size of 0.050 ppm, resulting in 81 images recorder.

5.2.3 CEST Data analysis

CEST data was imported in MATLAB as a 3D ascii matrix. MATLAB was used to correct the $\boldsymbol{B}_0$ inhomogeneity within the images and to correct the intrinsic frequency shift of the RARECEST sequence. The MATLAB code used can be found in the supplementary information. The correction process is outlined in figure 5.2. MTR_{asym} plot was produced using equation 2.9.

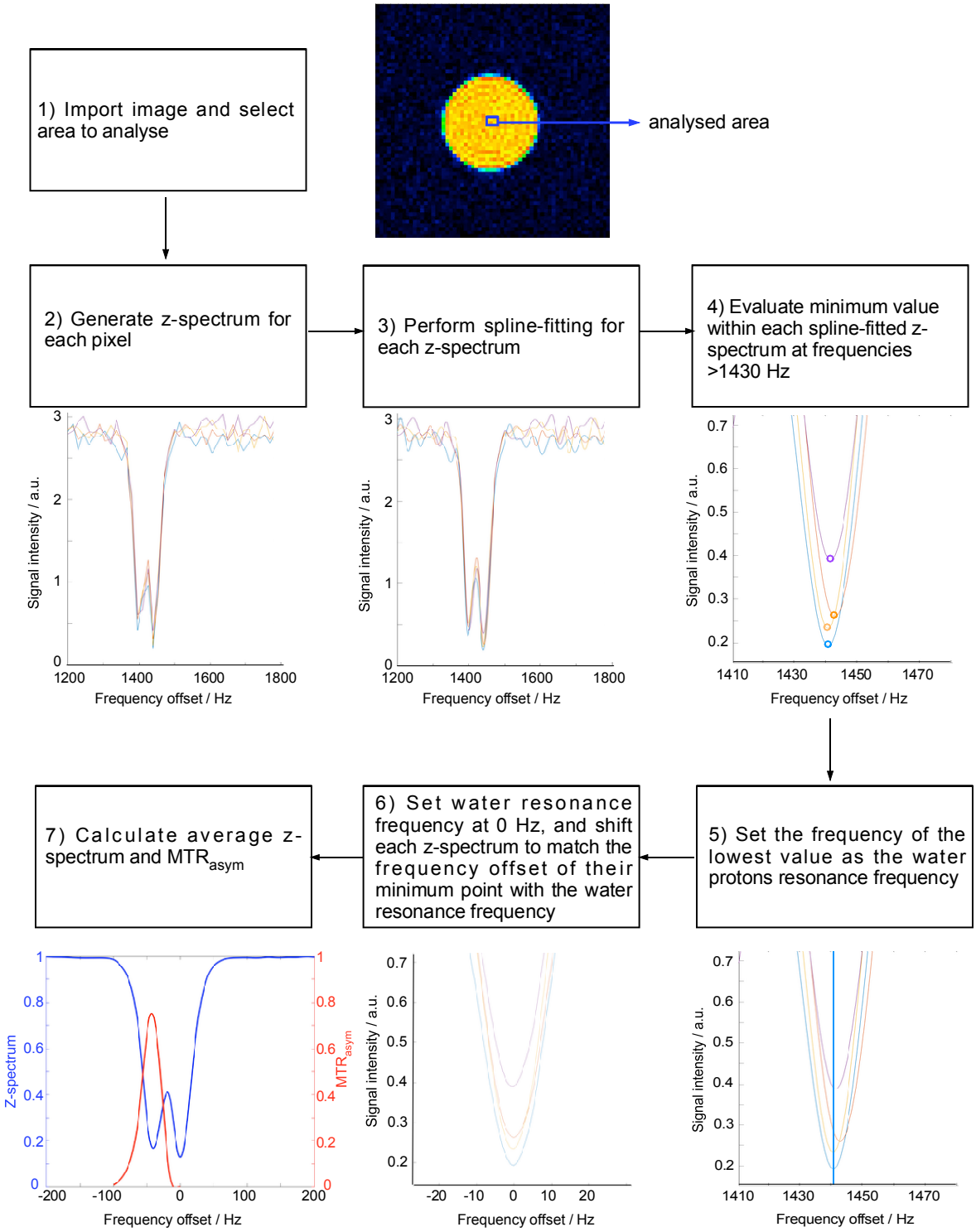


Figure 5.1 Flow chart showing the steps performed to correct the $\boldsymbol{B_0}$ *inhomogeneities within CEST images and to evaluate the Z-spectrum and* MTR_{asym}.

5.3 Results

5.3.1 Alginate solution

Figure 5.2 shows the MR T_2 relaxation time map for 2 % w/w sodium alginate solution in a 5 mm NMR tube. The T_2 relaxation map shows the solution is homogeneous, with an average T_2 = 127 ms ± 14 ms .

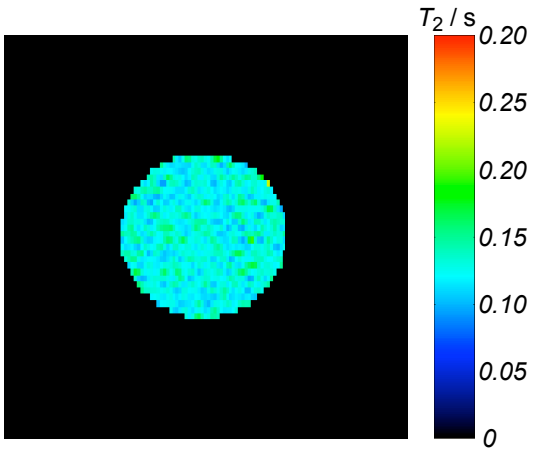


Figure 5.2 2D axial ^1H MR T_2 relaxation map of water for 2 % w/w sodium alginate solution in a 5 mm NMR tube.

A section of the CEST MRI are displayed in figure 5.3. A uniform signal intensity is visible for images acquired between 1680 Hz and 1500 Hz (figure 5.3 a-m). At 1485 Hz (figure 5.3 n), the signal intensity of the solution starts to decrease, reaching its minimum at 1440 Hz (figure 5.3s). A slight increase in intensity is visible at 1425 Hz (figure 5.3r), followed by a further decrease in intensity (figure 5.3s, 5.3t) and subsequent increase from 1380 Hz (figure 5.3u), to reach values of intensity similar to the one in the first images (figure5.3 v-x).

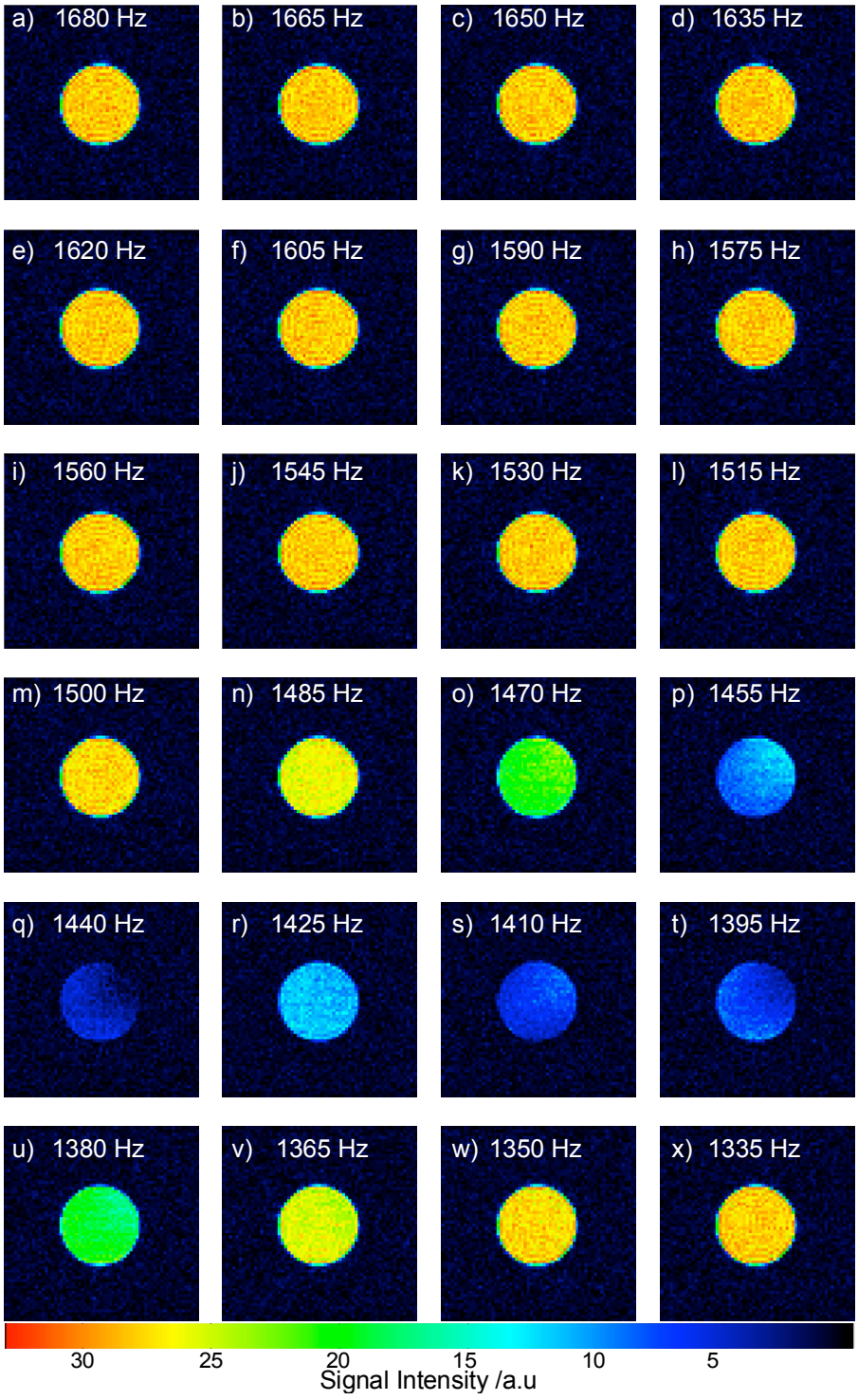


Figure 5.3 A selection of 2D axial MRI CEST images, displayed at an interval of 15 Hz, acquired for 2 % w/w sodium alginate solution in a 5 mm NMR tube. The images displayed cover the range of frequency offset between 1680 Hz and 1335 Hz.

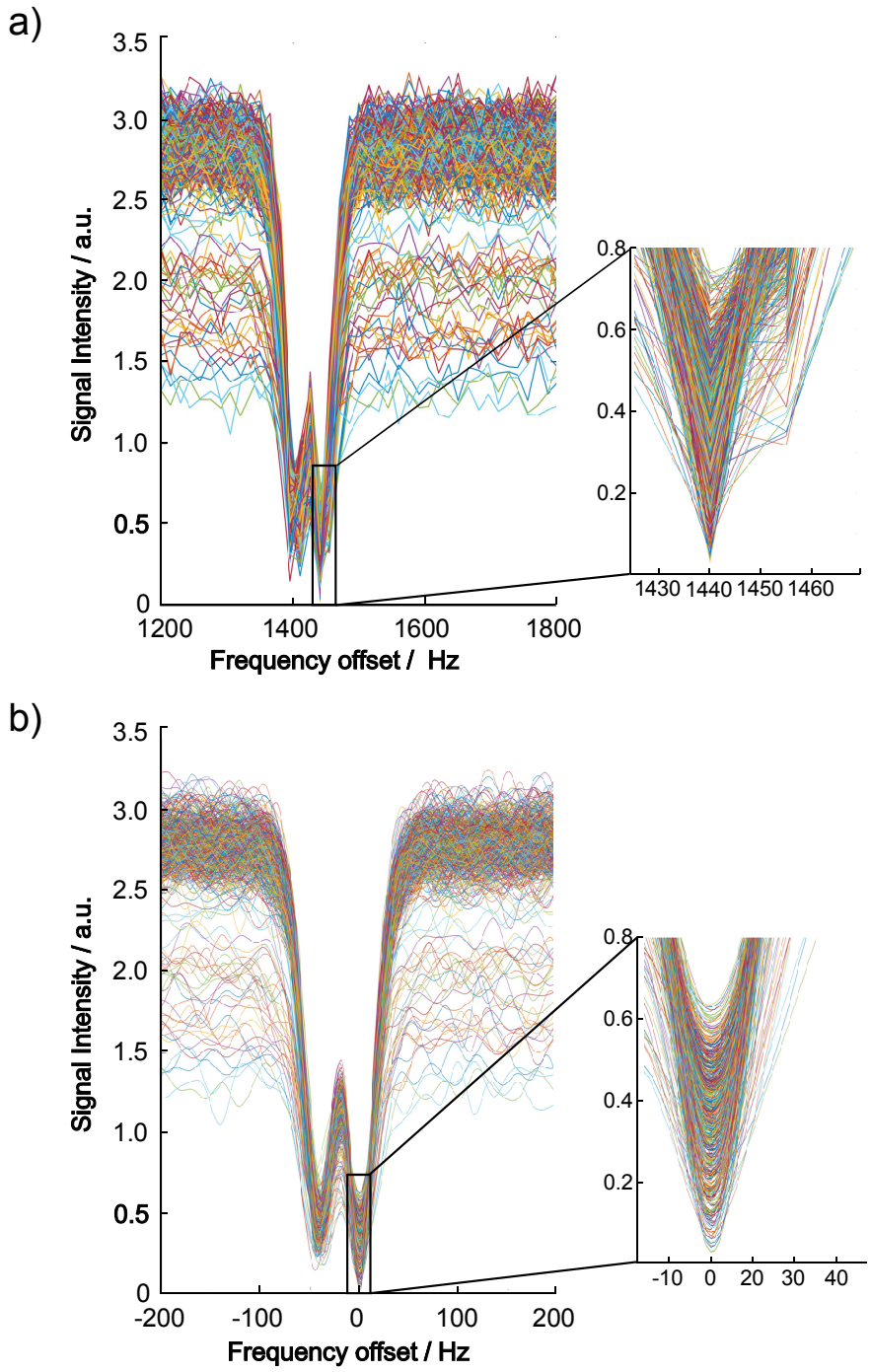


Figure 5.4 a) Z-spectrum and b) corrected spline-fitted z-spectrum, evaluated from each pixel of the 41 CEST images of the 2 % w/w alginate solution in a 5 mm NMR tube.

Z-spectra for each pixel of the sodium alginate solution, evaluated from the CEST images, are visible in figure 5.4a. For each pixel, the presence of two peaks is visible, one between 1440 Hz and 1455 Hz, corresponding to the signal intensity at the water frequency resonance, and one between 1395 Hz and 1410 Hz, corresponding to the signal intensity at the frequency resonance of exchangeable protons within sodium alginate. Figure 5.4b displays the corrected spline-fitted z-spectra for each pixel, where spectra have been shifted to have the water frequency resonance for each pixel at 0 Hz. From the data in figure 5.4b, the average z-spectrum has been evaluated, which is shown in figure 5.5 along with the MTR_{asym}.

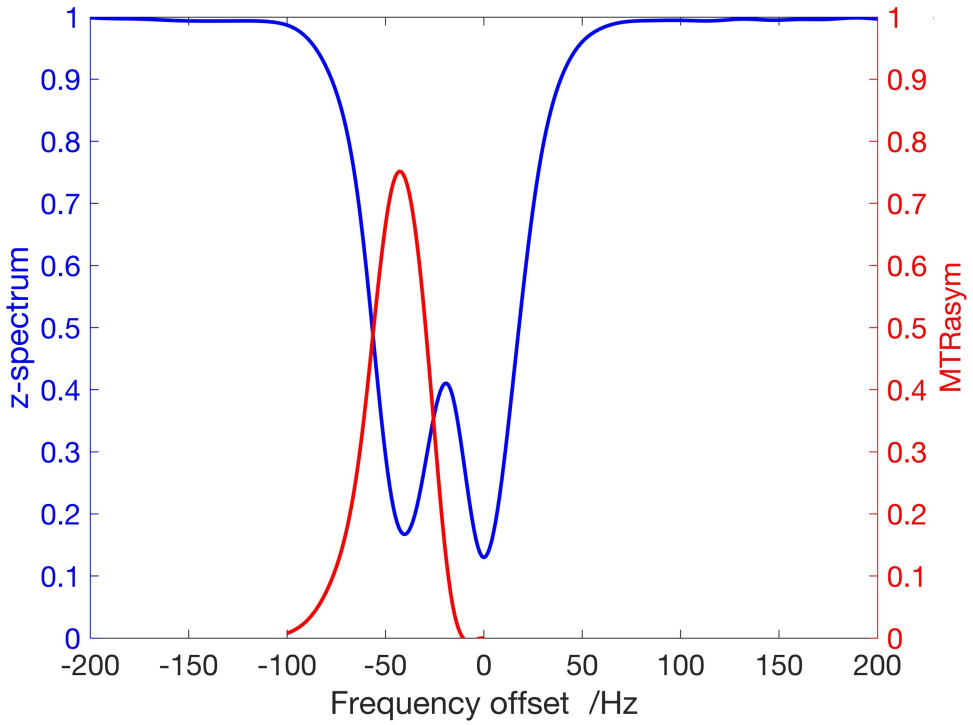


Figure 5.5 Plot of the Average z-spectrum and MTR_{asym} for 2 % w/w sodium alginate solution as a function of frequency offset.

In Figure 5.5, the average z-spectrum shows a peak at – 44 Hz, which corresponds to the CEST peak. The MTR_{asym}, which is used to quantify the CEST effect, shows a peak at – 44 Hz with a maximum value of 0.75.

5.3.2 Alginate gel beads

The T_2 relaxation map evaluated for the alginate bead in 0.2 M $CaCl_2$ solution within a 5 mm NMR tube is visible in figure 5.6.

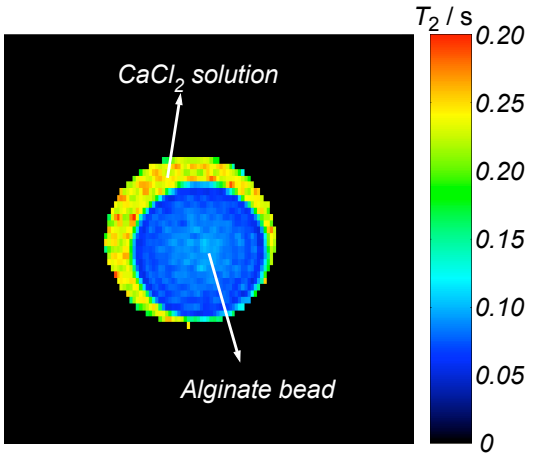


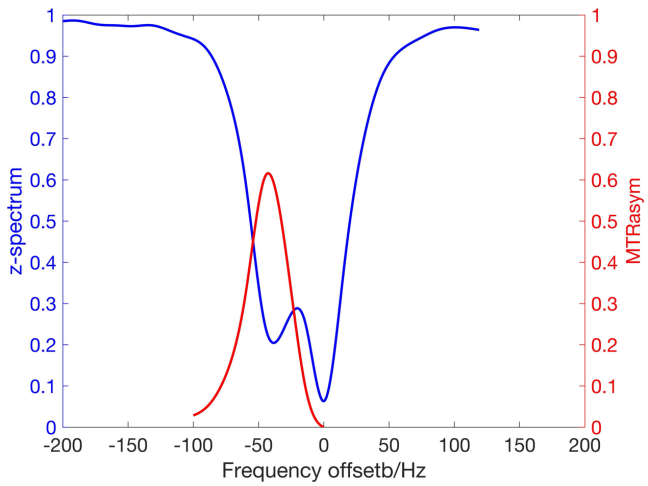
Figure 5.6 2D axial ^1H MR T_2 relaxation map of 2 % w/w alginate gel beads in 0.2 M $CaCl_2$ solution within a 5 mm NMR tube.

From Figure 5.6, the alginate gel bead is clearly distinguishable from the surrounding $CaCl_2$ solution, because of a different T_2 relaxation time between the two. In particular, an average T_2 = 90 ms ± 5.5 ms and T_2 = 237 ms ± 12 ms were measured for the alginate gel bead and for the surrounding solution, respectively.

Average z-spectra for alginate gel bead and the surrounding solution evaluated from CEST experiments, are visible in figure 5.7. In particular, figure 5.7a displays the z-spectrum for the alginate gel bead, while figure 5.7b shows the z-spectrum for the $CaCl_2$ solution surrounding the bead. Both z-spectra show two peaks: one at 0 Hz,

related to the suppression of water signal, and one at – 44 Hz, related to the CEST effect. However, the z-spectrum for $CaCl_2$ solution surrounding the alginate beads shows a deeper CEST peak compared to the one of the alginate gel bead. This difference is reflected in the MTR_{asym}, which displays a value of 0.82 and 0.61 for the $CaCl_2$ solution and the alginate gel bead, respectively. Considering $CaCl_2$ does not have exchangeable protons, the presence of a CEST peak within the $CaCl_2$ solution suggests the presence of alginate residues within it.

a)



b)

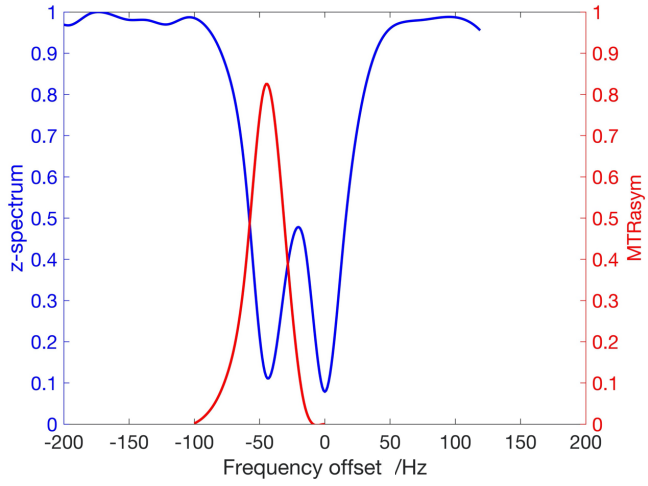


Figure 5.7 Averaged z-spectrum for a) alginate gel bead, and b) 0.2 M $CaCl_2$ solution surrounding the bead, within a 5 mm NMR tube.

A spin-density image of the tube containing the alginate beads and the $CaCl_2$ solution is shown in figure 5.8a. From the image 5.8a, no difference in intensity is visible between the bead and the solution. Figure 5.8b displays the CEST map of the system studied, where the percentage CEST effect for each pixel of the image is observable. In the CEST map (figure 5.8b), the bead is now distinguishable, from the surrounding $CaCl_2$ solution, because of the lower value of MTR_{asym}, for the bead compared to the solution.

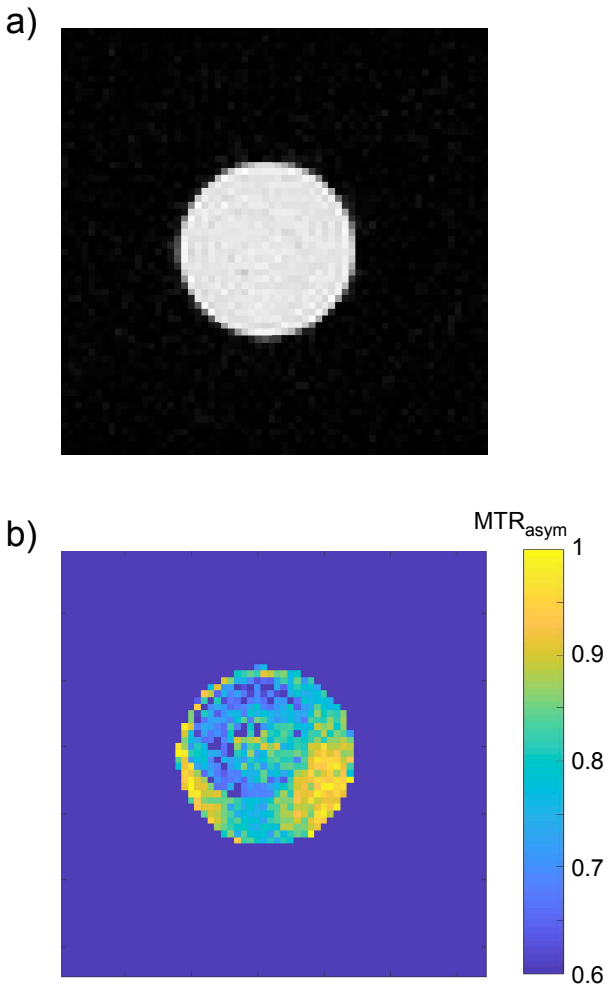


Figure 5.8 a) Axial MR spin density image and b) CEST map of the alginate gel bead in 0.2 M CaCl2 within a 5 mm NMR tube.

5.3.2 $CaCl_2$ solution in sponge

The average z-spectrum evaluated for 0.2 M $CaCl_2$ solution, within a sponge plug, is shown in figure 5.9. The z-spectrum shows only one peak at 0 Hz, related to water signal suppression. No CEST effect is visible, which is confirmed by the absence of any MTR_{asym} peak.

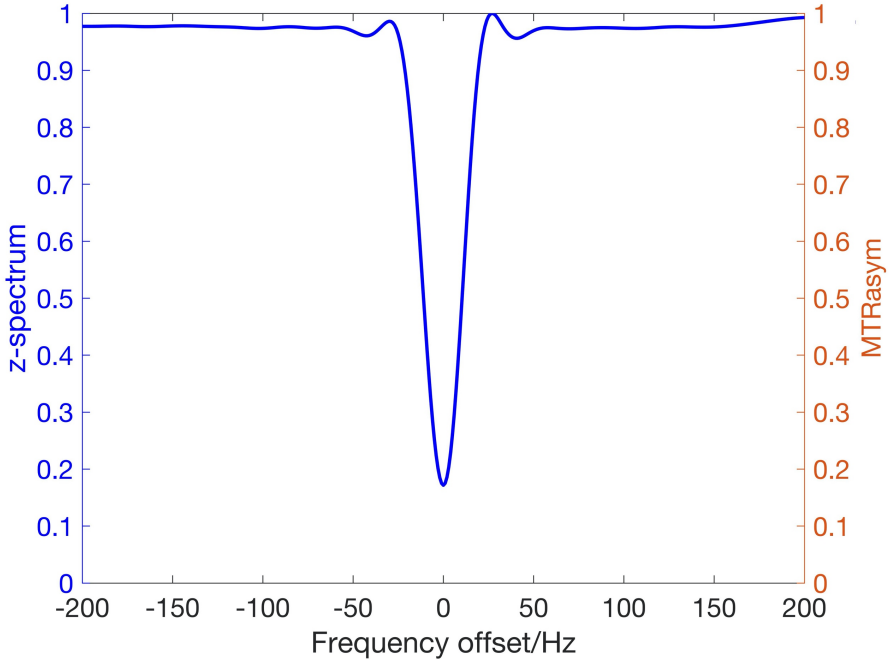


Figure 5.9 Averaged z-spectrum for water in a 0.2 M $CaCl_2$ solution within a sponge plug.

5.3.3 Alginate Gel in sponge

Figure 5.10 shows a MR T_2 relaxation time map of alginate in a sponge saturated with $CaCl_2$ solution. On the left side of the image, two blue filaments are visible with an average T_2 = 110 ms ± 12 ms which were associated with alginate gel. For the $CaCl_2$ solution within the sponge, which surrounds the two blue filaments, an average T_2 = 256 ms ± 24 ms was measured.

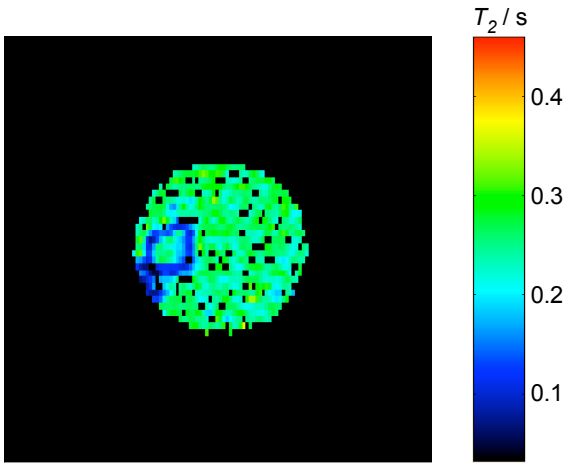


Figure 5.10 2D axial ^{1}H MR T_2 relaxation map of sponge filled with 0.2 M $CaCl_2$ solution, following injection of sodium alginate. Alginate gel is formed with a T_2 = 110 ms ± 12 ms and appears blue. The surrounding liquid has a T_2 = 256 ms ± 24 ms and appears green. This solution is predominately 0.2 M $CaCl_2$ but also contains residual sodium alginate. The black pixels in the sponge are regions with low signal intensity.

Z-spectra and MRT_{asym} were evaluated and are shown in figure 5.11. Once again, both z-spectra for the alginate gel and the $CaCl_2$ within the sponge possess two peaks. For both alginate gel and $CaCl_2$ z-spectra, the peak at 0 Hz is associated with suppression of the water signal. Instead, the peak at – 47 Hz present in the z-spectra of alginate gel (figure 5.8a), and the peak – 50 Hz present in the z-spectrum of the $CaCl_2$ surrounding the gel (figure 5.8b), are related to the CEST effect. For both the alginate gel and $CaCl_2$ solution, the CEST effect is confirmed by the MTR_{asym} analysis, which shows for both alginate gel and $CaCl_2$ solution a peak at – 47 Hz and – 50 Hz, respectively. However, MTR_{asym} analysis results differ to those observed in a 5 mm NMR tube, where the MTR_{asym} values observed for the bead and the solution surrounding were different. Indeed, for the alginate gel and $CaCl_2$ solution within

sponge show really similar maximum values (0.75 and 0.77 respectively). The presence of CEST effect for the $CaCl_2$ solution within this sample CEST suggest the presence of alginate residues within it

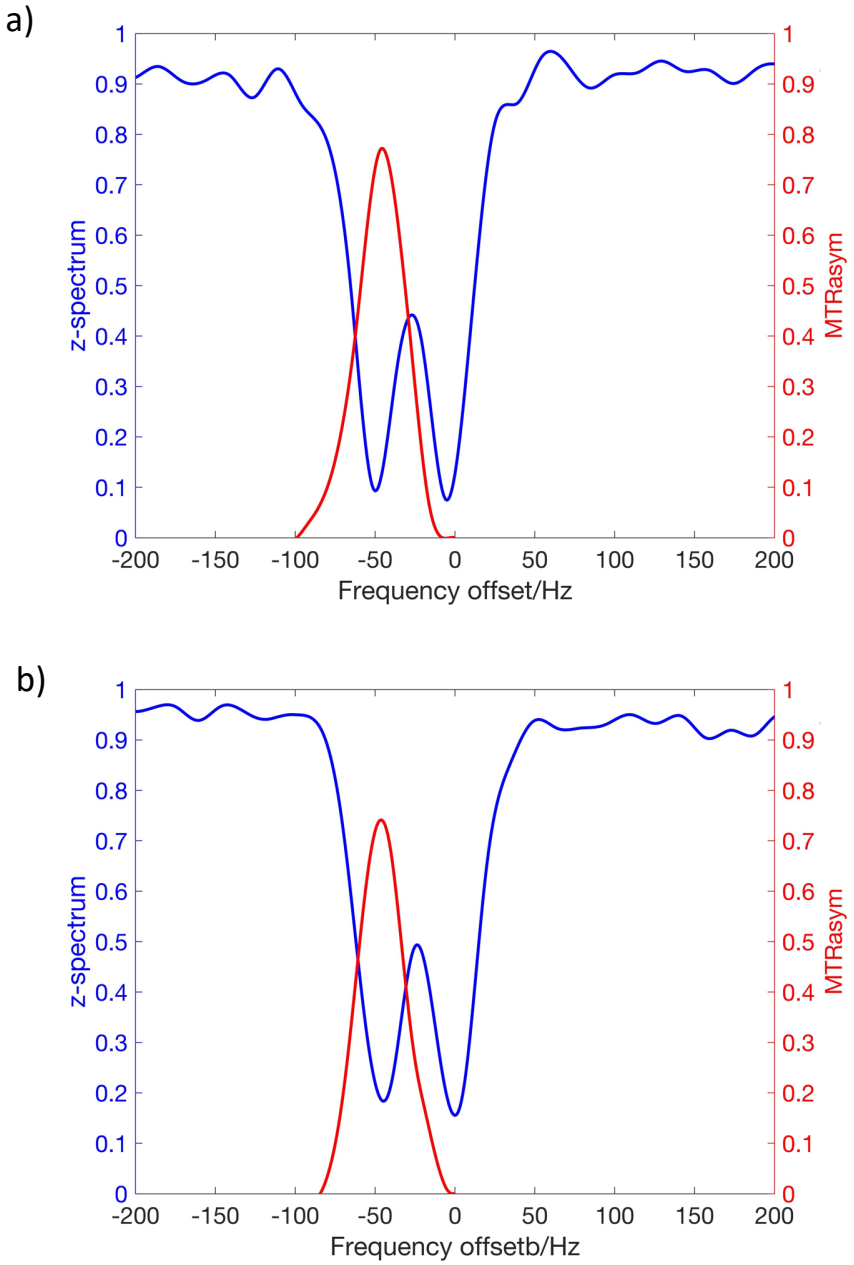


Figure 5.11 Averaged z-spectrum evaluated from CEST images of alginate gel in a sponge saturated with CaCl2 solution for a) alginate gel calculated from pixels range [46:50,28:29], and b) 0.2 M CaCl2 solution within a 4 mm diameter sponge plug, calculated from pixels range [31:37,29:38].

5.4 Discussion

Alginate gel beads were tested to better mimic the hydrogel-like structure of the EPS of biofilms. The average z-spectrum and MTR_{asym} value observed for sodium alginate in $CaCl_2$ solution, have highlighted the presence of a CEST effect at – 44 Hz, related to exchanging protons between sodium alginate and water. The z-spectrum of $CaCl_2$ solution in sponge (figure 5.9), does not show a CEST effect, which confirms that the CEST effect observed for sodium alginate in $CaCl_2$ solution sample is related to the alginate.

As for sodium alginate, alginate gel bead has also shown a CEST peak at – 44 Hz. However, the efficiency of the CEST effect, measured by MTR_{asym}, resulted in a 14% decrease for the alginate gel bead compared to the alginate solution. This reduction could be related to a decrease in the number of exchangeable protons available within alginate gel. Indeed, in the formation of the alginate gel, there is an exchange between proton and calcium ions, generating a cross-link in adjacent G residues chains,[20] and reducing the number of exchangeable protons available. A CEST effect has also been observed for the $CaCl_2$ solution surrounding the bead. However, the z-spectrum of pure $CaCl_2$ solution in sponge does not show CEST peaks, as shown in figure 5.9. Hence, the presence of a CEST peak for the $CaCl_2$ solution surrounding the bead suggests the presence of sodium alginate within the solution. The presence of free alginate, within the $CaCl_2$ solution, could be explained by leaching of alginate from the gel to the $CalC_2$ solution, during gelation. Thus, it is possible that $CaCl_2$ solution contains alginate residues that have not participated in the gelation process. This also

explains the presence of a CEST peak for $CaCl_2$ solution surrounding the alginate gel in the sponge (figure 5.8b).

The presence of a CEST effect for the both alginate gel and the surrounding solution could cause problem in the generation of a contrast between the two. Fortunately, alginate gel bead and the solution surrounding it shows different MTR_{asym} values between them. This different in MTR_{asym} can be used to generate a CEST contrast between the two, as exploited by the CEST map in figure 5.8b. However, this was not the case for alginate gel in sponge. Indeed, the alginate gel within the sponge showed a MTR_{asym} value (0.74) higher than the one observed for the alginate gel bead (0.61). The MTR_{asym} value of alginate in sponge was similar to the MTR_{asym} of the solution within the sponge (0.77), which did not allow the generation of a proper contrast between the gel and the solution. The difference in MTR_{asym} values observed in alginate gel bead and alginate gel in sponge is related to the preparation process of the alginate gels, which led to a variation in the composition of the gel. Indeed, alginate gel beads have been left to mature in the 0.2 M $CaCl_2$ solution for 48 h before CEST experiments. For CEST experiments on alginate gel in sponges instead, images were acquired within 1 h of the injection of sodium alginate within the sponge saturated with $CaCl_2$. Considering that the degree of crosslinking between alginate and calcium increases with time,[21] the higher CEST efficiency for alginate gel in sponge can be attributed to a lower degree of crosslinking, and thus to a higher number of exchangeable protons if compared to alginate beads. The difference in the degree of crosslinking between the two sample is confirmed by observing the T_2 relaxation time values for the samples studied. 2% w/w sodium alginate solution displayed a T_2 value

of 127 ms ± 14 ms, while the alginate gel bead, after 48 h maturation, displayed a T_2 value of 90 ms ± 5 ms. Alginate gel within the sponge instead showed a T_2 value of 110 ms ± 112 ms, which is in between the results observed for the alginate solution and the alginate gel bead. This suggests that the gelation process of the alginate gel within the sponge was still ongoing when CEST measurements were performed. Thus, a higher number of exchangeable protons were available for alginate gel within the sponge compared to the alginate gel bead, which resulted in a higher CEST effect in the former.

5.5 Conclusions

This chapter has demonstrated the viability of CEST for probing biofilms. A CEST effect has been observed for a biofilm mimic material, sodium alginate, in different environments (solution, gel beads, and gel within a sponge). The CEST observed for alginate gel in sponge, confirms that CEST effect is insensible to the presence of the sponge, and thus could be used for imaging biofilms within a sponge.

The possibility of using CEST to generate a proper contrast between alginate gels and its surroundings has been demonstrated for alginate gel beads. This result confirms the possibility of using CEST to produce images of alginate gel without any contrast agents. Unfortunately, this cannot be confirmed for alginate gel in sponge. Indeed, a non-complete gelification process of the Ca-alginate gel, and the presence of alginate in $CaCl_2$ solution saturating the sponge, do not allow the generation of a proper CEST contrast. However, the fact that a CEST effect can be detected for alginate within sponge, and the results produced for alginate gel beads, suggest that, with the right

sample preparation, a CEST contrast can also be produced for alginate gel within sponges.

We believe that the results displayed in this chapter for a biofilm mimic material show the potential of MRI CEST sequence to be applied for the visualization of real biofilms, in different environments, without the application of contrast agents or the need of any pre-treatments. It is important to notice that, while our results show that MRI CEST can be used to visualize the presence of biofilm in porous media, this will hardly be able to differentiates biofilm's morphologies, e.g. patches or streamers. Indeed, as described in paragraph 1.2.4, single patches and streamers have dimensions which are < 100 μm, thus lower than MRI resolution. To fully assess the potentiality of MRI CEST for biofilm imaging, further studies need to be performed. CEST experiments need to be performed on alginate gel in sponge with longer gel maturation time, to assure contrast can be produced also in sponges. Moreover, CEST imaging need to be tested on real biofilms in sponges, which requires the development of new procedures to grow biofilm within a sponge.

5.6 References

1 Costerton, J. W., Stewart, P. S. & Greenberg, E. P. Bacterial biofilms: a common cause of persistent infections. *Science* **284**, 1318 (1999).

2 Walker, J. T., Verran, J., Boyd, R. D. & Percival, S. in *Methods Enzymol.* Vol. 337 243 (Elsevier, 2001).

3 de Beer, D. & Stoodley, P. Relation between the structure of an aerobic biofilm and transport phenomena. *Water Sci. Technol.* **32**, 11 (1995).

4 Neu, T. R. *et al.* Advanced imaging techniques for assessment of structure, composition and function in biofilm systems. *FEMS Microbiol. Ecol.* **72**, 1 (2010).

5 Lawrence, J. *et al.* Scanning transmission X-ray, laser scanning, and transmission electron microscopy mapping of the exopolymeric matrix of microbial biofilms. *Appl. Environ. Microbiol.* **69**, 5543 (2003).

6 Priester, J. H. *et al.* Enhanced visualization of microbial biofilms by staining and environmental scanning electron microscopy. *J. Microbiol. Methods* **68**, 577 (2007).

7 Kachlany, S. C. *et al.* Structure and carbohydrate analysis of the exopolysaccharide capsule of Pseudomonas putida G7. *Environ. Microbiol.* **3**, 774 (2001).

8 Fassel, T. A. & Edmiston Jr, C. E. in *Methods Enzymol.* Vol. 310 194 (Elsevier, 1999).

9 Darkin, M., Gilpin, C., Williams, J. & Sangha, C. Direct wet surface imaging of an anaerobic biofilm by environmental scanning electron microscopy: application to landfill clay liner barriers. *Scanning* **23**, 346 (2001).

10 Ullrich, S., Karrasch, B., Hoppe, H., Jeskulke, K. & Mehrens, M. Toxic effects on bacterial metabolism of the redox dye 5-cyano-2, 3-ditolyl tetrazolium chloride. *Appl. Environ. Microbiol.* **62**, 4587 (1996).

11 Hoskins, B. C., Fevang, L., Majors, P. D., Sharma, M. M. & Georgiou, G. Selective imaging of biofilms in porous media by NMR relaxation. *J. Magn. Reson.* **139**, 67 (1999).

12 Seymour, J. D., Codd, S. L., Gjersing, E. L. & Stewart, P. S. Magnetic resonance microscopy of biofilm structure and impact on transport in a capillary bioreactor. *J. Magn. Reson.* **167**, 322 (2004).

13 Herrling, M. P. *et al.* NMR Investigation of Water Diffusion in different Biofilm Structures. *Biotechnol. Bioeng.* (2017).

14 Ranzinger, F. *et al.* Direct surface visualization of biofilms with high spin coordination clusters using Magnetic Resonance Imaging. *Acta Biomater.* **31**, 167 (2016).

15 Nott, K. P., Paterson-Beedle, M., Macaskie, L. E. & Hall, L. D. Visualisation of metal deposition in biofilm reactors by three-dimensional magnetic resonance imaging (MRI). *Biotechnol. Lett.* **23**, 1749 (2001).

16 Baker, J. *et al.* Copper stress induces a global stress response in Staphylococcus aureus and represses sae and agr expression and biofilm formation. *Appl. Environ. Microbiol.* **76**, 150 (2010).

17 Kogan, F., Hariharan, H. & Reddy, R. Chemical exchange saturation transfer (CEST) imaging: description of technique and potential clinical applications. *Curr. Radiol. Rep.* **1**, 102 (2013).

18 McMahon, M. T., Gilad, A. A., Bulte, J. W. & Van Zijl, P. C. *Chemical Exchange Saturation Transfer Imaging: Advances and Applications*. Vol. 1 (CRC Press, 2017).
19 Mann, E. E. & Wozniak, D. J. Pseudomonas biofilm matrix composition and niche biology. *FEMS Microbiol Rev* **36**, 893 (2012).
20 Davis, J. & McLister, A. Passive and Interactive Dressing Materials. *Smart Bandage Technologies: Design and Application*, 93 (2016).
21 Ramdhan, T., Ching, S. H., Prakash, S. & Bhandari, B. Time dependent gelling properties of cuboid alginate gels made by external gelation method: Effects of alginate-CaCl2 solution ratios and pH. *Food Hydrocolloids* **90**, 232 (2019).

6 CONCLUSION AND FUTURE WORK

The scope of this project was to investigate and develop new non-invasive methodologies to study and characterize porous media and biofilms, using magnetic resonance imaging. in combination with other techniques. To achieve this, within this project we focused on three main objectives: characterize polymeric open-cell porous media parameters, when porous media are saturated with liquids; establish new non-invasive ways to image food, and biofilms' growth in porous media, which could enable to monitoring biofilm development in-situ and in real-time; correlate how biofilms' development can be affected by foam characteristics and food viability within it. The study of biofilm growth in sponges in relation with sponge properties and food viability is of particular interest for the fast-good moving consumer goods industry, where this better understanding is fundamental to produce cleaning products that can eliminate bacteria and biofilm more efficiently. Results from this study can also interest various other industrial sectors where biofilm and porous media are used in conjunction, such filtration or wastewater biodegradation, or sector where biofilms can pose serious risks, such as human health and wound treatment. Previous studies have been performed on biofilms in sponges, and their relationship with food residues within sponges. However, the need to pre-treat samples,[1,2] or use contrast agents, to distinguish biofilms from the sponge or food residues,[3] have limited the ability to study this relationship in-situ and in a non-invasive way. In this study, MRI has been investigated as a method to non-invasively characterize polyurethane foams, visualize food deposits inside foams and observe the growth of biofilms, without the need of additional contrast agents.

In chapter 3, polyurethane open-cell foam characterization has been reported on compressed and uncompressed foam, to study the behaviour and structural changes of the foam when compressed. Comparisons between T_2 NMR relaxation times of water within compressed and uncompressed sponge plugs with the maximum opening, evaluated with μCT for the same samples, has highlighted the dependence of T_2 on the pore dimension of the sponge. While the dependence of T_2 on pore dimension has already been investigated for rocks and has been used for evaluating rocks pore size and porosity,[4-6] no studies have been conducted on polymeric open-cell foams. In polymeric porous systems there is a low difference in magnetic susceptibility between the porous matrix and the fluid (usually water) within it. This small difference in susceptibility it has been expected to be too low a difference to see a variation in T_2 NMR relaxation time within porous media. However, our results have determined a relationship between T_2 relaxation time and maximum opening within a polyurethane open-cell foam, which enables the characterization of the porous media via MRI. Such application will be important for studying the behaviour and performances of polyurethane open-cell foams in applications where there is a link between pore size distribution and performance of the sponge or products within the sponge. These results are of particular interest for FMCG companies producing cleaning detergents. Indeed, the performances of cleaning detergents, and their capability to avoid biofilm formation in foams, are strongly correlated to the detergent penetration in sponges, which depends on the properties of the latter. If combined with MRI flow or diffusion imaging of the detergent within sponges, the direct characterization of sponge pore size via MRI offers a new way to understand how pore size and its variation upon

compression are affecting the detergent penetration and behaviour, in situ, on the same sample, with no needs of pre-treatments. Results from this chapter have been published on *Materials* on the 24th of April 2021.[7]

Sponge characterization is not only important to understand how detergents penetrate and perform within foams, but also to understand how sponge characteristic can affect food residues to be trapped within them. Food residues that are necessary for bacteria and biofilms, as they are used as energy sources. The direct visualization of food residues within sponges can help to better understand the relationship between food viability and biofilm growth, and to understand if a better removal of the former, can prevent the formation of the latter. Moreover, it can also improve the understanding on where and how food residues distribute with the media, how this is affected by the pore properties, and how, eventual use of detergents, change this distribution. In chapter 4, MRI has been showed to be successful in directly visualise food sources for bacteria within polymeric open-cell foams, in situ, without the need of adding contrast agents. For this purpose, MR chemical shift selective imaging (CHESS) methods have been tested on sponges filled with water and oil. The results have confirmed that with CHESS, oil and water within sponges can be selectively visualized. Thus, it has been proven that MR CHESS is able to separate different chemicals within sponges without using contrast agents. However, it is important to highlight that this selective separation is possible only for chemicals that possess NMR active species, with different chemical shifts compared to other chemicals within the sample. If direct food residues visualization in sponge is combined with an MRI investigation of biofilm growth within the same sponge, MRI could be used to directly visualize how food residues within

sponges affect biofilm formation. Apart from food visualization, the possibility to use CHESS to visualize various chemical substances in polymeric foams, can be interesting for a series of other applications, such as spoiled oil separation.[8] Indeed, being able to visualize in-situ, with no pre-treatment, what happens when a sponge is used in oil/water separation, can improve the understanding of the adsorption and separation processes.

To fully understand how pore structure and food viability affect biofilm growth, you need to have the opportunity to visualise biofilm growth within the same environment, at the same time. While biofilm observation in sponges can be performed with different techniques, such as such as scanning electron microscopy, or X-ray micro-computer tomography, the need for these techniques of pre – treatments does not allow the study of biofilm growth in real time. Moreover, in chapter 4, we have demonstrated the difficulty to visualize biofilms in polyurethane porous media when contrast agents are present. In chapter 5, the use of MR chemical exchange saturation transfer (CEST) method to visualize biofilms within sponges without using contrast agents, and the need of pre-treat the sample, has been tested. CEST has been tested on a biofilm mimic material (alginate). MRI CEST results on sodium alginate, alginate gel beads, and alginate gel, have all shown the presence of a CEST peak related to proton exchange between alginate and water, which confirms that CEST can generate a contrast between these substances and the surroundings, without the need of contrast agents. The ability of CEST to generate contrast between alginate gel and the surrounding solution has been proven for alginate beads. This was possible even if alginate residues were present in the solution surrounding the beads, which also gave

rise to a CEST effect. Unfortunately, this was not the case for alginate in a sponge. Indeed, for alginate gel in sponge, the MTR_{asym} value of the gel was almost equal to the MTR_{asym} value of CEST effect caused by alginate residues within the $CaCl_2$ saturating the sponge. Because of these close values, it was not possible to achieve the desired contrast between alginate gel and the surrounding solution within a sponge. However, it was believed that this small difference in CEST effect was a result of how the sample had been prepared. To overcome this problem, MRI CEST experiments of alginate in sponge need to be performed after at least 48h gel maturation, to ensure a full hydrogel formation. The CEST results on biofilm mimic materials confirms, for the first time, the ability of using CEST MRI to image biofilms. The major advantage of CEST, compared to other MRI techniques for visualizing biofilms, as relaxation time measurements, is the ability of CEST contrast to be turned on and off at will. This gives the possibility to image porous media and food residues, with and without the interference of biofilms, and thus have a better idea of the whole system.

This thesis highlighted that MRI can be used to characterize polymeric porous media, to visualize food residues within them without the need of contrast agents, and to image biofilm in-situ and in a non-invasive way. Combined, all these results offer the opportunity for a real-time visualization of biofilm growth in relation to sponge characteristics and food viability. Moreover, real-time measurements on cleaning methods and products can be performed on the same sample. The ability to perform all these measurements on the same sample, gives the opportunity to observe a more direct cause and effect. This gives MRI a huge advantage compared to other

techniques, where measurements need to be performed multiple time on different samples, and information are extracted through long winded statistics. However, it is important to highlight that, while MRI have many advantaged as explained, it has a lower resolution compared to other techniques, such as μCt and TEM. Thus, with MRI it will be hardly possible to characterize biofilm morphologies within porous media.

The results showed on this thesis demonstrate the potential of using MRI for these systems. However, to fully validate the possibility of using CEST on real biofilms, further studies need to be performed. CEST has to be tested on real biofilm within PU foams, to confirm the possibility to visualise biofilm using CEST imaging. Combined CHESS and CEST studies, on the same sample, have to be performed to directly study the impact of food residues within sponges on biofilm growth. Moreover, cleaning agents can be added to the same sample to monitor in real-time its diffusion within the foam (through diffusion and flow MRI[9]), and how food and biofilms are affected by them. In this way, a better understanding on how cleaning agents work in removing food, and disabling biofilm growth, can be developed.

Methodologies developed on this thesis work are can potentially be applied to a whole range of different applications, where polymeric porous media are used, and where the relationship between pore size and fluids are extremely important. Examples of this applications can be filtration process, or wound dressing, where the diffusion of drugs through the porous structure is fundamental for the success of wound recovery. Indeed, the possibility to obtain information on pore size, fluid dynamic, and differentiate chemicals without using contrast agents, live and with one single technique, can bring a massive improvement on the understating of such processes.

For this, a whole range of experiments need to be programmed and performed. Moreover, this work further opens to in-situ studies on 3D porous media systems and provide a valid tool to validate results on porous media obtained using simulation tools. This potential has been proved by Markale *et al* study.,[10] where MRI has been successfully used to obtain, for the first time, 3D images of mixing interfaces between two reacting fluids, and to understand how this interface is affected by pores sizes and phase saturation. This study has also allowed, for the first time, to confirm simulation results on these systems, obtained using continuum scale models.

6.1 References

1 Vafai, K. *Porous media: applications in biological systems and biotechnology*. (CRC Press, 2010).

2 Fassel, T. A. & Edmiston Jr, C. E. in *Methods Enzymol.* Vol. 310 194 (Elsevier, 1999).

3 Shastry, A. *et al.* In-Situ High Resolution Dynamic X-ray Microtomographic Imaging of Olive Oil Removal in Kitchen Sponges by Squeezing and Rinsing. *Materials* **11**, 1482 (2018).

4 Wang, R. *et al.* Xenon NMR measurements of permeability and tortuosity in reservoir rocks. *Magn. Reson. Imaging* **23**, 329 (2005).

5 Schoenfelder, W., Gläser, H.-R., Mitreiter, I. & Stallmach, F. Two-dimensional NMR relaxometry study of pore space characteristics of carbonate rocks from a Permian aquifer. *J. Appl. Geophys.* **65**, 21 (2008).

6 Washburn, K. E. & Madelin, G. Imaging of multiphase fluid saturation within a porous material via sodium NMR. *J Magn. Reson.* **202**, 122 (2010).

7 Cimmarusti, G. M. *et al.* Characterization of open-cell sponges via magnetic resonance and X-ray tomography. *Materials* **14**, 2187 (2021).

8 Peng, L., Yuan, S., Yan, G., Yu, P. & Luo, Y. Hydrophobic sponge for spilled oil absorption. *J. Appl. Polym. Sci.* **131** (2014).

9 Britton, M. M. Porous Media Studied by MRI. *eMagRes*, doi:10.1002/9780470034590.emrstm1263 (2011).

10 Markale, I., Cimmarusti, G. M., Britton, M. M. & Jiménez-Martínez, J. Phase saturation control on mixing-driven reactions in 3D porous media. *Environ. Sci. Technol.* **55**, 8742 (2021).

APPENDICES

Appendix 1: MATLAB code for MR CEST data analysis

```
%% section
N=41; %number of CEST images acquired
m = nan(64,64, N);
for i  = 1:N
   indices=(1:64)+64*(i-1)
   m(:,:,i) = a(indices,:);
end

%%  create a mask
mslice=m(:,:,1);
mask=mslice<5000;
for i=1:N
   m1=m(:,:,i);
   m1(mask)=nan;
   m(:,:,i)=m1;
end

%% create NxN 1-dimensional slices along the third dimension
for i = 1:64
   for j = 1:64 %the normal one is 64
      eval(sprintf('v%d_%d=m(%d,%d,:);',i,j,i,j));
      eval(sprintf('v%d_%d=v%d_%d(:);',i,j,i,j));
   end
end

%% cubic-spline interpolation and minimum detection
x =1800:-15:1200; % insert range of frequencies used for CEST experiment
xx =1800:-1:1200;
figure;
M=nan(64,64);
N=nan(64,64);
for i =1:64
   for j = 1:64
      tmp = eval(sprintf('v%d_%d',i,j));
      if ~isnan (tmp(1));
         yy=spline(x,tmp,xx);
         subplot(1,2,1);
         plot(x, tmp);
         hold on;
         subplot(1,2,2);
         plot(xx,yy);
         hold on
         [a,b]=min(yy(xx>1200));
         xxx=xx(xx>1200);
         if a>0
         M(i,j)=xx(b);
         N(i,j)=a;
         else disp([i,j]);
         end
```

```
        end
    end
end
ylim([0,3.5e5]);
xlim([-200,200]);
hold off

%% to shift the interpolated data to x=0HZ
x =1800:-15:1200;
xx= 1800:-1:1200;
figure;
S=nan(64,64,length(xx));
minM=min(M(:),[],'omitnan');
minN=min(N(:),[],'omitnan');
for i = 1:64
    for j = 1:64
        tmp = eval(sprintf('v%d_%d',i,j));
        if ~isnan (tmp(1))
            delta = M(i,j)-minM;
             if ~isnan(delta)
             YY = spline(x-delta,tmp,xx)
             XX=xx-minM
             plot(XX,YY)
             S(i,j,:)=YY;
             hold on;
             end
        end
    end
end
ylim([0,3.5e4]);
xlim([-200,200]);
hold off


%% create averaged z-spectrum and MTRasym
S1=reshape(S,4096,length(XX));
T=mean(S1,1,'omitnan');
tmax=max(T);
T=T/tmax;
minT=min(T); %find the min value of T
ind=find(minT==T); % find the location of minT
ind1=(ind)- 100;
ind2= (ind)+ 100;
h=plot(XX,T);
set(h,'Color', [0 0 1],'LineWidth',2);
xlabel('Frequency offsetb/Hz','FontSize',16);
yyaxis left
ylabel('z-spectrum', 'FonztSize',16, 'Color',[0 0 1]);
set(gca,'FontSize',16);
set(gca,'yColor',[ 0 0 1]);
ylim([0,1]);
xlim([-200,200]);
hold on
yyaxis right;
ylabel('MTRasym','Fontsize',16);
ylim([0,1]);
s1=T(:,ind1:ind);
```

```
s=T(:,ind:ind2);
s=flip(s);
mt=s1-s;
x1=-100:1:0;
h1=plot(x1,mt);
set(h1,'Color','r','LineWidth',2);
set(gca,'yColor','r');
hold off

%% creat image at wanted frequency
xpos = 150; %inserted wanted frequency
ind=find(XX==xpos);
tmp=S(:,:,ind);
imagesc(tmp);
colorbar;
%set(gca,'CLim',[0,3e4]);

%% create CEST map
p=(tmp-tmp2);
p1=p./tmp3
figure
%imagesc(xpos1);
imagesc(p1);
colorbar;
set(gca,'CLim',[0, 0.4]);
```

Appendix 2: “Characterization of open-cell sponges via magnetic resonance and X-ray tomography”.

Gabriele M. Cimmarusti Abhishek Shastry, Matthieu N. Boone, Veerle Cnudde, Karl. Braeckman, Anju D. M. Brooker, Eric S.J. Robles, Melanie M. Britton.

Citation:

Materials 2021, 14(9), 2187; https://doi.org/10.3390/ma14092187

View Online:

https://www.mdpi.com/1996-1944/14/9/2187